Universität Bremen

THOMAS HOLLANDS

MOTION TRACKING OF SEA ICE WITH SAR SATELLITE DATA

Dissertation

zur Erlangung des Grades Dr. rer. nat
vorgelegt dem Fachbereich Geowissenschaften
der Universität Bremen

EINGEREICHT:
am 27. September 2012

PROMOTIONSKOLLOQUIUM:
am 19. Dezember 2012

GUTACHTER:
Prof. Dr. Heinrich Miller
Dr. Georg Heygster

PRÜFER:
Prof. Dr. Peter Lemke
Prof. Dr. Cornelia Spiegel

Thomas Hollands: *Motion tracking of sea ice with SAR satellite data.*

WEBSITE:
http://www.awi.de/

E-MAIL:
thomas.hollands@awi.de

The author conducted the research for this dissertation in the working group "Earth Observing Systems" at the Alfred Wegener Institute for Polar and Marine Research, Bremerhaven. The work was funded by the Alfred Wegener Institute in the framework of the German Earth Observing Network (Network EOS).

ERKLÄRUNG

Hiermit versichere ich,

Thomas Hollands,
wohnhaft in der Max-Dietrich-Straße 28A, 27570 Bremerhaven,
dass ich

1. die Arbeit ohne unerlaubte fremde Hilfe angefertigt habe,
2. keine anderen als die von mir angegebenen Quellen und Hilfsmittel benutzt habe und
3. die den benutzten Werken wörtlich oder inhaltlich entnommenen Stellen als solche kenntlich gemacht habe.

Bremerhaven, den 27. September 2012

Thomas Hollands

ABSTRACT

Sea ice influences the life in the polar regions, but it also is an important factor in the climate system due to its interaction with atmosphere and ocean. Its motion has been systematically observed for about a century. For the last thirty years, sea ice kinematics have been studied continuously over large areas, also taking advantage of the increasing availability of satellite data. The intention of the majority of studies on sea ice motion is to observe drift patterns on scales of 25 km to 60 km, even though since about twenty years, synthetic aperture radar satellites allow the investigation of sea ice motion at scales of individual floes. Since the knowledge of small scale behaviour is important, e. g. for understanding deformation processes and for improving coupled sea-ice-ocean models, one part of this thesis is concerned with techniques for the observation of sea ice kinematics at a spatial resolution of 0.5 km to 5 km.

In the framework of this dissertation, the author implemented and modified an algorithm for the observation of high resolution sea ice motion, which was first described about four years ago. The algorithm employs a correlation based pattern matching to identify corresponding sea ice structures in a sequence of images. With the help of this tool, the author has observed sea ice motion in the Weddell Sea at high spatial resolutions of a few hundred metres up to a few kilometres. The author shows that sea ice can change its drift patterns completely within less than a day, if wind conditions are highly variable. Consequently, also a high temporal resolution of satellite images is required to accurately observe sea ice motion. Furthermore, the author compares ice drift simulated by a coupled sea-ice-ocean model with ice drift derived from satellite imagery. In this comparison, local processes of sea ice kinematics for the Ronne Polynia in the northwestern Weddell Sea are studied.

Since sea ice regions are often difficult to access, in-situ measurements to validate the calculated ice drift are sparse. The author estimates the accuracy of the retrieved drift fields by manually determining the sea ice displacements. He finds the error comparatively independent from the speed of the ice or resolution of the image data. It is merely dependent on the degree of distinctness and stability of the patterns in the images of sea ice. Manual drift measurements can be employed to validate an algorithm, but not as a regular tool to provide information on the reliability of automated drift calculations. Therefore, another part of this thesis focuses on the automated evaluation of the reliability of retrieved drift data. The author shows that the magnitude of the correlation coefficient of the pattern matching is not a sufficient criterion for the reliability of the derived motion field. Here, a new reliability estimate is introduced, combining the correlation coefficient, with measures of selected texture parameters and the results of a reversed drift calculation (called back-matching).

ZUSAMMENFASSUNG

Meereis beeinflusst nicht nur das tägliche Leben in den Polarregionen, sondern ist aufgrund seiner Wechselwirkung mit Ozean und Atmosphäre ein wichtiger Bestandteil des Klimasystems. Seine Bewegung wird seit etwa einem Jahrhundert systematisch untersucht. In den letzten dreißig Jahren wurde die Eisdrift zunehmend auch unter der Zuhilfenahme der wachsenden Anzahl von Satellitendaten beobachtet. Ein Großteil dieser Studien beschäftigt sich mit der Bewegung von Meereis auf Skalen von 25 km bis 60 km. Doch lässt die Auflösung der Radarsatelliten seit etwa zwanzig Jahren auch die Beobachtung individueller Schollenbewegungen zu. Da es wichtig ist diese kleinräumigen Bewegungsprozesse zu verstehen, um Deformationsvorgänge im Meereis zu beschreiben und Meereis-Ozean-Modelle zu verbessern, ist ein wesentlicher Aspekt dieser Arbeit die Beobachtung von Meereisdrift auf Skalen von 0.5 bis 5 km.

Im Rahmen dieser Dissertation implementierte und modifizierte der Autor eine Technik zur detaillierten Beobachtung von Meereisdrift, die 2008 zum ersten Mal beschrieben wurde. Der Algorithmus berechnet zu diesem Zweck die Verschiebung von Mustern im Meereis zwischen zwei aufeinanderfolgenden Bildern. Hierzu erkennt das Programm sich entsprechende Muster in beiden Bildern, indem es die Muster in beiden Bildern miteinander korreliert. Diese Methode ermöglicht es dem Autor Meereisbewegungen auf Skalen von wenigen Hundert Metern bis Kilometern zu beobachten. Die Ergebnisse zeigen unter anderem, dass sich die Meereisdrift innerhalb eines Tages vollständig verändern kann, wenn sie von sich stark ändernden Winden beeinflusst wird. Dies unterstreicht die Notwendigkeit regelmäßiger Satellitenbeobachtungen, um die Bewegung des Meereises zu studieren. Ein weiterer Gesichtspunkt dieser Arbeit ist der Vergleich der Beobachtungen mit Ergebnissen eines gekoppelten Meereis-Ozean-Modells. Im Rahmen dieses Vergleiches wurde die Eisdrift innerhalb der Ronne-Polynja im antarktischen Weddell-Meer untersucht.

Da Meereis meist schwer zugänglich ist, stehen in situ Daten, die notwendig wären, um die berechneten Verschiebungen zu validieren, nur selten zur Verfügung. Deshalb schätzt der Autor die Genauigkeit der Driftvektoren mit Hilfe manuell bestimmter Verschiebungsinformationen. Dabei ist die Genauigkeit der berechneten Bewegung relativ unabhängig von der Geschwindigkeit des sich bewegenden Meereises. Vielmehr hängt sie von der Eindeutigkeit und Beständigkeit der Muster innerhalb der Bildfolge ab. Zwar eignen sich manuell bestimmte Driftvektoren, um den Algorithmus zu validieren, jedoch nicht um die Zuverlässigkeit der Drift standardmäßig zu beurteilen. Der Autor zeigt, dass der Korrelationskoeffizient allein kein geeignetes Maß zur Beurteilung der Zuverlässigkeit eines berechneten Bewegungsfeldes ist. Um Abhilfe zu schaffen, stellt er ein neues Maß vor. Dieses Maß berücksichtigt neben dem Korrelationskoeffizienten der Mustererkennung auch verschiedene Kriterien zur Beschreibung der Eindeutigkeit eines zu vergleichenden Musters und stellt zusammen mit den Ergebnissen einer inversen Driftberechnung ein verlässliches Kriterium zur Bewertung der berechneten Drift dar.

DANKSAGUNG

Ich danke Herrn Prof. Dr. Heinrich Miller und Herrn Dr. Georg Heygster für die Bereitschaft meine Arbeit zu betreuen und zu begutachten sowie Prof. Dr. Rüdiger Gerdes für seine Mitwirkung in meinem Doktorandenkomitee. Ein besonderer Dank gebührt Herrn Dr. Wolfgang Dierking, der mich bei dieser Arbeit über die letzten drei Jahre mit Rat und Tat begleitet hat. Des Weiteren möchte ich meinen Kolleginnen Stefanie Linow und Corinna Ziemer und vielen anderen für ihre vielfältige Unterstützung und Zeit danken.

TABLE OF CONTENTS

1 INTRODUCTION

When sea water freezes, it becomes sea ice which forms a connected or broken layer covering the liquid water underneath. It is put into motion mainly by atmospheric forces and underlying ocean currents. Sea ice affects life, industry and nature in the polar regions (e. g. as base for human activities like hunting, as limitation for ship traffic and offshore industry or as an ecological habitat). Information on sea ice conditions is important for shipping routes (e. g. the Northwest Passage) and for offshore constructions like oil platforms or lighthouses.

The history of systematic sea ice motion observations started more than a century ago, when Fridtjof Nansen moored his ship Fram to the ice and drifted with it across the Eurasian Arctic Ocean between 1893 and 1898. He observed that the velocity of wind-driven sea ice motion was on average 2 % of the wind speed and that its direction deviated 30° to the right from the wind direction [Nansen, 1902]. For the following seventy years, the research on sea ice kinematics was continued with buoys, drift stations and ship observations. The results were sea ice drift data, which were spatially sparse but had a high temporal resolution, allowing only limited assumptions on the Arctic-wide motion of sea ice and its deformation. This changed in the late nineteen-seventies, when the first satellite data became available. By means of a sequence of satellite images, it was possible to track the motion of sea ice at much higher spatial resolutions than thitherto possible.

1.1 IMPORTANCE OF SEA ICE IN THE CLIMATE SYSTEM

The sea ice cover is an important factor in the climate system. It insulates the ocean from the cold atmosphere and increases the albedo of the ocean surface. Hence, it causes a reduction of the solar radiation absorbed by the ocean surface. Extent, thickness and concentration of sea ice have a direct influence on the heat exchange between atmosphere and ocean. During the formation of sea ice latent heat is released to the ocean. Since the salt contained in the water does not fit into the crystal lattice of the growing sea ice, it is released to the underlying ocean surface layer as a high concentration salt solution, the so called *brine*. The salinity of new ice is about 50 % of the salinity of the underlying seawater. For multi-year ice, the typical salinity reduces to about 1 %. The release of brine to the ocean surface layer during ice growth destabilises the stratification of the water column below. In contrast, the surface layer becomes fresher and more stable, when the ice melts.

The drift of ice is the result of the interaction between the ice, the atmospheric boundary layer, and the ocean surface layer. For the understanding of the atmosphere-ocean interface, it is therefore of crucial importance to

study the ice drift and deformation patterns. The different forces which act on the sea ice are described in Section 3.1. By drift, sea ice is redistributed from regions of ice growth to regions of ice disintegration. Ice drift leads to the formation of leads (divergent motion) and deformation zones such as ridges and rubble fields (convergent motion). In coastal areas, zones of open water are generated by winds blowing seawards. These areas are called *polynia*. Polynias are important elements in the ocean-atmosphere exchange in the presence of sea ice. As gaps in the insulating sea ice cover, they allow a strong heat exchange between ocean and atmosphere which leads to an increased heat loss of the ocean and a warming of the air column above [Lüpkes *et al.*, 2008].

Due to the release of brine and latent heat during the formation of the sea ice, the drift of sea ice corresponds to a negative transport of latent heat and fresh water. Where sea ice is formed, fresh water is removed from and latent heat is added to the ocean. When sea ice is melting at a different place due to the drift, the water is cooled and gets fresher. Resulting spatial gradients in salinity and temperature can trigger the formation of currents. However, the melting of sea ice can as well strengthen the stratification and slow down the polar deep convection [Leppäranta, 2011].

One example for large amounts of drift ice is the export of sea ice from the Arctic through the Fram Strait into the Greenland sea. The Fram Strait is the main route for drift ice leaving the central Arctic ocean. Its outflow is about the same volume as the river run-off from the surrounding landmasses into the Arctic ocean. The ice export through the Fram strait integrates to about 3×10^3 km^3 per year and influences the circulation of the Atlantic ocean and especially the gulf stream [Hader, 1996; Leppäranta, 2011].

1.2 MODELLING AND OBSERVING SEA ICE MOTION

Drift buoys or drift stations can provide information on sea ice motion with high temporal resolution. However, they provide only data of single tracks. If the kinematics of sea ice for a whole region or basin have to be known on a fixed grid, i. e. several locations, problems arise when matching buoy or station data to the grid. Therefore, it is necessary to find supplementary ways to study sea ice motion. Spatial ice drift vector fields can be simulated by sea ice ocean models, or they can be retrieved from remote sensing data, as discussed in the further course of this thesis. The modelling of sea ice motion is based on assumptions on the ice motion in dependence on factors like wind, currents and ice floe interaction. Remote sensing provides snapshots of the sea ice on the ocean. The average ice motion is estimated by comparing the position of sea ice patterns in two subsequent snapshots. Satellite observations and model simulations are more similar to each other than to buoy observations. While buoys record the position of a floe over time (Lagrangian reference system), models and satellites calculate the motion of the sea ice at a fixed geographical position (Eulerian reference system).

It was shown by Kwok *et al.* [1990] that both remote sensing observations and model simulations can complement one another. The author employed a simple linear drift model to identify image pairs, in which the number of well corresponding sea ice patterns is maximum. The model predicts the ice drift for the time between the acquisition of both images, which then helps the algorithm to find the area to which the ice has approximately been shifted.

For the validation of the sea ice drift obtained from sea ice models, both in-situ instruments and remote sensing data are used. Ice drift derived from remote sensing imagery can be validated by comparing data with drift information from buoys and stations. Geiger *et al.* [1998] employed data from an ice drift station in the Weddell sea to compare model results with buoy observations. About four year later, also Timmermann *et al.* [2002] used buoys for model validation in the Weddell sea. McLaren *et al.* [2006] assessed the sea ice drift simulated in a coupled atmosphere-ocean climate model (HadGem1) based on the Pathfinder data by Fowler [2003] and the Atlas of Antarctic Sea Ice Drift by Schmitt *et al.* [2004]. The pathfinder data fuse observations from various satellite sensors as well as Arctic buoys and cover the entire Arctic and Antarctic sea ice regions while the Atlas focusses the Antarctic region. Stern and Moritz [2002] as well as Thomas *et al.* [2011] employed the track of the SHEBA ice drift station from October 1997 to October 1998 to validate motion vectors estimated from satellite images. Recently, Kwok [2011] analysed climate simulations (CMIP3) for the Arctic by comparing results on sea ice motion, concentration, thickness, and sea level pressure with satellite data.

1.3 MOTIVATION OF THIS STUDY

Depending on the scale of view, sea ice changes its characteristics of motion: At the large (basin) scale, sea ice is traditionally regarded as a non-rigid continuum. On the spatial scale of individual floes or in the vicinity of cracks, leads and deformation zones within the sea ice cover, however, it shows a discontinuous behaviour. For the study of general drift trends over large regions there exist several sea ice drift products derived from satellite imagery (see also Section 3.3). They provide daily drift information, but their resolution is coarse, corresponding to the resolution of most sea ice motion models, i. e. tens of kilometres[1].

The observation of individual floes has been possible since twenty years, when new satellite sensors first provided images with high spatial resolution ($\approx 100\,\mathrm{m}$). However, only nearly ten years ago, attempts to retrieve discontinuous drift were presented by Thomas *et al.* [2004]. Since about the same time, the resolution of a number of sea ice models has been increased. Therefore, the parametrisation of certain interaction processes in the ice drift field needs to be changed. The increased resolution of both sea ice drift from satellite imagery and model simulations allow the study of local processes in the ice drift field. This provides a chance to improve the parametrisation of sea ice motion in global models.

The motivation of this study is to assess the potential of ice drift monitoring using high-resolution radar images for the validation of coupled sea-ice-ocean

1 The resolution of the Pathfinder data is e. g. $25\,\mathrm{km} \times 25\,\mathrm{km}$ [Fowler, 2003]

models. Ice drift fields retrieved from radar and from model simulations are presented at spatial resolutions of 2 km to 5 km. One study with in the frame of this thesis focusses specifically in the ice movement during the formation of a polynia. Another important objective is to provide intrinsic reliability measures to assess the quality of calculated drift fields. Reliability information of estimated sea ice motion is e. g. essential not only for the comparison of the sea ice motion vectors retrieved from satellite imagery with model simulations, but also for operational sea ice mapping and for the assimilation of sea ice data into numeric models.

In addition to methodological improvements of sea ice motion tracking, the effect of temporal coverage with satellite images on the retrieval of the actual motion needs to be considered. Corresponding examples are discussed.

1.4 STRUCTURE OF THE THESIS

The thesis is subdivided into seven chapters. In Chapter 2, the author describes the general principle of estimating the motion from sequences of images. Chapter 3 deals with the different mechanisms which put sea ice into motion. Different satellite data products used for the estimation of sea ice motion are presented and a brief historical overview of the estimation of sea ice motion from satellite imagery is given. In the subsequent Chapter 4, the implemented method for sea ice motion tracking from satellite imagery based on the general concepts of motion analysis introduced in Chapter 2 is discussed in depth. After this, the scope of the attached papers as well as the respective contributions of the author are described in Chapter 5. The work closes with a summary (Chapter 6) and an outlook on future research in this field (Chapter 7).

2 ESTIMATION OF MOTION FROM IMAGES

An image can be interpreted as a 2D-function $E(x, y)$, where the spatial distribution of an amplitude E is described depending on x and y. The amplitude can be interpreted as *intensity*, *brightness* or *grey-value*. The function $E(x, y)$ is influenced by two components: (1) the amount of illumination from a source incident on the scene being covered by the image (*illumination*) and (2) the amount of illumination reflected by the objects in the scene (*reflectivity*). The image function $E(x, y)$ is originally continuous with respect to x, y. When x, y and E are all finite and discrete quantities, the image is referred to as a digital[1] image. To gain discrete values, the image is sampled at discrete positions (x_i, y_i), while the amplitude E is quantised from the continuous function at each discrete position (x_i, y_i). From an abstract point of view, digital images are patterns of discrete brightness values or pixels, mirroring the continuous image function $E(x, y)$ on a regular grid with a defined pixel size [Gonzalez and Woods, 2008].

All measurements are erroneous. The error consists of a systematic component, which corresponds to the mean deviation of the measurement from the undisturbed "true" signal, and a random component, which is described by the standard deviation. The random error is also called *noise*. It disturbs the interpretation of information in the signal. Noise can e. g. be caused by the sensitivity of the sensor to *shot noise* or the used sensor technique. Shot noise is a type of electronic noise, that originates from the discrete nature of photons and is unavoidable for any photon detector. A special kind of noise occurs in the case of Synthetic Aperture Radar (SAR) images. They use coherent microwaves to illuminate the ground and measure the backscatter. The signal is backscattered randomly from a usually large number of scatterers, from each scatterer at the same frequency but with different phase and amplitude. The signals from the individual scatters interfere with each other. This results in a random amplitude variation. The resultant 2D amplitude function multiplies with the information contained in the measured signal and creates a specific kind of multiplicative noise. This special kind of noise is called *speckle*.

For the sake of consistency with other authors, the author will use a less strict definition of noise in the further course of this work. Noise is defined as any unwanted component in the analysed signal. This may be actual noise, but also includes any systematic distortions caused by different acquisition conditions or other effects that change the signal in an unwanted way. If one e. g. analyse hyper-spectral images, it depends on one's goals what is regarded as noise. For SAR images, for example, there exists an incidence angle dependence of the backscatter. Since it is not random, it is strictly spoken no noise but is included into the more broad definition of the term used in this thesis.

The estimation of motion and its average velocity from two subsequent images corresponds to the estimation of displacements, normalised to the

1 digital from lat. digitus: finger, counted with fingers

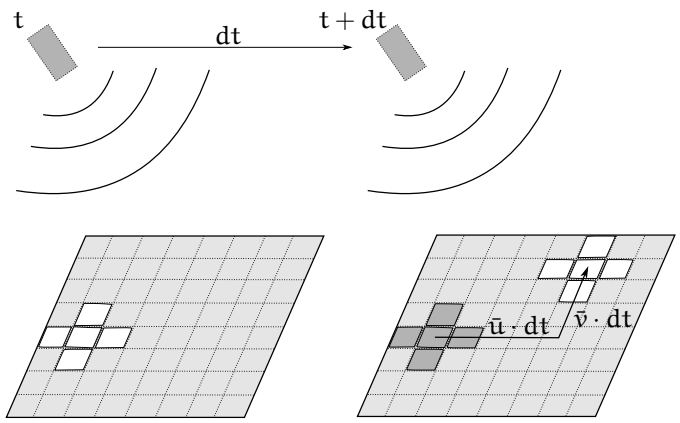

Figure 1: Estimation of motion from two subsequent images. The Figure shows the acquisition of a sequence of two satellite images at a point of time t and $t + dt$ and the observed displacement of a pattern. $\bar{u}$ and $\bar{v}$ are introduced in section 2.2.

time interval between the acquisition of the images. In this chapter, the derivation of displacement information from image sequences is discussed. The calculation of displacements between two images can in most cases be traced back to one of three central concepts. They are introduced in the subsequent sections:

- Optical flow / Gradient-based motion tracking (Section 2.1)
- Pattern matching (Section 2.2)
- Feature tracking (Section 2.3)

Additional concepts, e. g. based on wavelets, exceed the scope of this work and will not be presented here.

2.1 GRADIENT-BASED MOTION TRACKING

For gradient-based motion tracking, numerical differentiation is employed to spatially and temporally analyse brightness changes. The tracking is also referred to as calculation of the *optical flow*. With gradient-based motion tracking, a direction and a velocity are assigned to every pixel in an image sequence via the corresponding brightness gradient. Let us consider a single value of a brightness pattern (image) at position (x_i, y_i), which is displaced by a distance dx in x-direction and a distance dy in y-direction during the time interval $[t, t + dt]$. If we assume that the brightness of the pixel (x_i, y_i, t) in the first image and the brightness of the corresponding pixel $(x_i + dx, y_i + dy, t + dt)$ in the second image are identical (*brightness constraint*), we can state:

$$E(x, y, t) = E(x + dx, y + dy, t + dt). \tag{1}$$

By employing the Taylor series expansion we can show that in a first approximation for small dt it holds:

$$\nabla E \cdot \nabla_t(x, y, t) = \frac{\partial E}{\partial x}\frac{dx}{dt} + \frac{\partial E}{\partial y}\frac{dy}{dt} + \frac{\partial E}{\partial t} = 0. \tag{2}$$

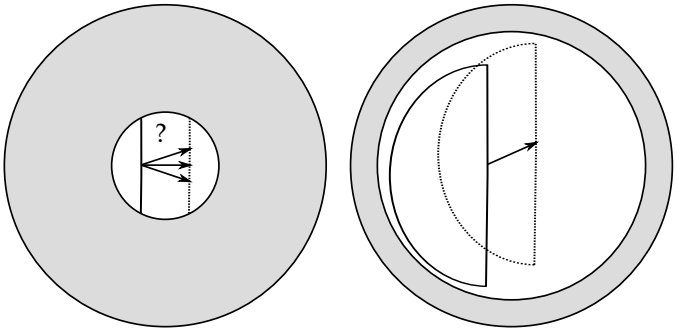

Figure 2: Aperture Problem. The left image shows a motion through a small aperture. It is only possible to identify the horizontal shift. The right image depicts the same motion trough a large aperture. Here both motion components can be identified.

This equation can be used to calculate the horizontal and vertical velocity components of the motion

$$u = \frac{dx}{dt} \quad \text{and} \quad v = \frac{dy}{dt},$$

of each pixel. Substituting the above equations into Equation (2), it becomes a single linear equation with two unknowns u and v:

$$\frac{\partial E}{\partial x}u + \frac{\partial E}{\partial y}v + \frac{\partial E}{\partial t} = 0. \tag{3}$$

This relation is sometimes referred to as *optical flow constraint*. It allows the calculation of the displacement in the direction of the brightness gradient ($\frac{\partial E}{\partial x}$, $\frac{\partial E}{\partial y}$). Since it is not possible to derive two unknowns from one linear Equation, it is necessary to define a second constraint to calculate the displacement perpendicular to the brightness gradient. This ambiguity is comparable with a look through a very small aperture which excludes the surrounding neighbourhood. Figure 2 illustrates the problem. On the left side we see two vertical lines, a dashed and solid one. The solid line represents the position of the line in an image while the dashed line represents its future position in the successive image. Based on the information gained from the small aperture it is not possible to derive the vertical component of the displacement obviously contained in the image when "opening the aperture" on the right side of the figure. For this reason, this ambiguity is called the *aperture problem*. It was first described by Wallach [1935]. Equally, in Equation (2) the surrounding neighbourhood is not taken into account for motion estimation.

Two commonly used constraints to solve this ambiguity are assumptions regarding the structure of the motion field. While Horn and Schunck [1981] assume that the motion field changes smoothly by minimising the square of the magnitude of the motion field gradient, Lucas and Kanade [1981] assume that motion is constant in the local neighbourhood of the patch under consideration, calculating an "optimised" motion for this neighbourhood using the least square criterion to minimise the sum of squares of the errors.

One problem of gradient-based motion tracking is, that the optical flow constraint is only valid for very small time steps because of the assumption of constant brightness. This limits the application of algorithms based on

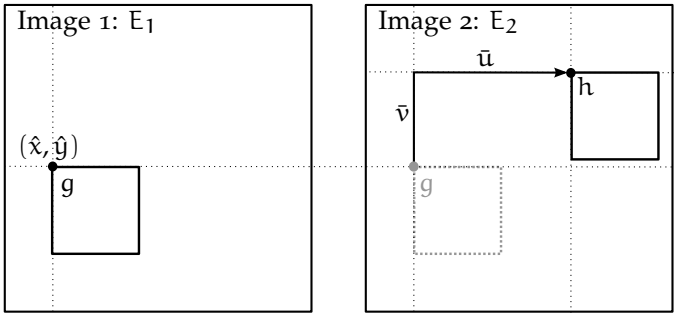

Figure 3: Template g running over a second image, while searching for the minimum distance between the second image and g

the optical flow constraint to image sequences with a high temporal resolution. In cases of low temporal resolution (only few frames: e. g. satellite images) or poor signal-to-noise ratio, numerical differentiation is impractical in most cases and matching algorithms are a better choice [Barron *et al.*, 1994; Beauchemin *et al.*, 1996].

2.2 PATTERN MATCHING

In most images, patterns formed by a number of pixels in a given *template* or *window* can be recognised. If an algorithm searches for these patterns in a subsequent image, it is called *pattern matching algorithm*.
If E_1 and E_2 describe the image intensity of two images acquired at times t and $t + dt$, respectively, corresponding patterns between both images are identified by the minimisation of a cost function. In image 1, a template g can be defined by its vertex $(\hat{x}, \hat{y})$ and its pixel size $(\Delta x, \Delta y)$. For the sake of simplicity we assume a quadratic template with a resolution $(N \times N)$:

$$g(x_k, y_j) = E_1(\hat{x} + k \cdot \Delta x, \hat{y} + j \cdot \Delta y) \quad \text{for } j, k = 0, \ldots, N. \tag{4}$$

In the following, g is shifted over the second image. Its respective position relative to the original position of its vertex is given by $(\bar{u}, \bar{v})dt$ under the condition that $\frac{\bar{u}\,dt}{\Delta x}$, $\frac{\bar{v}\,dt}{\Delta y}$ are integers. The area in the second image, covered by g, is given by:

$$h_{\bar{u},\bar{v}}(x_k, y_j) = E_2(\hat{x} + \bar{u}dt + k \cdot \Delta x, \hat{y} + \bar{v}dt + j \cdot \Delta y) \quad \text{for } j, k = 0, \ldots, N. \tag{5}$$

While g is shifted over E_2 via a variation of $(\bar{u}, \bar{v})$, the distance (i. e. the similarity) between g and $h_{\bar{u},\bar{v}}$ is calculated continuously. Figure 3 depicts this search. Where the chosen distance measure reaches its minimum, g and $h_{\bar{u},\bar{v}}$ are most similar and the most probable position of the vertex of g in E_2 is $(\hat{x}, \hat{y}) + (\bar{u}, \bar{v})_{min}dt$. The displacement of the pattern in the template g is described by its corresponding displacement vector $(\bar{u}, \bar{v})_{min}dt$. Since the cost function is minimised for various positions $(\hat{x}, \hat{y})$ of g, a collection of multiple displacement vectors is created which describes the displacements between both images. This collection of vectors is also called *vector field*, or in the case of floating sea ice, *drift field*. The resolution of such a vector field only depends on the number of positions $(\hat{x}, \hat{y})$ for g and the design of the algorithm, which shifts the template.

One of the simplest distance measures is the *sum of absolute distances* (SAD) between a group of brightness values (pixels) in the original template g and their corresponding brightness values in the search window $h_{\bar{u},\bar{v}}$. The $\mathrm{SAD}_{\hat{x},\hat{y}}(\bar{u},\bar{v})$ is given by:

$$\mathrm{SAD}_{\hat{x},\hat{y}}(\bar{u},\bar{v}) = \sum_{j,k=0}^{N} \left| h_{\bar{u},\bar{v}}(x_k, y_j) - g(x_k, y_j) \right| \tag{6}$$

A related measure is the *sum of squared differences* (SSD), also known as euclidean distance. Compared to the SAD, the squaring of the differences emphasises the influence of single larger differences on the measure.

$$\mathrm{SSD}_{\hat{x},\hat{y}}(\bar{u},\bar{v}) = \sum_{j,k=0}^{N} \left[h_{\bar{u},\bar{v}}(x_k, y_j) - g(x_k, y_j) \right]^2 \tag{7}$$

One of the most frequently used distance measures in the field of motion tracking is the cross-correlation between two patterns, i. e. the calculation of their covariance. Its calculation can be traced back to the calculation of the SSD. By the second binomial formula, we can expand Equation (7) to:

$$\mathrm{SSD}_{\hat{x},\hat{y}}(\bar{u},\bar{v}) = \sum_{j,k=0}^{N} h^2_{\bar{u},\bar{v}}(x_k, y_j) - 2 \cdot h_{\bar{u},\bar{v}}(x_k, y_j) \cdot g(x_k, y_j) + g^2(x_k, y_j) \tag{8}$$

Since $\sum_{j,k=0}^{N} g^2(x_k, y_j)$ is the squared sum of the original pattern, it is constant under variation of $(\bar{u},\bar{v})$. If we assume that the pixel values in the image are equally distributed, we can assume that $h_{\bar{u},\bar{v}}$ contains a combination of the same pixel values for all considered $(\bar{u},\bar{v})$, although possibly in differing order. In this case $\sum_{j,k=0}^{N} h^2_{\bar{u},\bar{v}}$ would be approximately constant as well. By neglecting both parts in Equation (8) and dividing the remaining term by (-2), the cross-correlation term following Lewis [1995], is given by:

$$c_{\hat{x},\hat{y}}(\bar{u},\bar{v}) = \sum_{j,k=0}^{N} h_{\bar{u},\bar{v}}(x_k, y_j) \cdot g(x_k, y_j) \tag{9}$$

This formulation of the cross-correlation corresponds to the *covariance* between two distributions of brightness values, described by $h_{\bar{u},\bar{v}}$ and g. Mathematically, the above product of the functions $h_{\bar{u},\bar{v}}$ and g is a convolution. Due to the division by (-2), corresponding patterns in two images are identified by maximising the correlation coefficient c. While the convolution of two discrete functions in the spatial domain causes a number of summations and multiplications, the result of the convolution can be estimated more efficiently within the Fourier domain where a convolution can be performed by the multiplication of the Fourier transforms of both functions.

When acquiring a digital image, it is is stored in the *spatial domain*. If one transforms these images into the *spectral domain* (i. e. *Fourier domain*), the discrete spatially distributed brightness values of the image are represented by frequencies, phase angles and amplitudes (described as complex numbers). The Fourier transformation specifies how to reconstruct the brightness pattern by the superposition of sine functions with different frequencies and phase angles. Sharp transitions in the brightness pattern are represented by high frequencies while soft transitions are represented by low frequencies. Equation (10) is the realisation of the cross-correlation in the Fourier domain.

Here $\mathcal{F}$ denotes the Fourier transform, $\mathcal{F}^*$ its complex conjugate and $\mathcal{F}^{-1}$ the back-transformation into the spatial domain.

$$c_{\hat{x},\hat{y}}(\bar{u},\bar{v}) = \mathcal{F}^{-1}(\mathcal{F}(h_{\bar{u},\bar{v}}) \cdot \mathcal{F}^*(g)) \tag{10}$$

Since the Fourier transformation represents the brightness pattern by periodical sine functions, they introduce an error by assuming their periodical continuation. Therefore it only measures *cyclic shifts*. However, one would not expect a pattern leaving an image at one side to enter it instantaneously at the other side again. Observed displacements in images are seldom cyclic. For this reason one will not obtain a function which shows a smooth surface with an single extreme value (impulse) but a degenerated impulse appearing as a peak with relatively steep slopes [Berg *et al.*, 2011]. This effect can be reduced when framing the input pattern by introducing an artificial border into the spectral representation of the brightness pattern. This method is called *zero-padding*. By zero-padding the input signals (template g and brightness pattern in the search window $h_{\bar{u},\bar{v}}$ of the second image), the spectral cross-correlation is equivalent to the one in the spatial domain [Eckstein and Vlachos, 2009].

The pattern matching based on the maximisation of the cross-correlation term following Equation (9), has three disadvantages. (1) Since it assumes an equal distribution of brightness values over the image, the calculated correlation values are only comparable if the distribution of brightness values within the scene is approximately constant. Matching can fail if it varies. This can e. g. be the case, when the correlation between a pattern and a corresponding pattern is smaller than the correlation of the same pattern with a pattern containing a bright spot. (2) It cannot take into account changing illumination over the image sequence. (3) Additionally, the correlation coefficient depends on the size of the template. Therefore the correlation coefficient for different template sizes is not comparable.

One way to overcome these problems is to subtract the mean brightness value of the pattern from all pixel values in the template and divide the cross-correlation (9) by the standard deviation of these differences, leading to the following equation:

$$\mathrm{NCC}_{\hat{x},\hat{y}}(\bar{u},\bar{v}) = \frac{\sum_{j,k=0}^{N} \left[h_{\bar{u},\bar{v}}(x_k,y_j) - \bar{h}_{\bar{u},\bar{v}}\right] \cdot \left[g(x_k,y_j) - \bar{g}\right]}{\sqrt{\sum_{j,k=0}^{N} \left[h_{\bar{u},\bar{v}}(x_k,y_j) - \bar{h}_{\bar{u},\bar{v}}\right]^2 \cdot \sum_{j,k=0}^{N} \left[g(x_k,y_j) - \bar{g}\right]^2}} \tag{11}$$

where $\bar{g}$ is the mean of the template g taken from the first image and $\bar{h}_{\bar{u},\bar{v}}$ is the mean of $h_{\bar{u},\bar{v}}$ in the region of the consecutive image covered under the shifted template. Equation (11) corresponds to the normalisation of the covariance between two functions with the product of their individual standard deviations and is often referred to as normalised cross-correlation (NCC). The NCC is one of the most commonly used distance measures for pattern matching. Even if it is not invariant to rotation, it provides a good performance in the presence of noise in the image. [Burt and Adelson, 1983; Lewis, 1995]. The NCC is the 2D realisation of the Pearson product-momentum-correlation-coefficient [Rodgers and Nicewander, 1988].

Since the NCC contains non-linear terms introduced by the normalisation employing the standard deviation (division and squares), it cannot be formulated as a convolution [Gonzalez and Woods, 2008] and thus it cannot be transferred to the Fourier domain. To transfer the advantages of the NCC from the spatial to the spectral domain, the influence of effects like local variation of brightness values or change of its global brightness on the cross-correlation (10) have to be reduced. The most common approach is known as *phase correlation* (PC) and described in Equation (12). This approach is described by e. g. Canty [2007] or Eckstein and Vlachos [2009] and uses a phase transformation filter (PHAT-filter). Herewith a so called normalised cross-power spectrum is calculated by normalising the cross-correlation in the Fourier domain to unit magnitude of amplitude. The cross-power spectrum is transformed back to the spatial domain and forms the phase correlation surface which contains a sharp correlation peak indicating the displacement of the pattern. Since the phase difference of every frequency contributes equally (due to the eliminated influence of the amplitude), the location of the peak on the phase correlation surface will not change if there is noise which is limited to a small range of frequencies [Brown, 1992]. This property makes the peak location of the PC notably insensitive to those types of noise, which are correlated to the image function, like uniform variations of illumination or offsets in average intensity [Foroosh *et al.*, 2002].

$$\mathrm{PC}_{\hat{x},\hat{y}}(\bar{u},\bar{v}) = \mathcal{F}^{-1}\left[\frac{\mathcal{F}(h_{\bar{u},\bar{v}})\cdot\mathcal{F}^{*}(g)}{|\mathcal{F}(h_{\bar{u},\bar{v}})\cdot\mathcal{F}^{*}(g)|}\right] \tag{12}$$

Even if this approach has been shown to be successful [Burt and Adelson, 1983; Lewis, 1995], the peak of the phase correlation surface is sensitive to additive high frequency noise [Eckstein and Vlachos, 2009; Manduchi and Mian, 1993]. There are various approaches discussed by e. g. Eckstein and Vlachos [2009], suggesting other filters than the PHAT-filter to meet this drawback.

In contrast to the NCC, the PC is invariant to rotation of the sought-after pattern in the image [Gonzalez and Woods, 2008; Lucchese *et al.*, 2002; Thomas *et al.*, 2008a]. Since most search strategies for pattern matching focus on translational motion, this advantage is of theoretical nature only.

2.3 FEATURE TRACKING

Feature tracking algorithms do not match brightness patterns in two images, but employ a pre-posed recognition step during which features with distinct shapes are identified in both images. In the following, the algorithm evaluates the similarity of the feature found in both images with some kind of distance measure. To do so, it is necessary to analyse the texture before the tracking to identify existing semantics. This can be done by segmentation, classification or edge detection. To trace a feature, it must be described in both images. The chosen descriptor of the feature should not change (e. g. when describing an ice floe by its shape, the floe should neither partly melt nor break). Since feature tracking only takes into account the features identified and described during the recognition phase, the resulting displacement information has a lower resolution than that gained by pattern matching and is only available for identified features. The recognition step however reduces the number

of necessary matching operations (distance calculations or correlations) and leads to a reduced computation load for the matching itself.

The main advantage of feature-based algorithms is their high reliability of matched features (like e. g. shape). Feature tracking algorithms are invariant to rotation and illumination. Therefore they can be extremely useful to handle the influence of changing light conditions as well as rotational motion that often occurs at the marginal ice zone.

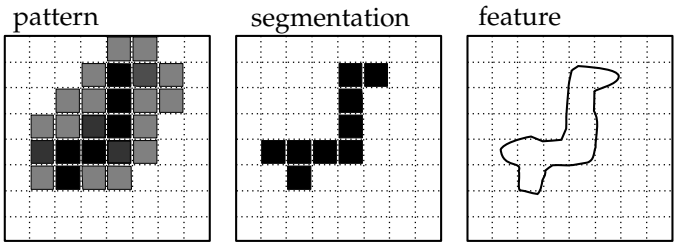

Figure 4: Feature tracking. The left part shows the pattern of the original image, the central part the segmented version of the pattern and the right part the description of the found object by its smoothed shape.

3 SEA ICE IN MOTION

Sea ice plays an important role in many processes of the climate system. For example, it has a strong influence on the absorption and emission of radiant energy in the polar regions and also on the poleward heat-flux. Carsey *et al.* [1992] present a number of main quantities of interest to both the operational and scientific data user. These are ice extent and thickness, snow depth and snow wetness, duration of summer melt period and melt-pond coverage, ice motion and deformation as well as wind and ocean currents pushing the ice, cloud cover, and air and ocean temperatures controlling growth and melt of the ice. Most of these parameters can be derived from satellite data. This work will be confined to the observation of sea ice motion.

3.1 DRIFT ICE

Sea ice is drifting, because it is accelerated by forces acting on it. These forces have three basic origins: wind, ocean currents and internal ice stresses.

On short time-scales of days and weeks, the strongest influence on the drift of sea ice is exerted by the wind. It introduces a drag which depends on the wind speed and on the surface characteristics of the sea ice. A rough sea ice surface provides a larger sail area than a smooth surface and reacts more sensitive to the wind. In the Arctic, an individual ice floe with an average surface roughness, which is free of any interaction with other ice floes or borders like coast lines, has a velocity of about 2 % of the wind speed [Nansen, 1902; Thorndike and Colony, 1982]. For Antarctica, larger velocity ratios have been observed. Brennecke [1921] found a velocity of about 2.8 % of the wind speed while Martinson and Wamser [1990] obtained a ratio between the velocity of the sea ice motion and the wind speed of about 3 % for the Weddell Sea. In the second paper of this work, the author analysed, among other things, the wind ratios of observed and modelled sea ice velocities for the Ronne Polynia [Hollands *et al.*, 2012b] [1].

The drift direction of ice floes is at a range of about 20° to 40° to the right (Northern Hemisphere) or left (Southern Hemisphere) of the wind direction. This was first described by Nansen [1902] and explained by Ekman [1902]. In the meantime, these observation have also been confirmed by experiments e. g. undertaken by Thorndike and Colony [1982]. The turning angle of the drift direction of the moving sea ice compared to the wind direction cannot be explained with the atmospheric drag alone, but is a consequence of the interaction of atmosphere, ocean and ice drift under the influence of the Coriolis force. For shallow waters, this offset can be ignored and the ice follows the wind direction [Leppäranta, 2011]. Rossby and Montgomery [1935] state that for wind speed less than $2\,\mathrm{m\,s^{-1}}$, there is no explicit relation between ice motion and wind velocity, since the local wind has less influence

1 Submitted to the Journal of Geophysical Reseach, under review. The preliminary version of the article can be found in Appendix A.2.

on the ice drift than the ocean currents [Leppäranta, 2011]. In most cases the wind speed is the dominating factor, which contributes to the ice drift, while it is antagonised by the ocean drag. The ocean drag depends on the thickness of the ice and its bottom roughness. Thicker ice experiences a stronger ocean drag compared to thin ice. Since ocean currents are more stable than the wind field, the oceanic drag affects the ice drift in time scales of months and years. If only ocean and wind interact with the sea ice, the drift regime is called *free drift* [McPhee, 1980]. It is a good approximation for the drift of individual, separate ice floes or ice fields with low compactness [Leppäranta, 2011].

In the case of a closed sea ice cover or a high density of drifting ice floes, interactions with the surrounding ice take place. These interactions cause an internal stress which slows down the velocity of the drifting ice. According to Leppäranta [2011] the main stress generating processes are:

- up-breaking of pack ice into ice floes
- collision of ice floes
- shear friction between ice floes
- friction between ice blocks in pressure ice formation
- potential energy production in pressure ice formation

Spatial differences in stress give rise to forces that influence the entire velocity field. These forces have a mediating influence on the drift ice (e. g. at coastlines, where the ice might be slowed down by shear friction) and transmit momentum over large distances.

3.2 SATELLITES FOR SEA ICE OBSERVATIONS

The area covered by a sensor on the earth's surface depends on the resolution of the satellite sensor. The coarser the resolution of a sensor is, the larger is the area it covers on the earth surface. This area is called the *footprint* of the sensor. The larger the footprint of the satellite sensor is, the large is the swath width of the sensor covered along one orbit and hence the spatial coverage. Then it needs less orbits i. e. time to cover the earth surface completely. The less orbits a satellite needs to cover the earth surface, the more often it revisits an orbit position above a certain point on the earth surface.

Requirements for certain spatial and temporal resolutions depend on various aspects. With a coarse spatial resolution one can ensure a daily coverage of a region at the costs of detail. With an increase of the spatial resolution (usually coupled with a shrinking footprint), the revisiting time increases up to a few days.

For the estimation of motion of sea ice from satellite images, the consequences from this balance between the size of the footprint and the resolution of the image are as follows: If the footprint of a satellite is small, the resulting area covered by the overlap of two satellite images is small as well. The reduced temporal resolution can also cause problems if the patterns change during this period or leave the imaged overlap area due to high velocities of the ice drift. Consequently, one has to balance between the

necessary degree of detail of the drift field, the size of area for which the drift field has to be determined and the needed temporal resolution (revisiting time).

Depending on the sea ice properties and the required temporal and spatial resolution for the ice drift, different satellite sensors can be employed to observe sea ice motion. They are presented in Table 2. The data of all satellite sensors mentioned in the following can be used to calculate sea ice motion employing the methods outlined in Chapter 2. The sensors differ in the way they 'see' the sea ice and their spatial resolution. The potential sensors can be subdivided into four categories:

Spectrometers separate the visible and infrared spectra into frequency bands. The resolution of a sensor depends on its design and the spectral range. Optical and Thermal Infra-Red (VIS-TIR) sensors are mainly useful for the identification of leads or individual floes, due to the high difference in albedo and temperature between the ice and the open water. However, they are disturbed by clouds. Optical sensors cannot be employed during the polar night. This is a significant drawback.

Passive microwave sensors measure the microwave radiation of the earth surface for one or multiple defined frequencies. Because of their coarse spatial resolution, they cover the polar regions about once a day. This allows the calculation of daily ice drift products. In those satellite images, it is possible to differentiate between ice and open water, since the crystalline structure of ice typically emits more microwave radiation than the open water. The radiation is additionally influenced by the age of the ice, its salt content and other physical properties. Drift products derived from passive microwave sensors can be combined with those from scatterometer results, since they have a similar spatial and temporal resolution. This increases the reliability of the gained drift information and compensates for gaps in the retrieved drift vector fields due to a potential lack of traceable pattern in one of the satellite data sets. One example for the combination those sensors is the work by Lavergne *et al.* [2010].

Scatterometers belong to the group of *active sensors*. They send an impulse with a defined frequency and measure its response reflected from the surface. The scatterometer measures the backscatter for multiple incidence angles and a number of azimuth angles (i. e. different directions relative to the satellite track). Based on a comparison of this backscatter information it is possible to analyse in which direction the signal is scattered most. The procedure was originally developed to measure winds over the ocean, since the scatter characteristics of the ocean surface can be related to wind speed and direction. In recent years, scatterometer data have also been employed for the calculation of soil water content. For sea ice, the backscattered intensity is sensitive to the roughness of the ice surface. Depending on the used frequency band, the penetration depth varies. It increases with decreasing frequency and is a function of ice salinity, temperature, wetness, and volume structure. Hence, scattering contributions from the volume may influence the observed intensity variations in the image. Due to the long time series of available data, sea ice drift products derived from passive microwave sensors and scatterometers are excellent for climate research [Leppäranta, 2011], but given their low resolution, they are only of limited use for detailed process

Table 1: Overview over the spectral bands and their wavelength.

Band	Spectral range	Wavelength
L-band	Microwave	15 cm to 30 cm
C-band	Microwave	3.75 cm to 7.5 cm
X-band	Microwave	2.5 cm to 3.75 cm
Ku-band	Microwave	1.67 cm to 2.5 cm
K-band	Microwave	1.11 cm to 1.67 cm
TIR	Thermal Infrared	8 µm to 15 µm
MWIR	Mid Wavelength Infrared	3 µm to 8 µm
SWIR	Short Wavelength Infrared	1.4 µm to 3 µm
NIR	Near Infrared	0.78 µm to 3.0 µm
VIS	Visible Light	400 nm to 780 nm

studies related to sea ice kinematics.

Another type of active sensors is the group of *synthetic aperture radar sensors* (SAR). The acquired images have a higher spatial resolution than passive microwave sensors and scatterometers. However, swath width of SAR sensor on the ground are typically relatively small[2]. Like scatterometers, SAR sensors emit a directed beam of pulses with a defined frequency and measure the backscatter energy returning from the surface. While sensors operating in the L-band penetrate the sea ice and measure backscattering contributions from the sea ice volume as well, C-band sensors hardly penetrate the sea ice surface, and X-band sensors receive a backscatter signal which is reflected more or less directly at the sea ice surface. However, also the backscatter signal in the L- and C-band contain a surface signal. The penetration depth of the beam of pulses increases with increasing wavelength. Table 1 lists the individual bands and their respective wavelength.

Sensors which operate in the L-band acquire images that emphasise large-scale topographic features, like pressure ridges, ridges lines, fractures or rubble fields while ice floe boundaries are often less precisely identifiable than in other frequency bands. C-band satellites acquire images of sea ice with well defined ice floe shapes and high backscatter values from multi-year ice. Images acquired in the X-band emphasise similar characteristics as those acquired in the C-band with slightly increased differences between the ice types together with a slightly increased variance of the backscatter for the individual ice types [Onstott, 1992].

3.3 MOTION TRACKING OF SEA ICE

In this section, the development of sea ice motion tracking is outlined. The first manual observations of sea ice motion from satellite imagery were done in 1979 using SEASAT images [Curlander *et al.*, 1985; Hall and Rothrock, 1981]. Ninnis *et al.* [1986] were the first to estimate sea ice motion automatically from satellite images using cross correlation on AVHHR imagery[3].

2 between 20 km to 500 km, hence images from a given position can only be acquired at temporal resolutions of at least a day. An exception to this rule would be the combination ascending and descending orbits.

3 this approach was originally developed by Leese *et al.* [1971] for tracking cloud motion

Table 2: Satellite sensors employed for sea ice motion tracking. The period indicates the lifetime of the sensor or its planned lifetime. If no end is indicated, the sensor already reached the anticipated lifetime but is still operating. For sensors which are still within there anticipated lifetime, the planned end of mission is indicated.

Satellite sensor	Sensor type	Spectrum	Period
Landsat MSS	Spectrometer	VIS-TIR	1972-2010
AVHRR	Spectrometer	VIS-TIR	1978-2020
OLS	Spectrometer	VIS-TIR	1976-2009
SeaWiFS	Spectrometer	VIS-TIR	1997-2010
MODIS	Spectrometer	VIS-TIR	1999-
Envisat AATSR	Spectrometer	VIS-TIR	2002-2012
ERS-1 ESCAT	Scatterometer	C-band	1991-2000
ERS-2 ESCAT	Scatterometer	C-band	1995-2011
ASCAT	Scatterometer	C-band	2006-
NSCAT	Scatterometer	Ku-band	1996-1997
QuikSCAT	Scatterometer	Ku-band	1999-2009
SEASAT SASS	Scatterometer	L-band	1978-1978
SEASAT SAR	SAR	L-band	1978-1978
ERS-1	SAR	C-band	1991-2000
ERS-2	SAR	C-band	1995-2011
JERS-1	SAR	L-band	1992-1998
Radarsat-1	SAR	C-band	1995-
Radarsat-2	SAR	C-band	2007-
Envisat ASAR	SAR	C-band	2002-2012
ALOS PALSAR	SAR	L-band	2006-2011
TerraSAR-X	SAR	X-band	2007-
COSMO-Skymed	SAR	X-band	2007-
SMOS	Passive Microwave	L-band	2009-2014
EMSR	Passive Microwave	K-band	1972-1977
SMMR	Passive Microwave	Multiple Bands	1978-1987
SSM/I	Passive Microwave	Multiple Bands	1987-2008
SSMI/S	Passive Microwave	Multiple Bands	2003-2016
AMSR-E	Passive Microwave	Multiple Bands	2002-2011
AMSR-2	Passive Microwave	Multiple Bands	2012-2025

Subsequent studies by Fily and Rothrock [1987], Vesecky *et al.* [1988] and Collins and Emery [1988] adapted this approach for the analysis of SAR images [Emery *et al.*, 1991]. Fily and Rothrock [1987] first presented the concept of nested correlation in a resolution pyramid[4] to calculate sea ice motion automatically from SEASAT data. They point out that correlation-based pattern tracking is highly sensitive to rotation of ice floes. The sensitivity depends on the size of the correlation template: The smaller the template is, the better it can deal with rotation. However, a small template often cannot represent pattern characteristics of sea ice adequately due to its limited size. In the case of rotational motion Vesecky *et al.* [1988] suggest to to increase the reliability of sea ice drift products with the help of features/geometric primitives instead of patterns in the case of rotation. Pattern matching algorithms work sufficiently well for the central pack ice of the Arctic with its mainly

4 An introduction on the idea of resolution pyramids can be found in Chapter 4

translational motion but fails if the rotational component becomes too large, like in the marginal ice zones [Kwok *et al.*, 1990]. Daida *et al.* [1990] states that for low ice concentrations at the marginal ice zone, a feature-matching technique is needed that can address rotational and translational motion, while the compact ice masses of the central pack ice can be tracked by a pattern matching technique. Based on this background, Kwok *et al.* [1990] outlined a meta-algorithm, the Geophysical Processing System (GPS) at the Alaska SAR Facility (ASF), which used ERS-1 data and combined the pattern matching for the pack ice with the feature tracking based on correlation of the shape of ice floes for the marginal ice zone. It employed Ψ/S-Curves, as discussed by McConnell *et al.* [1991], to describe the shape of the floes by the direction of the tangent to the floe edge, plotted as a function of arc length around the curve. The GPS became operational in February 1992. The system was relatively simple by today's standards but demonstrated the concept of operational sea ice motion tracking from SAR imagery.

After the GPS was shut down after three years, its successor, the Radarsat GPS (RGPS), was set up in 1999 at the ASF. Based on Radarsat images it calculates sea ice motion in the Arctic for the full acquisition period of RADARSAT starting from November 1996 until today. The temporal sampling time of the ice drift is three days or six days, the grid spacing 5 km or 10 km [Kwok and Cunningham, 2002]. In the framework of the GlobIce project, the University College London lead the development of sea ice products for ESA. Employing Envisat data from 2004 - 2011, they calculated Arctic wide sea ice motion, deformation and mass flux at a temporal resolution of three days and a spatial resolution of 5 km. Within this project, they recently also published a beta version for an Antarctic-wide sea ice motion product, which is available for August and September 2010 only.

To provide global ice motion products, it often is necessary to fuse various low resolution datasets from various sensors. First attempts were undertaken by Agnew *et al.* [1997] and Kwok *et al.* [1998], who estimated large scale sea ice motion from SSM/I data. For the years 1979 - 1997, Schmitt *et al.* [2004] provided a sea ice drift atlas for the Antarctic, combining SSM/I and buoy data. The National Snow and Ice Data Center offers the Polar Pathfinder data for the period from 1978 to 2006 [Fowler, 2003]. The Pathfinder data is based on AVHRR, SMMR, SSM/I and buoy information of the International Arctic Buoy Program and provides global sea ice motion information at a resolution of 25 km. An operational low resolution sea ice drift product is provided by the EUMETSAT OSI SAF (European Organisation for the Exploitation of Meteorological Satellites Ocean and Sea Ice Satellite Application Facility) with a temporal resolution of two days and a spatial resolution of 62.5 km [Lavergne *et al.*, 2010].

While all studies described above mainly focus on the estimation global sea ice motion trends, Thomas [2004] presented an algorithm for the estimation of sea ice motion from SAR data with a high spatial resolution and continued its development to handle discontinuous motion [Thomas, 2008]. He demonstrated that it is possible to retrieve ice drift products with a resolution of about 400 m from ERS-1 data [Thomas *et al.*, 2008a]. His algorithm is the basis of the algorithm used in this thesis (described in Chapter 4).

Most algorithms for sea ice motion tracking are based on one of the techniques described in Chapter 2. However, there are also other approaches like the one by Banfield [1991] who outlined an algorithm focusing on the statistical tracking of floes. He employed a statistic maximum likelihood estimation based on simplified shapes from principal curves. One main drawback of all tracking schemes is their need for stable image intensity variations with sufficient contrasts between ice structures (recognised as intensity patterns). If the contrast is reduced in a way that boundaries between floes or deformation zones are no longer clearly identifiable[5], a "normal" feature tracking would fail. For these conditions Liu *et al.* [1997] suggested the use of wavelets for motion tracking.

5 a situation that occurs during summer melt

4 METHODOLOGY

The calculation of sea ice motion from satellite data requires a sequence of images that cover the same region. The time interval between the acquisitions of single images needs to be small enough to capture also faster movements of the ice. To calculate the motion, structural patterns in the ice which were identified in the first image are compared with patterns in the second image to find corresponding matches. Next, the displacement between the position of the pattern in the first image and its position in the second image is derived. The mean velocity of the sea ice is then calculated from the displacement divided by the time interval between both acquisitions.

To identify a particular pattern from the first image in the second one, one needs to scan the full extent of the second image. This is computationally inefficient. Another problem is that most similarity measures are very sensitive to high frequency noise. For gradient-based approaches, described in Section 2.1, a sequence of images has to fulfil the condition that the displacement (of a pattern) from one image to another is very small. Given the fact that the time interval between two images is in most cases at least about one day and that the ice can move up to 30 km during this time, this can cause problems. Therefore, various approaches work with a sequence of resolution levels [Adelson *et al.*, 1984; Fily and Rothrock, 1987; Sun, 2002].

The concept of using multiple versions of the same image with decreasing resolution is known as *image pyramid* or *resolution pyramid*. It is depicted in Figure 5. To construct a resolution pyramid, the original image is smoothed and re-sampled to a quarter of the original image size in terms of pixels[1]. The resulting lower-resolution image is used to calculate the next level of the pyramid. Thereby every resolution level leads to a more generalised and coarser representation of the original image. At the top of the pyramid large displacements cover only a few pixels, limiting the search area for corresponding patterns.

After the generation of the resolution pyramid, the motion of the ice field is first calculated on the coarsest resolution level. Then, the estimated displacement is employed to optimise the search direction on the next resolution level until the final displacement is calculated for the original resolution of the image. The coarser levels of the resolution pyramid contain less local variation in the image brightness patterns. Furthermore, these more general patterns do not change much between two successive images. Consequently, the resulting displacement estimation is comparatively reliable. By inheriting these displacement estimates to a higher resolution level, the algorithm is forced to search for the corresponding pattern in the inherited direction, which enforces a certain robustness against noise. *Robustness* describes the ability of the algorithm to provide reliable displacement information despite the distortion of the analysed patterns by noise.

1 The side lengths of a pixel increase by a factor of 2.

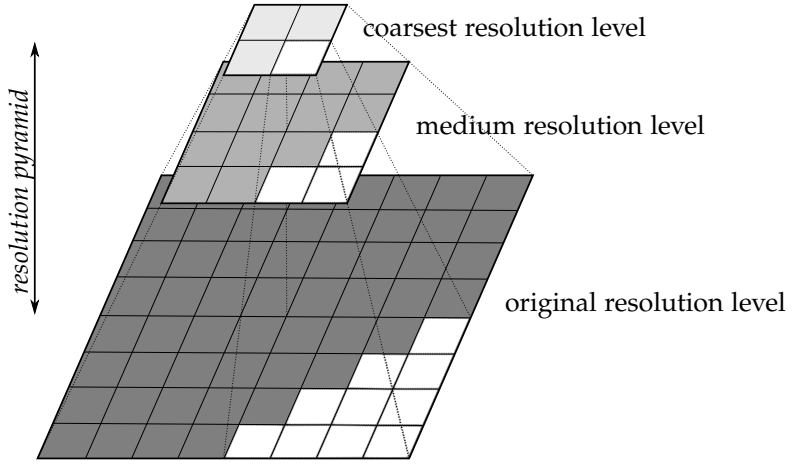

Figure 5: Formation of a resolution pyramid with three levels. The white patches symbolise a pattern of pixels which is adapted on every coarser resolution level.

The number of resolution levels depends on the resolution of the original image and on magnitude and homogeneity of the displacements within the scene. If image size and displacements are large, more resolution levels are chosen to reduce the number of calculations needed to identify matching patterns. However, sea ice is not a homogeneous medium, and single ice floes do not always move in the same direction. Therefore an image sequence may cover spatially heterogeneous drift regimes. Such fields include converging motion which leads to deformations such as e. g. ice ridges, or diverging drift which causes the formation of leads. In the case of complex small-scale motion processes, a high number of resolution levels can cause problems, since the variations in local motion might vanish in the coarse-resolution levels of the pyramid. This would enforce the retrieval of a very homogeneous but potentially wrong vector field.

4.1 THE SEARCH STRATEGY

In the following, the general concept of the sea ice motion tracking algorithm employed for this work is described. It is a modified version of an algorithm outlined by Thomas [2008]. The implemented algorithm is a pattern matching algorithm based on a correlation measure[2]. In the algorithm, the same resolution pyramid is used repeatedly to calculate the vector field. This series connection will be called *cascade*. As described in Section 2.2, pattern matching algorithms are based on templates that subdivide the first image into small areas of brightness patterns, for which they search the most similar pattern in a second image.

At the first step of the cascade, the template size is chosen according to the resolution of the image at the coarsest level of the pyramid. This initial template size in terms of pixels remains constant for all levels of one pyramid. While the template size remains constant, the image size quadruplicates with every level of the pyramid. Therefore, the area covered by a single

2 described in Section 2.2

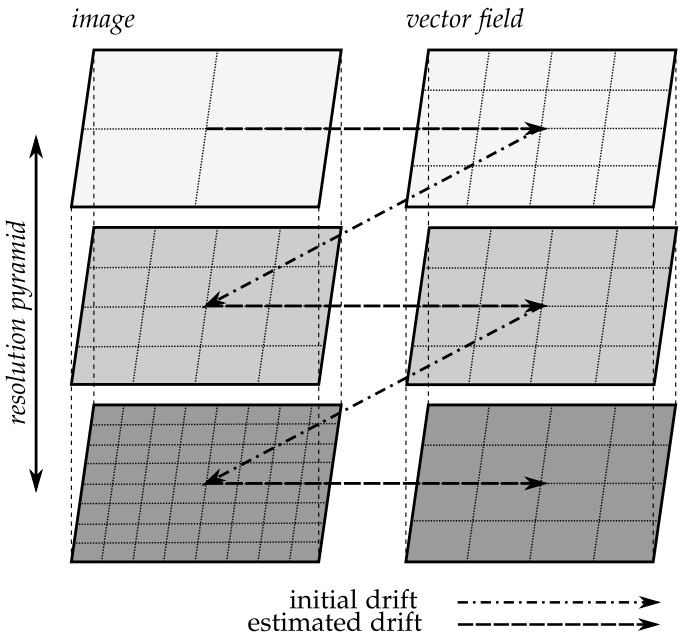

Figure 6: The drift calculation is initialised at the coarsest level of a resolution pyramid. The search template agrees with the resolution of the image a the coarsest pyramid level, containing 2×2 pixels, remaining constant for all levels of the pyramid. The resulting vector field is inherited to the next resolution level as a first guess for the displacement. Note that the drift vector field at coarser resolution levels is computed using overlapping templates.

template decreases with each level of the pyramid. At the highest resolution there exist $2^l \times 2^l$ positions $(\hat{x}, \hat{y})$, with l being the total number of resolution levels of the pyramid, for the template at which it can be positioned without overlapping with templates at neighbouring positions. As a result, the template subdivides the first image on the highest resolution level into a regular grid of $2^l \times 2^l$ template positions for which the corresponding pattern is searched in the second image. Consequently, the resulting vector field contains the same number of displacement vectors.

The resolution of the derived vector field remains constant over one pyramid. This allows to inherit search directions based on estimates from preceding stages, to find corresponding patterns (i. e. the respective displacement vectors) at the final resolution. The inheritance of vectors from the preceding resolution level to the next finer one is depicted in Figure 6.

For the calculation of the drift vectors, the algorithm works with overlapping templates. On the coarsest level, the individual template positions overlap completely. The overlap decrease starting from the coarsest level to the finest one, ensures a certain homogeneity of the drift vector field on coarser levels that decreases towards the finer levels of the pyramid. At the same time, the area of the individual template (in length units) shrinks. This causes a spatial refinement of the vector field from a more global displacement vector field on the coarsest resolution level to a more localised displacement vector field at the finest level. The decrease of the overlap over the resolution pyramid is depicted in Figure 7.

The resulting vector field at the bottom of the first resolution pyramid (i. e. the end of the first step of the cascade) is used as initial guess for the

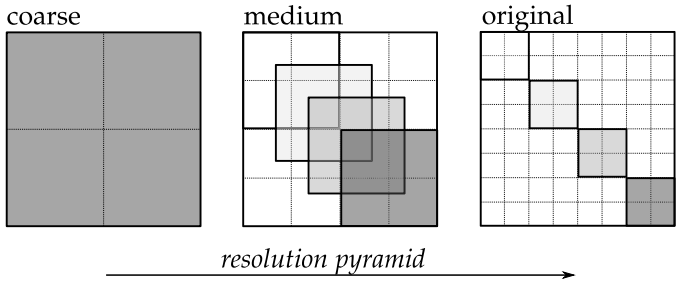

Figure 7: Decomposition of the overlap for a three-level resolution pyramid at the first stage of a cascade. The coarsest image on the left is fully covered by all four templates, in the middle, the positions of the template overlap only partly while there is no overlap on the highest resolution.

subsequent cascade step, starting on the coarsest level of the next resolution pyramid. For each new step of the cascade, the length of the template is halved. Hence, in a second step, the template covers only a quarter of the image at the coarsest resolution level and the resolution of the vector field quadruples. In the following, the resolution of the resulting vector field quadruplicates with every additional run of the cascade. The process of motion decomposition is depicted in Figure 8, which illustrates the principle of vector field inheritance for a cascade with two stages and a resolution pyramid with three levels.

The resolution of the final vector field can be calculated according to the number of resolution levels l and number of cascade stages c:

$$\text{resolution} = 2^{l+c-2} \times 2^{l+c-2}. \tag{13}$$

Additionally, the resolution of the final vector field is limited by the number of pixels needed per template for a reliable correlation. The total number of pixels covered by the template[3] should not fall below a value of 75 to 100 pixels and both side lengths of the template should not be below 6 pixels. Otherwise, the patterns loose their specific characteristics required for a reliable matching.

Pattern matching can fail. In this case it leaves either a gap in the vector field, if no corresponding pattern was found, or a wrong displacement vector if a wrong pattern was matched. Therefore, the algorithm includes a filtering and interpolation step before the derived vector field is inherited to the next level. The vector field is smoothed with a median filter to suppress outliers caused by potentially wrong matching results. Occurring gaps in the drift vector field are filled by interpolating between the surrounding drift vectors after filtering potential outliers.

The employment of the resolution pyramid allows the tracking of large displacements and improves the robustness of the matching algorithm against noise. By using multiple resolution pyramids in series (cascade), an additional feature is added to the algorithm. Since the calculated drift from the preceding pyramid is evaluated again on the coarsest resolution level of the next step of the cascade, it enables the algorithm to refine the vector field for a smaller region of the image. While preserving the advantages of the resolution pyramid, the use of the cascade allows the algorithm to deal with counteracting displacements in an image sequence, which might have been

3 the aspect ration of the template agrees with the aspect ratio of the image

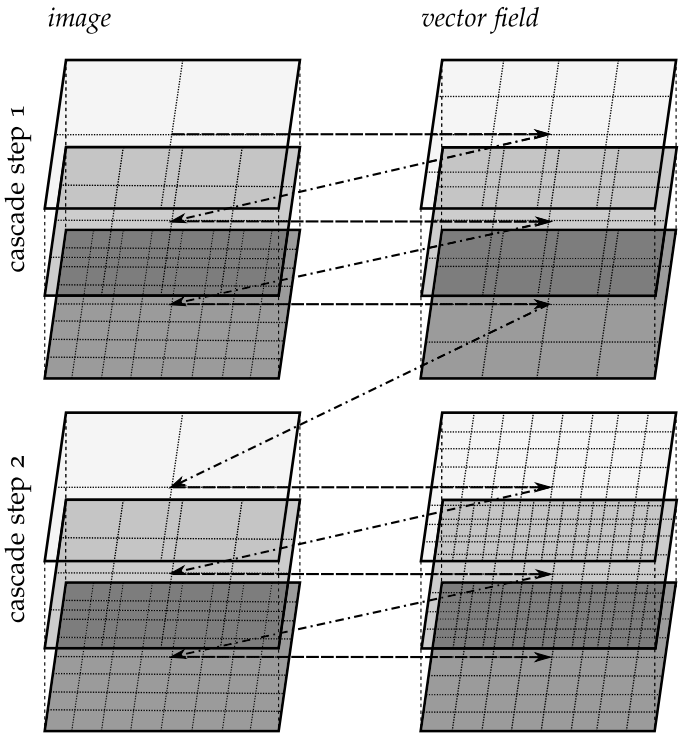

Figure 8: Design of multi-scale algorithm. The drift calculation is initialised at the coarsest level of a resolution pyramid. The resulting vector field is inherited to the next resolution level as a first guess for the displacement. The results of the first run through the image pyramid are afterwards used as initial displacement information on the subsequent stage of the cascade.

suppressed in a single pyramid with additional resolution levels.

Thomas *et al.* [2008b] suggested an overlap of the templates on the highest resolution level of the pyramid of about 50 %. This would enforce a certain agreement between neighbouring vectors in the vector field. In contrast, the author decided to eliminate this overlap on the final level of the pyramid. This reduces the enforced similarity between neighbouring vectors on the final resolution level and reduces the template size relative to the image. Furthermore, it decreases the number of computations for a vector field.

4.2 THE SIMILARITY MEASURE

The core element of every pattern matching algorithm is the identification of corresponding patterns in two consecutive images. This can be achieved as the minimisation of a cost function for a chosen similarity measure, as described at the beginning of Section 2.2. The corresponding pattern in the second image is found by moving a template g, covering a certain pattern from the first image, over the second image. For every position of template g on the second image, the similarity between g and the underlying area $h_{\bar{u},\bar{v}}$ of the second image is calculated. For each position of the template, the similarity values are stored on a grid determined by the shift of the template over the second image, hence forming a surface. A peak in the

surface indicates the position where a pattern in the second image is most similar to the pattern from the first image, which is contained in template g. The difference between the origin of the template in the first image and the position of the peak in the second image is the displacement of the pattern in the template. In contrast to most other motion tracking algorithms, the implemented method evaluates the similarity between two patterns based on two measures. It employs a normalised cross-correlation (NCC) with a pre-posed phase correlation (PC).

A problem arises when single parts of a pattern covered by the template g in the first image move into different directions. When matching the corresponding patterns in both images, the surface formed by the cost function exhibits multiple peaks which are relatively small. This means that no distinctive peak can be found at the position where a pattern from the second image is most similar to the pattern covered by the template in the first image. This lack of significant peaks is related to the aperture problem, which was described in Section 2.1. It states that the true displacement of a template can not be estimated clearly if the structure covered by the template is ambiguous. Therefore, selecting the maximum of the cost function surface does not necessarily provide the best estimate [Thomas *et al.*, 2008a].

Compared to the NCC, the PC is relatively robust in the presence of non-linear motion as well as to noise that is correlated to the image function, such as uniform variations of illumination or offsets in average intensity [Foroosh *et al.*, 2002; Thomas *et al.*, 2005]. An additional advantage of the PC is its high computational performance, since it can easily be calculated in the Fourier domain and shows distinct peaks. The main advantage of the NCC is its higher robustness towards high frequency random noise compared to the PC [Manduchi and Mian, 1993].

With the combination of these measures in the search for corresponding patterns, one takes advantage of both methods. This is done by a candidate selection process. First, the potential positions of the template in the second image are identified with the PC. Afterwards, these candidate positions are tested with the NCC. The position of the candidate peak with highest correlation coefficient for the NCC indicates the best guess for a correspondence between two patterns.

In the candidate selection process, the phase correlation surface shows one distinct peak, if the pattern to be matched does not change between the first and the second image. The surface reveals multiple peaks, if some parts of the pattern moved to another direction than others. Additional peaks on the surface can be introduced by noise. Compared to Thomas *et al.* [2008b], the author modified the candidate selection. The former considers every value as a candidate whose PC-value is greater than 75 % of the maximum of the phase correlation surface. This includes not only the maximum of a (local) peak but also all adjacent positions belonging to this peak with values greater than 75 % of the global maximum. In contrast to this, the author only takes into account the position of the local maxima but not their neighbouring values and considers all peaks greater than 25 % of the global maximum. Depending on the correlation surface and the steepness of the individual peaks this can reduce the number of candidates significantly.

By considering additional local maxima as candidates, the influence of high frequency noise on the final result is reduced. The influence of the more noise-robust NCC on the candidate selection scheme is strengthened.

Additionally, the author introduced a simple noise detector which ensures that the candidates of the PC are only analysed with the NCC measure if less than 25 % of the whole phase correlation surface is regarded as a potential candidate. It filters cases in which the correlation surface becomes so noisy that no distinct peaks can be identified. Following Carneiro and Jepson [2003], the author added 0.05 to the denominator of the PC[4] to cut off frequencies with very low amplitudes.

This candidate-based selection scheme has two central advantages. First, it ensures a certain robustness against non-linear motion while taking advantage of the fast calculation in the Fourier domain. Second, it adds the better robustness of the NCC against various kinds of high frequency noise (Gaussian, Speckle, Salt-and-Pepper) to the algorithm [Thomas *et al.*, 2008b].

4.3 THE CONSISTENCY CHECK

For the data sets analysed in this work, no drift buoy data were available to assess the accuracy of the retrieved drift vector fields. Hence the author needed to devise a method in order to assess the reliability of the sea ice drift data in a different way. In the following, three methods to analyse the reliability of the sea ice motion data, based only on the available image data, will be introduced.

The first method is manual evaluation. Displacement vectors for the image pairs are measured by hand and then compared with the automatically estimated drift fields. The accuracy of the manual measurements depends on the quality of the images and the structural brightness changes between them. However, it is reasonable to assume that the accuracy of manually measured displacements is ± 1 to 2 pixels at minimum.

In the third paper, the author proposes two intrinsic measures which can be calculated automatically by the algorithm to provide quality estimates for the created drift product [Hollands *et al.*, 2012a]. This quality information help to assess if the correspondences found by the algorithm are trustworthy or if the algorithm might have failed.

The results of the matching algorithm might not be trustworthy for two reasons. Either there are not enough characteristic patterns in the image for matching, or the displacements during the time between both images was to large to track them. The algorithm fails e. g. if a certain ice pattern left the overlapping scene in the time between the acquisition of two images or if existing patterns were deformed. While a texture within the template can be analysed before the matching to assess if it contains distinct structural elements for a successful correlation, the errors caused by the the sea ice motion itself (e. g. deformation, forming of leads) need meta-information. This meta-information on the sea ice drift is only available from the tracking procedure. Therefore the proposed measures handle both cases individually.

The reliability of a calculated displacement is evaluated with a measure that describes how trustworthy a pattern and the calculated correlation are. This measure is called *confidence factor* (CFA). For every pattern analysed at a given level of a resolution pyramid, a score is assigned to the CFA. This score is based on a threshold for the correlation coefficient and its reliability linked to the number of pixels in the template, a threshold for randomly positioned bright intensity spots caused by mirror reflections from the sea ice that could

4 Equation (12) in Section 2.2

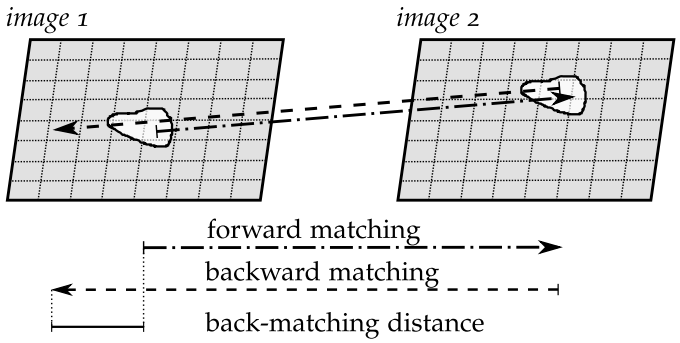

Figure 9: Back-matching. The difference between forward matching and backward matching is the back-matching distance. If a found correspondence is consistent, the back-matching distance is small. The grid exemplifies the resulting vector field. Each cell represents a displacement vector calculated from the image sequence.

distort a successful tracking, and three thresholds for texture measures. If threshold values are exceeded, then the score is incremented by one. The resulting score is accumulated over the different levels of the pyramid and the entire cascade and is normalised to the number of matching calculations performed for the individual template. This results in a CFA map which indicates the reliability of the found match and the resulting displacement.

Furthermore, the reliability of a match is assessed by a technique called back-matching, which is illustrated in Figure 9. It is a check which analyses the overall consistency of the calculated displacement vector field and thereby also identifies problems which are neither related to the texture nor to the correlation. The back-matching is based on two runs of the algorithm with the same two images. In a first step, the vector field is calculated in the normal way, which results in a regular grid of templates in the first image, whose nodes are linked to positions in the second image. In a second step, the order of the images is changed. Now the originally second image is subdivided into a regular grid of templates while their corresponding patterns are searched in the first image. This second vector field is now inverted and re-sampled to the grid of the vector field based on found pattern displacements relative to the first image. Since only the order of the images is changed, the resulting vector field from the reversed-order image pair should agree with the drift vector field estimated in the first step. Strong differences between the “forward” and “backward” calculation of the drift vector field indicate regions with low reliability.

5 SCOPE OF THE PAPERS

PAPER 1: *Thomas Hollands and Wolfgang Dierking. (2011) "Performance of a multi-scale correlation algorithm for the estimation of sea ice drift from SAR images: initial results", Annals of Glaciology, 52 (57), pp. 311-317.* **[published]**

The authors describe the implementation and modification of a sea ice motion tracking algorithm. The original algorithm was developed for high resolution motion tracking in the Arctic. The algorithm was applied to a test side in the south western Weddell sea, north of the Filchner-Ronne Ice Shelf, Antarctica. The authors validated the results based on manually measured displacement vectors. They found that the correlation coefficient depends on the texture of the images. From a geophysical perspective, the most interesting aspect of this paper is the observation of ice drift regimes, which changed completely within a single day. This observation underlines the need for a temporally dense coverage of sea ice regions in order to calculate the true motion of the ice. Based on a series of five images covering a time period of eight days, the authors found and validated four completely different drift situations and were able to link it with the highly variable wind conditions during the observation period. Additionally, the authors compared sea ice drift vector fields estimated from satellite images of different resolution and found comparable drift characteristics.
For this paper, the responsible author implemented and modified the multi-scale sea ice motion tracking algorithm[1], validated it based on seven image pairs, undertook the described analysis of the data and wrote the manuscript. The co-author contributed to the data analysis and improved the manuscript.

PAPER 2: *Thomas Hollands, Verena Haid, Wolfgang Dierking, Ralph Timmermann and Lars Ebener (2012) Sea ice motion at the Ronne Polynia, Antarctica: SAR observations vs. model results, Journal of Geophysical Research.* **[under review]**

The authors present a comparison of satellite based observations and model results for the Ronne Polynia. The employed model is a global coupled sea-ice-ocean model of the Alfred Wegener Institute called FESOM (Finite Element Sea Ice Ocean Model). The authors studied the difference between observed and modelled polynia extent and compared the difference of modelled and observed ice drift in magnitude and direction, developed a specific presentation of drift vector statistics based on polar plots. The main contrast to studies of other authors like Pease [1987], Haarpainter *et al.* [2001] or Krumpen *et al.* [2011] who studied polynias is that the authors employed the results of a global coupled sea ice ocean model instead of a local flux model which allows to consider the interaction with factors such as the spatial water-land distribution and the specific ice conditions (concentration, thickness, degree of deformation, extent) that may influence the evolution of a polynia. Furthermore, they studied the outcome of the model for different atmospheric forcing of different spatial and temporal resolu-

1 described in Chapter 4

tion. Focusing on the development of the polynia area and on variations of polynia extent, the authors found that the results of FESOM reproduce these parameters well. For the magnitude and direction of the wind data, the results for time periods with heterogeneous wind conditions are better modelled if the model employs an atmospheric forcing with a high temporal and spatial resolution, whereas the model results for periods with more homogeneous wind conditions are relatively independent from the resolution of their atmospheric forcing. For most test cases, the magnitude of the modelled drift is smaller than the observed one, while the turning angles are slightly too large. Given the fact that the authors also observed relatively high wind-speed/ice-velocity ratios, this could be a hint that the atmospheric forcing generally underestimates the actual wind speed.
For this paper the author calculated the vector fields from satellite images and compared the results with the modelled vector fields provided by Verena Haid. The author calculated, described and discussed the differences between observations and model and drew the respective conclusions. The co-authors were involved in the interpretation of the data and reviewed and supplemented the manuscript, written by the author. The model description of FESOM was written by Verena Haid.

PAPER 3: *Thomas Hollands, Stefanie Linow and Wolfgang Dierking (2012), Reliability measures for sea ice motion retrieval from synthetic aperture radar images images, Journal of Selected Topics in Applied Earth Observations and Remote Sensing.* **[manuscript prepared for submission]**

The authors advance an aspect from the study described in Paper 1, in which they found a relation between the entropy within a template and the resulting correlation coefficient. They show that the correlation coefficient has only limited significance for the evaluation of the calculated vector field and its reliability. Therefore they propose a measure called confidence factor (CFA), which is based on a combination of correlation and various texture measures. It indicates regions were the correlation coefficient is less or more reliable based on the texture in the respective region. It is described in Section 4.3. Since other effects influence the reliability of the drift field as well, we applied a method to check the consistency of a calculated vector field called back-matching, which is also described in Section 4.3. Combined with the developed CFA, the authors can identify regions where the algorithm works reliably as well as regions where the algorithm fails. By employing a simple classification based on the developed reliability measures, the authors can explain, whether a potential uncertainty in the drift calculation for a certain region is a lack of image patterns for correlation or a lack of constancy of the image patterns (ice structure).
The author developed the ideas for the CFA. Moreover, the author tested the included statistic measures for their eligibility and potential thresholds for the individual measures which could potentially indicate a less reliable correlation. Furthermore, the author adopted the idea of back-matching from photogrammetric techniques he employed during his diploma thesis. The co-author Stefanie Linow prepared the algorithm for batch processing, and implemented the back-matching and the final version of the CFA. Together with her, the author performed a simple classification to study individual regions in the analysed sequences of images. The third author contributed to the analysis of the results and helped in writing of the manuscript.

6 SYNOPSIS

The major goal of this study was to extend the use of high-resolution radar images for the validation of sea-ice-ocean models, here in particular focusing on sea ice drift. To this end, the author implemented an algorithm to track high resolution sea ice motion, which was first described by Thomas *et al.* [2008b] and modified by Hollands and Dierking [2011]. The modified version of the algorithm has been employed for all studies within the framework of this dissertation and is described in Chapter 4. In the first article, the authors evaluated the performance of the modified algorithm and studied the effect of temporal resolution on the retrieval of the actual motion. Additionally, they presented drift vector fields at spatial resolutions of a few hundred metres to about one kilometre. First studies were undertaken to analyse the relation between the value of the correlation measure and composition of the correlated image patterns.

The application of ice drift data retrieved from satellite imagery for the validation of coupled sea-ice-ocean models was realised in the second paper. Specifically, it focusses on the complex ice movement on scales of 2 km to 5 km during the formation of a polynia. In the model the drift was simulated based on different atmospheric forcings. Moreover, the authors discussed differences in the observed and simulated width of the polynia [Hollands *et al.*, 2012b].

In order to use ice drift data derived from satellite imagery for model validation, it is necessary to be aware of their reliability. To ensure the consistency of the measured displacement, the author collected various displacement vectors manually [Hollands and Dierking, 2011; Hollands *et al.*, 2012b]. Manual drift measurements can be employed to validate an algorithm, but not as a regular tool to provide information on the reliability of automated drift calculations. Therefore, a second objective of this thesis was to provide intrinsic, automatically computable reliability measures to assess the quality of calculated drift fields. Reliability information of estimated sea ice motion is e. g. essential not only for the comparison of the sea-ice motion vectors retrieved from satellite imagery with model simulations, but also for operational sea ice mapping and the assimilation of data into numeric models. Consequently, in his third paper, the author proposed two automated methods which provide some estimate on the reliability of individual displacement vectors [Hollands *et al.*, 2012a].

The calculation of sea ice drift from satellite images has now been carried out for about thirty years. One relatively new aspect, however, which also has been considered in this thesis, is the need for high resolution sea ice motion products for comparison with recently developed sea ice models, simulating ice motion on comparable scales. Earlier studies compared satellite observations and model simulations at spatial resolutions of tenths of kilometres. In contrast, the author studied the differences on scales at which local process studies on sea ice kinematics become feasible. Hollands *et al.*

[2012b] were one of the first to analyse the ice drift in a polynia region based on a comparison of sea ice drift from satellite observations and a coupled sea-ice-ocean model. Other studies like those by Pease [1987], Haarpainter *et al.* [2001] or Krumpen *et al.* [2011] compared the result of local flux models with observed ice drift. However, these simple models neglect important factors that can influences the evolution of a polynia such as the spatial water-land distribution and the specific ice conditions (concentration, thickness, degree of deformation, extent). These interactions are included in the coupled sea-ice-ocean model used in Hollands *et al.* [2012b], which makes there comparisons more realistic.

7 OUTLOOK

7.1 POLYNIA RESEARCH

The author will continue and extend the study described in Hollands *et al.* [2012b] in the framework of a Postdoc project, which deals with the satellite-based exploration of polynias in the Arctic and Antarctic. Polynias are open water areas in the sea ice, with a size ranging between 10 km^2 to 100 000 km^2. The project focuses on so called coastal polynias that occur frequently along many coasts in the Arctic and Antarctic when offshore winds move the sea ice away from the coastline. Due to their great importance for the understanding of the interaction between ocean, sea ice and atmosphere, polynias have widely been studied. Since the width of polynias varies from a few hundred metres to hundreds of kilometres, however, a number of studies emphasise the need for high resolution satellite data in order to analyse polynia processes.

In the frame of the project, the author will develop and improve methods which allow to derive the state and dynamics of a coastal polynia from satellite data. He will study the potential of future sensors and their combination for polynia research based on the data provided by their predecessors. This will include the analysis of Envisat ASAR data (as preparation of using data from its successor Sentinel-1), Envisat AATSR (in preparation for Sentinel-3) and hyper-spectral images from MODIS as link to EnMAP[1] as well as data from passive microwave sensors. The information about the polynia dynamics retrieved from the fusion of this data will afterwards be compared with model calculations and (if possible) with field campaigns. The individual goals of the project are:

- Improvement of ice type classification in regions of coastal polynias.
- Improvement of sea ice motion in the polyias and the adjoining pack ice regions.
- Analysis of the potential of high resolution SAR imagery for the identification of rafting, ridges and leads in the neighbourhood of polynias combined with an analysis of the drift vector field.
- Observation of thin ice thickness in polynias based on passive microwave sensors and data from Envisat AATSR and its successor
- Improvement of sea ice model simulations by comparison with the results of the satellite data analysis.

One important aspect for the analysis of polynias from satellite images is the identification of different ice classes in and around the polynia. Therefore, apart from its scientific benefit, the project also includes potential applications

1 EnMap is a hyperspectral satellite, which is going to be launched in 2015. It will operate at spectral bands between 420 nm to 2450 nm, which corresponds to the visual and infrared range.

for shipping and offshore logistics. The ice type classification is also used for the preparation of ice charts. Consequently, a cooperation with the German ice service (at the BSH) has been arranged. To ensure the future availability of the required satellite data, a strategy for the systematic acquisition of satellite data over key areas in the polar coastal regions will be developed within the framework of the project.

7.2 IMPROVEMENTS OF MOTION TRACKING

In the project outlined above, the development of sea ice motion tracking will continue in close co-operation with partners working in the framework of the EU-Project SIDARUS. The algorithm developed during this thesis works reliably if temporal changes of structures are negligible in the sea ice for the time between the acquisition of the images. It can handle translational motion, but due to its design it is not able to track rotational motion. This limits the application of the algorithm to central pack ice areas and causes errors if individual floes rotate. To solve the problem of rotation Berg *et al.* [2011] propose an extension for the algorithm based on a Fourier-Mellin transform of the images. This way the algorithm can handle the rotational motion of individual floes at the marginal ice zone. Another approach is the additional implementation of feature tracking to form a meta-algorithm similar to Kwok *et al.* [1990].

Another aspect of the future work within SIDARUS will be the identification of deformation zones at high spatial resolution based on the calculation of the strain-rate invariants from the calculated vector field. This follows Lindsay *et al.* [2003] and was already anticipated by Hollands and Dierking [2010].

A third field of further study is to extend the development of reliability measures for the retrieved drift vector field. This allows for the assessment of the drift information quality in absence of in-situ validation data as shown by Hollands *et al.* [2012b]. Various measures have already been proposed, mainly focusing on the evaluation of the texture or the reliability of the correlation. Kwok *et al.* [1990] use the texture variance to identify regions that contain patterns suitable for matching, while Karvonen [2012] analyses the correlation function. The need to evaluate the reliability of a match has been discussed for many years in geodetic photogrammetry. The differences between pattern matching for motion tracking and the identification of corresponding points in a stereo scene are quite small. To improve the reliability of matches for the extraction of three-dimensional models from stereo imagery, various constraints limit the area of the search and thereby reduce the risk of wrong correspondences. These are the epipolar constraint, the limitation of the disparity range, the uniqueness constraint, the smoothness constraint and the ordering constraint [Schreer, 2005]. Only the latter four can be transferred to sea ice motion tracking. They will be explained in the following.

If the depth (distance between the object closest to the lens and the object furthest away from the lens) of a three dimensional scene is known, it is possible to limit the disparity range for photogrammetric operations since the potential positional differences between two scenes of a stereo image are limited. In a stereo scene, pixels have different positions in both images due to depth changes. Compared to motion tracking from satellite images, this

corresponds to the displacement of patterns due to motion. In the case of sea ice, the limitation of disparity range complies for example with a limitation to a range of pixel displacements that are physically feasible. Leppäranta [2011] states that the velocity of sea ice motion ranges between $1\,\mathrm{cm\,s^{-1}}$ to $100\,\mathrm{cm\,s^{-1}}$. Given a temporal resolution of one day and a spatial resolution of the satellite sensor of 150 m, this corresponds to a displacement of the pattern between 5.76 to 576 pixels. Displacements larger than 576 pixels are then eliminated since they are physically unlikely. Using informations about regional wind speed and direction, the disparity range can be limited more efficiently.

The uniqueness constraint states that a pattern can only have one corresponding partner in both images. Therefore it is not possible that a pattern in the second image corresponds to multiple patterns in the first image. This general assumption holds even in the case of ice drift, which might include zones of converging motion and lead to the deformation of patterns.

The smoothness constraint states that the displacement of neighbouring points differ only in a limited range. For sea ice motion, this means that the differences in velocity between two neighbouring pixels should not be too large. It has however to be kept in mind, that this assumption is not true for discontinuous sea ice motion. This constraint is to a certain degree covered by Thomas *et al.* [2008b], who employed the calculation of strain-rate invariants for the identification of discontinuities in the ice drift field. Furthermore, it is similar to the test on smoothness, used by Kwok *et al.* [1990] as a consistency check.

The fifth constraint is the so called ordering constraint, stating that the order of patterns in a scene can be assumed to be constant. Even if this assumption is, strictly spoken, only true for non-moving patterns in the case of stereo imagery, it can be transferred to the observation of translational motion. An ice structure can not overtake another structure which lies on its drift path other than by rotation.

Together with other parameters which focus on the texture and the reliability of the correlation, these constraints can be used to enhance the performance of the matching algorithm.

One open issue is to analyse different image data acquired at different frequencies and polarisations. The expectation is that certain sea ice structures are more emphasised in curtain images than in others, dependent on radar frequency, polarisation and incidence angle. Hence patterns would be more stable in certain image types. The research presented here was conducted using single polarised C-band data of Envisat ASAR. Onstott [1992] observed that L-band images emphasise large-scale topographic features like pressure ridges, ridge lines, fractures or rubble fields. C-band satellites acquire images with well defined ice floe shapes and high backscatter values from multi-year ice. It is speculated that the performance of the sea ice motion algorithm will be improved with data from the successor for the ALOS PALSAR sensor or the Argentine SAOCOM satellites, which will all operate in the L-band. When using multiple polarisations, it might be helpful to combine them to a image product which emphasises some structures more clearly than a single band. A first guess how to do this, would be to have a look at photogrammetric strategies to match colour images or the application of a principal component analysis, where the first component contains the majority of the information from the different polarisations.

A second open issue is the combination of various sensors and resolutions. As the author showed in the frame of this thesis, there is a need for a high temporal resolution to derive detailed sea ice motion from satellite imagery [Hollands and Dierking, 2011; Hollands *et al.*, 2012b]. Moreover, it has been described by Hollands and Dierking [2011] that patterns at different resolutions can be comparable. This leaves the question if data at different resolutions can be combined into an image sequence by sub-sampling the data with the higher resolution to the resolution of the coarser one. Because different sensor types emphasis different structures of the sea ice, it is hardly possible to combine data from different sensors in an image sequence. A combination of sensors operating in the same frequency band (e. g. Envisat ASAR, Radarsat-1 and Radarsat-2 or TerraSAR-X and COSMO-Skymed), however, might be a promising approach to increase the temporal resolution.

BIBLIOGRAPHY

Adelson, Edward H., Charles H. Anderson, James R. Bergen, Peter J. Burt and Joan M. Ogden

1984 'Pyramid methods in image processing', *RCA Engineer*, 29, 6, pp. 33–41.

Agnew, Tom A., Hao Le and Thomas Hirose

1997 'Estimation of large-scale sea-ice motion from SSM/I 85.5 GHz imagery', *Annals of Glaciology*, 25, pp. 305–311.

Banfield, Jeffrey D.

1991 'Automated Tracking of Ice Floes: A Stochastic Approach', *IEEE Transactions on Geoscience and Remote Sensing*, 29 [6Nov. 1991], pp. 905–911, ISSN: 0196-2892, DOI: 10.1109/36.101369.

Barron, John L., David J. Fleet and Steven S. Beauchemin

1994 'Performance of Optical Flow Techniques', *International Journal of Computer Vision*, 12 [1Feb. 1994], pp. 43–77, DOI: 10.1007/BF01420984.

Beauchemin, M., K. P. B. Thomson and G. Edwards

1996 'Edge detection and speckle adaptive filtering for SAR images based on a second-order textural measure', *International Journal of Remote Sensing*, 17, 9 [June 1996], pp. 1751–1759, DOI: 10.1080/01431169608948737.

Berg, Anders, Leif E. B. Eriksson, Karin Borenäs and Henrik Lindh

2011 *Observations and Analysis of Sea Ice Motion with the Ice Buoy DRIVA during the 2010 Spring Field Campaign in the Bay of Bothnia*, tech. rep. 7, Chalmers University of Technology, Göteborg, Sweden, p. 20, http://publications.lib.chalmers.se/records/fulltext/local_147945.pdf.

Brennecke, Wilhelm

1921 *Die ozeanographischen Arbeiten der Deutschen Antarktischen Expedition 1911–1912*, vol. 39, Archiv der Deutschen Seewarte, 1, Hammerich and Lesser, 216 pp.

Brown, Lisa Gottesfeld

1992 'A survey of image registration techniques', *ACM Computing Surveys*, 24 [4Dec. 1992], pp. 325–376, DOI: 10.1145/146370.146374.

Burt, Peter J. and Edward H. Adelson

1983 'The Laplacian Pyramid as a Compact Image Code', *IEEE Transactions on Communications*, 31 [4Apr. 1983], pp. 532–540, ISSN: 0090-6778, DOI: 10.1109/TCOM.1983.1095851.

Canty, Morton John

2007 *Image Analysis, Classification and Change Detection in Remote Sensing: With Algorithms for Envi/Idl*, CRC/Taylor & Francis, 348 pp., ISBN: 0-8493-7251-8.

Carneiro, Gustavo and Allan D. Jepson

2003 'Multi-scale Phase-based Local Features', in *Proceedings of the IEEE Computer Society Conference on Computer Vision and Pattern Recognition*, ed. by Danielle Martin, vol. 1, pp. I–736–I–743, ISBN: 0-7695-1900-8, DOI: 10.1109/CVPR.2003.1211426.

Carsey, Frank D.

1992 *Microwave Remote Sensing of Sea Ice*, ed. by Frank D. Carsey, Geophysical Monograph, 68, American Geophysical Union, Washington DC, U.S.A., p. 462, ISBN: 0-87590-033-X.

Carsey, Frank D., Rodger G. Barry and Wilford F. Weeks

1992 'Introduction', in Carsey [1992], chap. 1, pp. 1–7, ISBN: 0-87590-033-X.

Collins, Michael J. and William J. Emery

1988 'A Computational Method for Estimating Sea Ice Motion in Sequential Seasat Synthetic Aperture Radar Imagery by Matched Filtering', *Journal of Geophysical Research*, 93, C8, pp. 9241–9251, DOI: 10.1029/JC093iC08p09241.

Curlander, J.C., B. Holt and K. Hussey

1985 'Determination of sea ice motion using digital SAR imagery', *IEEE Journal of Oceanic Engineering*, 10, 4 [Oct. 1985], pp. 358 –367, DOI: 10.1109/JOE.1985.1145134.

Daida, Jason, Ramin Samadani and John F. Vesecky

1990 'Object-Oriented Feature-Tracking Algorithms For SAR Images of the Marginal Ice Zone', *IEEE Transactions on Geoscience and Remote Sensing*, 28 [4July 1990], pp. 573–589, DOI: 10.1109/TGRS.1990.572956.

Eckstein, Adric and Pavlos P Vlachos

2009 'Digital particle image velocimetry (DPIV) robust phase correlation', *Measurement Science and Technology*, 20, 5 [Apr. 2009], p. 14, DOI: 10.1088/0957-0233/20/5/055401.

Ekman, V. W.

1902 'Om jordrotationens inverkan påvindströmmar i hafvet', *Nyt Magasin för Naturvidenskab B*, 40, 1.

Emery, W. J., C. W. Fowler, J. Hawkins and R. H. Preller

1991 'Fram Strait Satellite Image-Derived Ice Motions', *Journal of Geophysical Research*, 96, C3, pp. 4751–4768, DOI: 10.1029/90JC02273.

Fily, M. and D. A. Rothrock

1987 'Sea Ice Tracking by Nested Correlations', *IEEE Transactions on Geoscience and Remote Sensing*, GE-25, 5 [Sept. 1987], pp. 570–580, DOI: 10.1109/TGRS.1987.289836.

Foroosh, Hassan, Josiane B. Zerubia and Marc Berthold

2002 'Extensioon of Phase Correlation to Subpixel Registration', *IEEE Transactions on Image Processing*, 11 [3Mar. 2002], pp. 188–200, ISSN: 1057-7149, DOI: 10.1109/83.988953.

Fowler, C.

2003 *Polar Pathfinder Daily 25 km EASE-Grid Sea Ice Motion Vectors*, National Snow and Ice Data Center, http://nsidc.org/data/nsidc-0116.html.

Geiger, Cathleen A., William D. Hibler III and Stephen F. Ackley

1998 'Large-scale sea ice drift and deformation: Comparison between models and observations in the western Weddell Sea during 1992', *Journal of Geophysical Research*, 103, C10 [Sept. 1998], pp. 21893–21913, DOI: 10.1029/98JC01258.

Gonzalez, Rafael C. and Richard E. Woods

2008 *Digital Image Processing*, ed. by Marcia J. Horton, 3rd ed., Pearson Education, Inc., Upper Saddle River, New Jersey, 954 pp., ISBN: 0-13-505267-X.

Haarpainter, Jörg, Jean-Claude Gascard and Peter M. Haugan

2001 'Ice production and brine formation in Storfjorden, Svalbard', *Journal of Geophysical Research*, 106, C7 [July 2001], pp. 14001–14013, DOI: 10.1029/1999JC000133.

Hader, Markus

1996 'Dynamik, Rauhigkeit und Alter des Meereises in der Arktis - Numerische Untersuchungen in einem großskaligen Modell', *Berichte zur Polarforschung*, 1996, 203, ed. by Franz Riemann, ISSN: 0176-5027, http://hdl.handle.net/10013/epic.10204.d001.

Hall, R.T. and D.A. Rothrock

1981 'Sea Ice Displacement From Seasat Synthetic Aperture Radar', *Journal of Geophysical Research*, 86, C11, pp. 11078–11082, DOI: 10.1029/JC086iC11p11078.

Hollands, Thomas and Wolfgang Dierking

2010 'Monitoring of sea ice drift and deformation with SAR satellite data', in *Proceedings of ESA Living Planet Symposium, 28 June - 2 July 2010, Bergen, Norway*, ed. by H. Lacoste-Francis, vol. SP 686, CD-ROM, European Space Agency, ESA Communication Production Office, http://hdl.handle.net/10013/epic.36767.

2011 'Performance of a multiscale correlation algorithm for the estimation of sea ice drift from SAR images: initial results', *Annals of Glaciology*, 52, 57 [May 2011], pp. 311–317, DOI: 10.3189/172756411795931462.

Hollands, Thomas, Stefanie Linow and Wolfgang Dierking

2012a 'Reliability measures for sea ice motion retrieval from synthetic aperture radar images images', *Journal of Selected Topics in Applied Earth Observations and Remote Sensing*, manuscript prepared for submission.

Hollands, Thomas, Verena Haid, Wolfgang Dierking, Ralph Timmermann and Lars Ebener

2012b 'Sea ice motion at the Ronne Polynia, Antarctica: SAR observations vs. model results', *Journal of Geophysical Research*, under review.

Horn, Berthold K. P. and Brian G. Schunck

1981 'Determining Optical Flow', *Artificial Intelligence*, 17 [Aug. 1981], pp. 185–203, DOI: 10.1016/0004-3702(81)90024-2.

Karvonen, J.

2012 'Operational SAR-based sea ice drift monitoring over the Baltic Sea', *Ocean Science*, 8, 4, pp. 473–483, DOI: 10.5194/os-8-473-2012.

Krumpen, Thomas, S. Willmes, M. A. Morales Maqueda, C. Haas, J. Hölemann, R. Gerdes and D. Schröder

2011 'Evaluation of a polynya flux model by means of thermal infrared satellite estimates', *Annals of Glaciology*, 52, 57, pp. 52–60, DOI: 10.3189/172756411795931615.

Kwok, Ronald

2011 'Observational assessment of Arctic Ocean sea ice motion, export, and thickness in CMIP3 climate simulations', *Journal of Geophysical Research*, 116, CooD05, p. 8, DOI: 10.1029/2011JC007004.

Kwok, Ronald and G.F. Cunningham

2002 'Seasonal ice area and volume production of the Arctic Ocean: November 1996 through April 1997', *Journal of Geophysical Research*, 107, C10, p. 8038, DOI: 10.1029/2000JC000469.

Kwok, Ronald, John C. Curlander, Ross McConnell and Shirley S. Pang

1990 'An Ice-Motion Tracking System at the Alaska SAR Facility', *IEEE Journal of Oceanic Engineering*, 15, 1 [Jan. 1990], pp. 44–54, ISSN: 0364-9059, DOI: 10.1109/48.46835.

Kwok, Ronald, A. Schweiger, D. A. Rothrock, S. Pang and C. Kottmeier

1998 'Sea ice motion from satellite passive microwave imagery assessed with ERS SAR and buoy motions', *Journal of Geophysical Research*, 103, C4 [Apr. 1998], pp. 8191–8214, DOI: 10.1029/97JC03334.

Lavergne, T., S. Eastwood, Z. Teffah, H. Schyberg and L.?A. Breivik

2010 'Sea ice motion from low?resolution satellite sensors: An alternative method and its validation in the Arctic', *Journal of Geophysical Research*, 115, C10032, p. 14, DOI: 10.1029/2009JC005958.

Leese, John A., Charles S. Novak and Bruce B. Clark

1971 'An Automated Technique for Obtaining Cloud Motion from Geosynchronous Satellite Data Using Cross Correlation', *Journal of Applied Meteorology*, 10 [1Feb. 1971], pp. 118–132, DOI: 10.1175/1520-0450(1971)010<0118:AATFOC>2.0.CO;2.

Leppäranta, Matti

2011 *The Drift of Sea Ice*, ed. by Philippe Blondel, 2nd ed., Springer - Praxis books in Geophysical Sciences, Springer Berlin / Heidelberg, 347 pp., ISBN: 978-3-642-04683-4, DOI: 10.1007/978-3-642-04683-4.

Lewis, J. P.

1995 'Fast Normalized Cross-Correlation', in *Proceedings of Vision Interface 95*, Quebec City, Canada, pp. 120–123.

Lindsay, R. W., J. Zhang and D. A. Rothrock

2003 'Sea-Ice Deformation Rates from Satellite Measurements and in a Model', *Atmosphere–Ocean*, 41, 1 [Mar. 2003], pp. 35–47, DOI: 10.3137/ao.410103.

Liu, Antony K., Seelye Martin and Ronald Kwok

1997 'Tracking of Ice Edges and Ice Floes by Wavelet Analysis of SAR Images', *Journal of Atmospheric and Oceanic Technology*, 14, 5 [Oct. 1997], pp. 1187–1198, DOI: 10.1175/1520-0426(1997)014<1187:TOIEAI>2.0.CO;2.

Lucas, Bruce D. and Takeo Kanade

1981 'An Iterative Image Registration Technique with an Application to Stereo Vision', in *Proceedings of Imaging Understanding Workshop*, pp. 121–130.

Lucchese, L., G. Doretto and G. M. Cortelazzo

2002 'A frequency domain technique for range data registration', *IEEE Transactions on Pattern Analysis and Machine Intelligence*, 24, 11 [Nov. 2002], pp. 1468–1484, ISSN: 0162-8828, DOI: 10.1109/TPAMI.2002.1046160.

Lüpkes, C., V. M. Gryanik, B. Witha, M. Gryschka, S. Raasch and T. Gollnik

2008 'Modeling convection over arctic leads with LES and a non-eddy-resolving microscale model', *Journal of Geophysical Research*, 113, C09028 [Sept. 2008], p. 17, DOI: 10.1029/2007JC004099.

Manduchi, Roberto and Gian Antonio Mian

1993 'Accuracy Analysis for Correlation-Based Image Registration Algorithms', in *IEEE International Symposium on Circuits and Systems (ISCAS)*, IEEE, Chicago, IL, pp. 834–837, ISBN: 0-7803-1281-3, DOI: 10.1109/ISCAS.1993.393852.

Martinson, Douglas G. and Christian Wamser

1990 'Ice Drift and Momentum Exchange in Winter Antarctic Pack Ice', *Journal of Geophysical Research*, 95, C2, pp. 1741–1755, DOI: 10.1029/JC095iC02p01741.

McConnell, Ross, Ronald Kwok, John C. Curlander, W. Kober and Shirley S. Pang

1991 'Ψ-S Correlation and Dynamic Time Warping: Two Methods for Tracking Ice Floes in SAR Images', *IEEE Transactions on Geoscience and Remote Sensing*, 29 [6Nov. 1991], pp. 1004–1012, ISSN: 0196-2892, DOI: 10.1109/36.101377.

McLaren, A. J., H. T. Banks, C. F. Durman, J. M. Gregory, T. C. Johns, A. B. Keen, J. K. Ridley, M. J. Roberts, W. H. Lipscomb, W. M. Connolley and S . W. Laxon

2006 'Evaluation of the sea ice simulation in a new coupled atmosphere-ocean climate model (HadGEM1)', *Journal of Geophysical Research*, 111, C12014 [Dec. 2006], pp. 1–17, DOI: 10.1029/2005JC003033.

McPhee, M .G.

1980 'An analysis of pack ice in summer', in *Proceedings of ICSI/AIDJEX Symposium on Sea Ice Processes and Models*, ed. by R. S. Protchard, University of Washington, Seattle, pp. 62–75.

Nansen, Fridtjof

1902 *The Oceanography of the North Polar Basin. Scientific Results*, vol. 3, 9, Longman Green & Co., Kristinania, Norway.

Ninnis, R. M., W. J. Emery and M. J. Collins

1986 'Automated Extraction of Pack Ice Motion From Advanced Very High Resolution Radiometer Imagery', *Journal of Geophysical Research*, 91, C96, pp. 10725–10734, DOI: 10.1029/JC091iC09p10725.

Onstott, Robert G.

1992 'SAR and Scatterometer Signatures of Sea Ice', in Carsey [1992], chap. 5, pp. 74–104, ISBN: 0-87590-033-X.

Pease, Carol H.

1987 'The Size of Wind-Driven Coastal Polynyas', *Journal of Geophysical Research*, 92, C7, pp. 7049–7059, DOI: 10.1029/JC092iC07p07049.

Rodgers, Joseph Lee and W. Alan Nicewander

1988 'Thirteen Ways to Look at the Correlation Coefficient', *The American Statistician*, 42, 1 [Feb. 1988], pp. 59–66, DOI: 10.2307/2685263.

Rossby, C. G. and R. G. Montgomery

1935 'Frictional Influence in Wind and Ocean Currents', *Papers in Physical Oceanography and Meteorology*, 3, 3, Massachutsetts Institute of Technology and Woods Hole Oceanographic Institute, Cambridge, MA.

Schmitt, C., Ch. Kottmeier, S. Wassermann and M. Drinkwater

2004 *Atlas of Antarctic Sea Ice Drift*, Institut für Meteorologie und Klimaforschung, Universität Karlsruhe, http://imkbemu.physik.uni-karlsruhe.de/~eisatlas/.

Schreer, Oliver

2005 *Stereoanalyse und Bildsynthese*, Springer, 278 pp., ISBN: 978-3-540-23439-5.

Stern, Harry L. and Richard E. Moritz

2002 'Sea ice kinematics and surface properties from RADARSAT synthetic aperture radar during the SHEBA drift', *Journal of Geophysical Research*, 107, C10, p. 8028, DOI: 10.1029/2000JC000472.

Sun, Changming

2002 'Fast Stereo Matching Using Rectangular Subregioning and 3D Maximum-Surface Techniques', *International Journal of Computer Vision*, 47, 1–3, pp. 99–117, DOI: 10.1023/A:1014585622703.

Thomas, Mani V.

2004 *Global Motion Estimation of Sea Ice using Synthetic Aperature Radar Imagery*, MA thesis, University of Delaware.

2008 *Analysis of large Magnitude Discontinuous Non-Rigid Motion*, dissertation, University of Delaware, Delaware, USA, p. 294, http://proquest.umi.com/pqdweb?did=1654490401&sid=5&Fmt=2&clientId=8331&RQT=309&VName=PQD.

Thomas, Mani V., Cathleen A. Geiger and Chandra Kambhamettu

2004 'Discontinuous Non-Rigid Motion Analysis of Sea Ice using C-Band Synthetic Aperture Radar Satellite Imagery', in *IEEE Computer Society Conference on Computer Vision and Pattern Recognition Workshops*, vol. 1, ISBN: 0-7695-2158-4, DOI: 10.1109/CVPR.2004.51.

Thomas, Mani V., Shubhra Misra, Chandra Kambhamettu and James T. Kirby

2005 'A robust motion estimation algorithm for PIV', *Measurment Science and Technology*, 16 [Feb. 2005], pp. 865–877, DOI: 10.1088/0957-0233/16/3/031.

Thomas, Mani V., Cathleen A. Geiger and Chandra Kambhamettu

2008a 'High resolution (400 m) motion characterization of sea ice using ERS-1 SAR imagery', *Cold Regions Science and Technology*, 52 [2Apr. 2008], pp. 207–223, DOI: 10.1016/j.coldregions.2007.06.006.

Thomas, Mani V., Cathleen A. Geiger, P. Kannan and C. Kambhamettu

2008b 'Streamline Regularization for Large Discontinuous Motion of Sea Ice', in *2008 IAPR Workshop on Pattern Recognition in Remote Sensing (PRRS 2008)*, ed. by Selim Aksoy and Nicolas H. Younan, International Association for Pattern Recognition, Institute of Electrical and Electronics Engineers, Inc., Tampa, FL, pp. 1 –4, DOI: 10.1109/PRRS.2008.4783171.

Thomas, Mani V., Chandra Kambhamettu and Cathleen A. Geiger

2011 'Motion Tracking of Discontinuous Sea Ice', *IEEE Transactions on Geoscience and Remote Sensing*, 49 [12Dec. 2011], pp. 5064–5079, ISSN: 0196-2892, DOI: 10.1109/TGRS.2011.2158005.

Thorndike, A. S. and R. Colony

1982 'Sea Ice Motion in Response to Geostrophic Winds', *Journal of Geophysical Research*, 87, C8 [Feb. 1982], pp. 5845–5852, DOI: 10.1029/JC087iC08p05845.

Timmermann, R., A. Beckmann and H. H. Hellmer

2002 'Simulations of ice-ocean dynamics in the Weddell Sea - 1. Model configuration and validation', *Journal of Geophysical Research*, 107, C3, p. 3024, DOI: 10.1029/2000JC000741.

Vesecky, J. F., R. Samadani, M. P. Smith, J. M. Daida and R. N. Bracewell

1988 'Observation of sea-ice dynamics using synthetic aperture radar images: automated analysis', *IEEE Transactions on Geoscience and Remote Sensing*, 26 [1Jan. 1988], pp. 38–48, ISSN: 0196-2892, DOI: 10.1109/36.2998.

Wallach, Hans

1935 'Über visuell wahrgenommene Bewegungsrichtung', *Psychologische Forschung*, 20 [Dec. 1935], pp. 325–380, ISSN: 0033-3026, DOI: 10.1007/BF02409790.

A | PAPERS

A.1 PAPER I: ANNALS OF GLACIOLOGY

"Performance of a multiscale correlation algorithm for the estimation of sea-ice drift from SAR images: initial results"

Performance of a multiscale correlation algorithm for the estimation of sea-ice drift from SAR images: initial results

Thomas HOLLANDS, Wolfgang DIERKING

Alfred Wegener Institute for Polar and Marine Research, Bussestrasse 24, D-27570 Bremerhaven, Germany
E-mail: thomas.hollands@awi.de

ABSTRACT. Sea-ice drift fields were obtained from sequences of synthetic aperture radar (SAR) images using a method based on pattern recognition. The accuracy of the method was estimated for two image products of the Envisat Advanced SAR (ASAR) with 25 m and 150 m pixel size. For data from the winter season it was found that 99% of the south–north and west–east components of the determined displacement vector are within ±3–5 pixels of a manually derived reference dataset, independent of the image resolution. For an image pair with 25 m resolution acquired during summer, the corresponding value is 12 pixels. Using the same resolution cell dimensions for the displacement fields in both image types, the estimated displacement components differed by 150–300 m. The use of different texture parameters for predicting the performance of the algorithm dependent on ice conditions and image characteristics was studied. It was found that high entropy values indicate a good performance.

INTRODUCTION

Sea ice is subject to constant changes. Ice drift and deformation are influenced by forces from wind and ocean currents, by obstacles such as islands and coastlines and by ice thickness and roughness variations in a given area. Satellite-borne imaging sensors, operating in the optical and in the microwave range of the electromagnetic spectrum, are used for continuous monitoring of sea-ice-covered regions.

The main advantage of microwave data compared to optical imagery is that they are independent of weather and light conditions. For more detailed studies of sea-ice drift, synthetic aperture radar (SAR) images have been successfully used since the launch of European Remote-sensing Satellite ERS-1 (Holt and others, 1992). SAR imaging modes with different spatial coverage and resolution make it possible to investigate drift patterns at different scales. Our systematic analysis of different SAR image types indicates that the possibility to select between data acquired at different polarizations may enhance the reliability of the drift and deformation patterns derived from sequences of SAR images.

For the last three decades, various approaches have been applied to extract sea-ice drift information automatically from SAR data. One of the first approaches was described by Hall and Rothrock (1981). The first operational system was implemented at the Alaska SAR Facility by Kwok and others (1990). The range of approaches covers feature tracking, floe tracking, statistical methods and optical flow-based algorithms, as described by Gutierrez and Long (2003).

Some of the employed approaches are based on the tracking of pixel patterns such as that described by Fily and Rothrock (1987) while others first use a classification step to identify objects for tracking (Banfield, 1991; McConnell and others, 1991). Recent work by Thomas and others (2008) is based on pattern recognition to identify the change of positions of recognizable structures in the ice cover between successive SAR scenes. Hence, it depends on the assumption of temporal pattern stability.

However, sea-ice deformation changes existing patterns and violates the 'constancy constraint'. It is therefore necessary to acquire data with a sufficiently high temporal resolution which varies depending on the typical drift velocities in the area of interest. The temporal resolution also determines the accuracy of the displacement vector field derived from an image pair. The displacement vector represents the shortest distance between the respective positions of a reference point. The true path of the latter, however, may deviate considerably from a straight line between the two positions (e.g. due to the influence of varying wind directions and/or tidal currents). Any variations of the drift pattern between the two snapshots are unknown.

The first part of the paper deals with the description of the implemented method and the SAR data used for testing the algorithm. The implemented method is one of the most recent pattern-based tracking approaches and shows promising results for high-resolution sea-ice drift estimation from SAR satellite data (Thomas and others, 2008). To estimate the reliability of the method, it is crucial to quantify the magnitude of the error. Another central point of this paper is to establish criteria predicting the performance of the algorithm depending on ice-cover characteristics and image features such as the texture entropy.

In order to increase the spatial coverage, as well as to study details of drift and deformation in key regions, it is necessary to use data of different spatial resolution and swath widths and to quantify the differences in the estimated drift. Here comparisons between Image Mode (IM) and Wide Swath Mode (WS) products from Envisat Advanced SAR (ASAR) are presented. Finally, the results of this work are discussed and an outlook on future work is provided.

METHOD

The ice-drift algorithm used is based on a concept outlined by Thomas (2008) and Thomas and others (2008). In the original algorithm, global motion (inital motion vector) was estimated in advance either based on buoy data (Thomas, 2008) or based on an assumed phase correlation (Thomas and others, 2008). In our implementation, the initial motion vector is determined in the same way as subsequent vectors on finer scales (see the description of the algorithm below). Subpixel accuracy was not included in the recent version of our implementation. One reason for this was to minimize the

computational cost, which is an important aspect if sea-ice drift needs to be determined over a larger area and a longer time period.

Robustness against noise is an important criterion for the choice of a drift retrieval algorithm. To achieve a high robustness, the correlation module is embedded into a cascading resolution pyramid. It is based on a normalized cross correlation (NCC) with a preceding candidate selection. The candidates are selected by employing phase correlation, an approach which is described by, for example, Canty (2007). All correlation peaks higher than 75% of the maximum peak obtained from phase correlation are stored as candidates to be analysed employing the NCC. If the phase correlation does not provide an unambiguous result (>25% accepted correlation peaks), the region is regarded as distorted and an error flag is returned. The NCC has to be carried out in the spatial domain due to the nonlinear terms introduced by the normalization employing the standard deviation (division and squares), which cannot be carried out within a convolution kernel (Gonzalez and Woods, 2008). The application of two independent correlation measures increases the stability of the algorithm. Additionally, the algorithm runs in a computationally efficient manner since phase correlation can be performed efficiently in the Fourier domain.

The algorithm starts at the coarsest resolution level with a search window covering the full scene. On the second coarsest resolution level, the numbers of rows and columns of the scene double while the number of pixels in the search window stays the same which now covers a quarter of the full scene. For the calculation of position changes at the second level, the result of the first level is used as the initial shift and the resulting four shift vectors of the current resolution level are handed over as the initial shift to the next higher level. The next higher resolution level again contains four times more pixels, and the calculated shift vectors are used to initialize the calculations for the next step until the bottom of the resolution pyramid is reached.

The number of resolution levels and cascade runs are defined by the user. This procedure reduces the sensitivity to noise and increases the robustness of the algorithm, since the initial vectors are based on the resulting vectors of the previous cascade representing the estimated central shift for each search window. Due to this initial information, the algorithm searches in the predicted direction. Since the correlation module returns an error flag if a correlation 'fails', data gaps occur which would inhibit shift estimation on subsequent resolution levels. To avoid this and to reduce the influence of outliers on successive calculations, the data are regularized using a running box median filter followed by a triangulation-based interpolation to fill existing data gaps. The interpolation is performed using quintic polynomials (Akima, 1978).

In order to assess the quality of the results, the calculated values are compared with manually collected reference data. The reference vectors represent the shift of one specific identifiable object or pixel within the enclosing resolution cell, while the algorithm calculates a central shift for the whole cell. The comparison of both shifts is therefore, strictly speaking, only valid for uniform shifts within the respective resolution cell. The manually determined shift is also prone to errors. The appearance of distinct objects in the two images is sometimes slightly different, which makes it more difficult to determine the positions of matching reference points on a pixel scale. One way to estimate the magnitude of reference errors is the collection of two or more independent reference datasets.

When applying the drift retrieval algorithm described above, we assume that both images are precisely geocoded. The comparison between the results of pattern recognition and the manually derived dataset (which is a result of visual pattern recognition) is a quality control for the former since, in both approaches, only the two SAR images are compared. However, for estimating the absolute error of the obtained drift vectors, independent datasets such as drift buoy tracks and/or land-based control points are required. In this case, the geolocation errors of the SAR images and the reference drift patterns also have to be taken into account. For our SAR images we could not find suitable drift buoy data for comparision and the scenes did not cover land.

Methods based on pattern recognition calculate the spatial shift of a resolution cell from one point in time to another. Sea-ice drift refers to a velocity, i.e. a change of position within a certain time period. To compare the performance of the algorithm for different resolutions, the shift (motion) is presented as pixels. Calculated shift data can be converted to velocity by normalizing them to the time difference between the respective image acquisitions.

In practical situations, the retrieval of ice drift patterns is more difficult if the ice cover appears homogeneous in the image, without clearly recognizable structures. Hence, it is useful to check whether a given algorithm can be applied for given sea-ice conditions. For the algorithm used in this study, the correlation coefficients for each single resolution cell were compared to different texture parameters such as entropy and variance.

DATA

The Envisat ASAR data used for the analyses presented in this paper were acquired in 2006 in the Weddell Sea close to the grounded A-23A iceberg. The overlaps for each of the selected image pairs cover regions of at least 100 km $\times$ 100 km. The data are from the end of January, middle of June and end of August. For all three periods it was possible to order two IM SAR images. For the periods June and August, corresponding WS data could be ordered in addition to the IM data. Level 1b data products were used.

While the June and August datasets show numerous stable patterns, the patterns in the January scene change considerably due to the season (Antarctic summer). Prior to drift calculations, the images were geocoded and calibrated using commercial remote-sensing software. The drift in the IM data was determined using a five-level resolution pyramid within a six-stage cascade to create 512 $\times$ 512 resolution cells. The drift values from the WS data were obtained on the basis of a four-level image resolution pyramid within a five-stage cascade, creating 128 $\times$ 128 resolution cells. The amount of extractable cells depends on the extent and spatial resolution of the scene. Experiments show that the size of a resolution cell should not be smaller than $\sim$10 $\times$ 10 pixels in order to extract a stable shift vector field. These values are based on a close examination of the amount of data gaps and resulting resolution. A smaller resolution cell would grant a higher resolution of the drift field but would also contain more data gaps due to the smaller significance of corresponding image patterns.

The accuracy of the automated procedure was determined in comparison to manually derived reference datasets as

Table 1. Properties of test Envisat ASAR datasets. The original resolution refers to the image product, and the resampled resolution to the post-processed data products used for the drift calculation. The position of the overlap area is indicated by the coordinate of the upper left corner (UL). The drift algorithm calculates a drift for square regions (referred to as resolution cells). The covered area per resolution cell is called shift resolution. Dates are dd/mm/yy

	January	June	August	June WS	August WS
Acquisition dates	28/01/06, 29/01/06	17/06/06, 23/06/06	26/08/06, 27/08/06	16/06/06, 20/06/06, 22/06/06	25/08/06, 29/08/06
Mode	Image	Image	Image	Wide swath	Wide swath
Time difference (days)	1.19	5.80	1.19	4.05,* 6.01,† 1.96‡	4.12
Original resolution (m)	12.5 × 12.5	12.5 × 12.5	12.5 × 12.5	75 × 75	75 × 75
Used resolution (m)	25 × 25	25 × 25	25 × 25	150 × 150	150 × 150
Coordinate UL	76°14′24″ S, 43°12′24″ W	76°11′49″ S, 42°55′55″ W	75°55′40″ S, 43°48′58″ W	76°11′46″ S, 42°55′54″ W	75°55′39″ S, 43°49′02″ W
Dimensions (pixels)	5520 × 6263	6206 × 6163	6141 × 6089	1036 × 1029	1025 × 1016
No. of resolution cells	512 × 512	512 × 512	512 × 512	128 × 128	128 × 128
Shift resolution (m)	270 × 306	303 × 301	300 × 297	1214 × 1206	1201 × 1191
Collected reference shift vectors	135	Reference1: 150 Reference2: 150	151	143,* 159,† 163‡	162

*IM data pair 16–20/06/06. †IM data pair 16–22/06/06. ‡IM data pair 20–22/06/06.

described above. The number of collected vectors per image pair varies between 133 and 151. Details of the SAR scenes, the parameters required for the automated procedure and the reference datasets are summarized in Table 1.

RESULTS

The spatial resolution of the resulting drift vector fields is 300 m in the IM data and 1200 m in the WS data. Since we use geocoded images, the x and y axes (image coordinates) correspond to the south–north (SN) and west–east (WE) directions. Mean absolute velocities for the observed cases are 110–1850 m d^{-1}. Table 2 shows the mean absolute displacement per day in pixels and metres. The apparently inconsistent results for June can be explained by fast variations of wind direction and speed.

To generate larger datasets for statistical analysis of the errors, the differences between the algorithm and the reference are combined independently of direction where possible. It was therefore checked whether the error is direction-dependent using a two-sample Kolmogorov–Smirnov test. The null hypothesis H_0 states that the WE and SN errors come from the same distribution. The alternative hypothesis H_1 states that they come from different distributions. The IM error distributions for January and June do not depend on the direction at the 95% confidence level. For the August IM dataset, H_0 is rejected at the 95% confidence level. Based on the test results, errors in the WE and SN directions are combined for January and June but examined individually for the August period. Student's t-distribution is fitted to all four IM error distributions. All error values are within the 95% confidence bounds of the corresponding Student's t-distribution.

The calculated error statistics for the IM-based shift vector fields are listed in Table 3. For June and August, 99% of the calculated error values are within ±5 pixels, which corresponds to ±125 m in the IM images. With a time difference of 5.8 days (IM image pair from June), the error of the drift velocity is 22 m d^{-1}. With 1.19 days (IM image pair from August), it is 105 m d^{-1}. These values have to be related to the estimated daily mean absolute drift shown in Table 2.

For January (summer conditions), the error is ±12 pixels, corresponding to a displacement error of ±300 m. Error distributions for the August WS drift field and the 16–20 June WS data do not depend on the direction, while the error distributions for the 16–22 June WS and 20–22 June WS do. Since the position shift is estimated in numbers of pixels, the different error measures are also given as a number of pixels. As the errors for June and August are of almost identical magnitude in the SN and WE directions, it is reasonable to assume a lower bound of the spatial shift below which any displacement cannot be resolved reliably.

Thomas (2008) notes that a mean absolute percentage error (MAPE) of 10% is generally used as a reasonable metric in many practical applications. The goal is to give a limit for the estimated shift value below which the relative error has to be considered in subsequent applications. The absolute percentage error is calculated for each reference point individually. It is described as the absolute difference between reference shift and estimated value, divided by the absolute

Table 2. Mean absolute displacement of the sea ice for the observed time period, normalized to 1 day (24 hours). The results for June are discussed in the text

	Image pair						
	28–29/01/06	16–20/06/06	16–22/06/06	20–22/06/06	17–23/06/06	25–29/08/06	26–27/08/06
Resolution	IM	WS	WS	WS	IM	WS	IM
Daily mean absolute shift (pixels d^{-1})	74.17	2.75	0.72	4.21	13.28	7.24	7.06
Daily mean absolute drift (m d^{-1})	1854.25	412.50	108.00	631.50	332.00	1086.00	176.50

Table 3. Error statistics for IM data: dates of data acquisition, number of used reference displacement vectors *n*, the calculated mean error based on the used reference data (as well as the standard deviation of the error), the error margin representing 99% of the error, the mean absolute error (MAE) and the root mean square error (RMSE)

	Date			
	28–29/01/06	17–23/06/06	26–27/08/06	
			WE	SN
Antarctic season	Summer	Winter	Winter	Winter
Number of reference points, *n*	270	594	149	149
Mean error (pixels)	–0.08	0.13	–0.26	0.34
Standard deviation, σ (pixels)	1.46	1.20	0.93	0.89
$\text{Error}_{99\%}$ (pixels)	±11.57	±4.69	±4.48	±4.81
RMSE (pixels)	3.07	1.74	1.47	1.46
MAE (pixels)	1.84	1.19	0.98	0.98

reference shift. In order to estimate the minimum shift fulfilling this criterion, the mean absolute error (MAE) is used (Tables 3 and 4). The lower bound of the magnitude of the shift vector is therefore about ten times the MAE, meaning 8–12 pixels for June and August (200–300 m and 1200–1800 m, respectively) and about 18 pixels for January (450 m).

The relative error of a shift vector depends not only on the existence of constant patterns but also on the velocity of the related drift. In case of a slow drift, a short observation time might result in a positional shift not fulfilling the 10% criterion, while a longer observation time (with pattern constancy) might do. (The related lower bounds for the drift are calculated from the pixel shift bounds, converting them to a distance in metres based on the given resolution information. The limiting velocity is calculated by normalizing this distance to the time difference of the data pair.) The resulting lower bounds for the drift in the selected IM examples are 388 m d^{-1} (0.005 m s^{-1}) for January, 51 m d^{-1} (0.0006 m s^{-1}) for June and 206 m d^{-1} (0.002 m s^{-1}) for August. The resulting lower bounds for the WS examples are 210–690 m d^{-1} (0.002–0.008 m s^{-1}).

The comparison of two manually generated independent reference datasets of the sea-ice drift for June shows that the error between the reference shift and the central drift of the enclosing resolution cell, as well as of the error introduced by the manually collected reference data, is about ±1 pixel (25 m). This observation also makes sense given that there is no subpixel tracking for the reference data collection.

Figure 1 shows the results for the August data. The shape of the image boundaries is determined by the overlapping area between the two successive SAR images used for the derivation of the ice shift. In the figure, the estimated shift (left) is presented together with a gap map showing the positions of resolution cells where the matching algorithm returned an error flag (right). The corresponding pixels are marked by black dots. The overlap area covers the southern part of iceberg A-23A (upper left), surrounded by sea ice. In the western part, open water patches are visible with smaller icebergs. The key feature of the scene is a long lead dividing the ice cover into a western and an eastern part. While the sea ice in the western part of the scene is brought to a halt by iceberg A-23A in the north, it drifts comparatively fast northeastwards in the eastern part of the scene.

Studying the gap map reveals that the algorithm fails in some regions while it works perfectly well for others. Large icebergs can be easily detected by the increased number of correlation failures. This is also valid for leads and low-contrast regions such as in the southeast in Figure 1. Results for the January and June datasets also support this conclusion.

In order to identify other methods that help to assess the expected performance of the algorithm from the characteristics of the image, the correlation coefficient of each resolution cell was plotted against different texture parameters such as entropy and variance for the respective cell. Entropy is a measure used in information theory describing the uncertainty associated with a value. Minimum values occur for uniform regions while maximum values occur for heterogeneous regions with *n* equiprobable values for *n* texture pixels, as first described by Shannon (1948):

$$H(X) = -\sum_{i=1}^{n} p(x_i) \log_2 p(x_i), \quad (1)$$

where $p(x_i)$ is the probability mass function of outcome x_i.

Table 4. Same as Table 3, but for WS data

	Date					
	16–20/06/06	16–22/06/06		20–22/06/06		25–29/08/06
Direction		WE	SN	WE	SN	
Antarctic season	Winter	Winter	Winter	Winter	Winter	Winter
Number of reference points, *n*	286	159	159	163	163	324
Mean error (pixels)	–0.11	–0.01	0.29	–0.25	0.32	0.17
Standard deviation, σ (pixels)	1.00	1.56	1.20	0.95	1.04	0.82
$\text{Error}_{99\%}$ (pixels)	±3.65	±4.02	±3.09	±2.71	±3.07	±3.07
RMSE (pixels)	1.22	1.56	1.20	1.03	1.18	1.01
MAE (pixels)	0.91	1.07	0.84	0.82	0.90	0.75

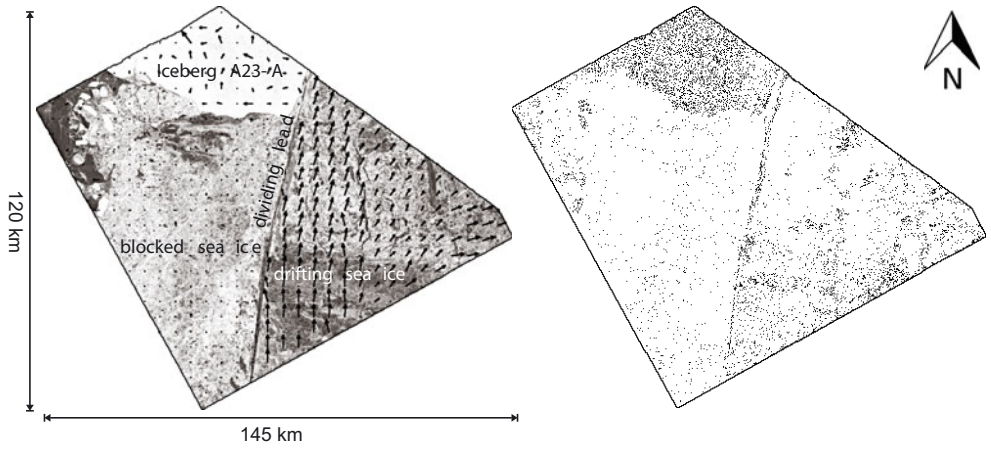

Fig. 1. Drift and data gaps of the August IM dataset. Left: data acquired on 26 August 2006 combined with the calculated drift between 26 and 27 August 2006; right: data gaps indicating regions (black dots) for which the algorithm failed to calculate reliable shift information and returned an error flag.

Equation (1) is employed as a measure of local textural heterogeneity. From the investigated parameters, a meaningful relationship was obtained only for the texture entropy (Fig. 2) but not for measures such as uniformity, registrability and intensity. Registrability is a measure developed by Chalermwat (1999) for high-performance image registration for remote sensing.

Two separated data clusters can be recognized in the two-dimensional (2-D) histogram (Fig. 2): a smaller group in the lower left corner with an entropy of 0.8–0.9 and a correlation coefficient of 0.1–0.3 and the main group with an entropy of 1.04–1.42 and a corresponding correlation coefficient of 0.35–0.85. The maximum observed entropy is 1.70. To reduce the variation in the data and to emphasize the correspondence between entropy and performance of the algorithm, the histogram is calculated based on preprocessed shift data which were filtered with a 5×5 median filter. The correlation coefficient for this relation is 0.75. While the smaller data cluster is only a significant feature for the August dataset, caused by the huge influence of A23-A on this scene, it is possible to find relations similar to the main group for January and June.

Higher entropy (local heterogeneity) indicates a higher probability of the occurrence of characteristic patterns in the sea-ice structure seen by the radar. In this case, the correlation coefficient between corresponding areas in successive images is higher. A low entropy value for a region indicates a lack of characteristic patterns, which may lead to worse correlation results. A lower entropy is linked with less local variation of the radar intensity. Compared with the sea-ice cover in the August scene, iceberg A23-A appears quite homogeneous. The correlation between entropy and (pattern) correlation coefficient is, however, only moderate. This indicates that the performance of the algorithm depends not only on the entropy but also on other image characteristics such as the presence of distinct patterns.

The result suggests that an entropy greater than 1.00 indicates good correlation conditions but with some restrictions due to the levelling nature of filtered values. Regions of high entropy cannot be correlated if patterns are different in the two images used for shift vector retrieval.

The third topic of this paper is the comparison of motion fields estimated from ASAR IM data with those from WS data. Figure 3 shows the corresponding results. The field of shift vectors calculated from the IM data is less homogeneous than that extracted from the WS mode where the flow field is more uniform. Key features of the drift field remain recognizable at the lower resolution level. To compare the results statistically, the IM shift vector field is smoothed and resampled to the resolution of the WS data. Both datasets are normalized to 1 day, assuming constant drift conditions during the observation period. Subsequently, the difference between the vector fields is calculated separately for the WE and SN components of the drift. The mean absolute distance between the WS shift and resampled IM shift is about 1 pixel (150 m) in the WE direction and 2 pixels (300 m) in the SN direction, with

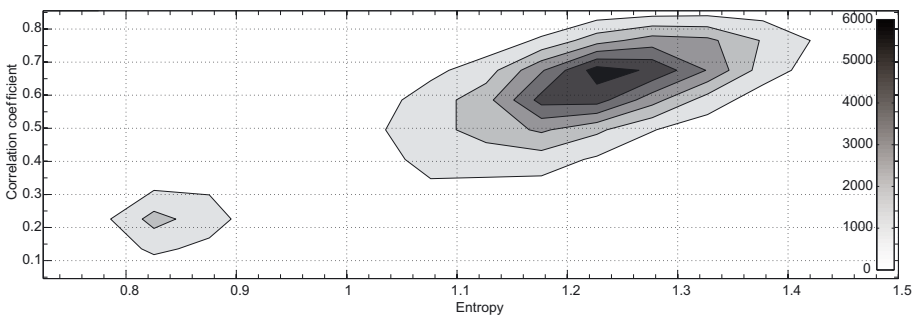

Fig. 2. Relation between entropy and correlation coefficient: a simplified 2-D histogram based on entropy values for each resolution cell and their corresponding median-filtered correlation coefficents. The data density is indicated with a greyscale.

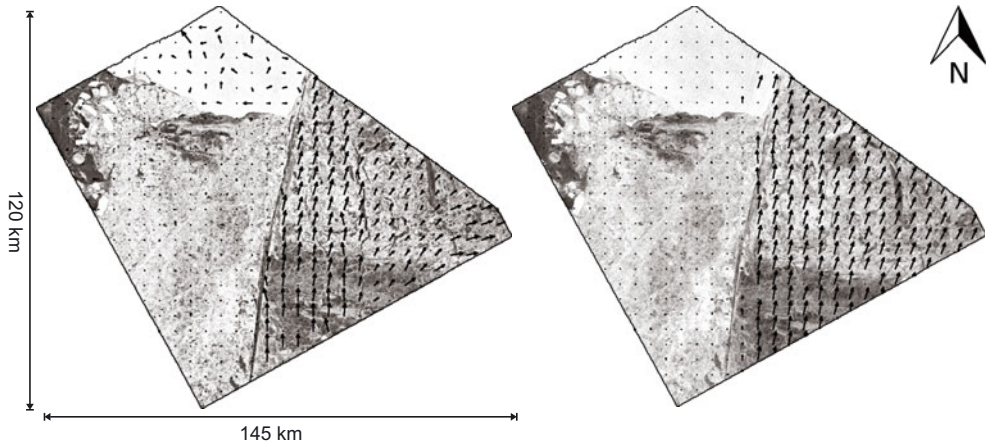

Fig. 3. August drift vector field and August WS drift vector field. Left: results for the IM data pair; right: WS results.

a corresponding RMSE of 2.64 pixels (400 m) in the WE direction and 3.73 pixels (560 m) in the SN direction.

Major differences in the drift field between the two datasets are caused by the different scales. The high-resolution vector field follows the shape of the central lead, while in the WS image larger shifts in the east are transferred into the stagnant sea ice in the west and vice versa. The relation between the IM-based drift field and the WS-based drift field is shown in the scatter plot in Figure 4, which illustrates the complex relation between the two motion fields. In contrast to the IM-based drift information, which identifies smaller motion variations even at the coarser resampled resolution, the WS-based motion field shows a more levelled drift. Both directions resolve the stable sea-ice situation south of iceberg A23-A.

The iceberg itself creates errors due to false correlation results related to its small amount of characteristic patterns. While the IM-based drift data follow the shape of the central lead quite closely, the WS-based motion shows various deviations from the orientation of the lead. East of the lead that divides the scene into two parts, the IM drift vector field shows drift zones of miscellaneous magnitude and direction while the WS data show a more homogeneous drift situation. The IM drift field reveals an eastern shift in the far east of the image, whereas the shift of the WS motion field is a northeastern shift in this region. Additionally, the fact that the image pairs span different time periods must be taken into consideration. Changing conditions during these periods would also lead to changes within the normalized data.

The situation is more complicated for the June period since the extracted drift fields do not show key features common to both imaging modes (IM and WS). The drift field extracted from both WS pairs, 16–20 June 2006 and 16–22 June 2006, fails to reveal drift characteristics similar to the drift field estimated from the IM pair. A direct comparison of shift is therefore not possible. The result of a manual check was that the calculated displacements are correct for all analysed cases. Based on the stable position of the grounded A23-A in all images, the observed change of motion cannot be explained by an erroneous geocoding. Instead it is more probable that a change of motion directions over time occurred, leading to different motion fields for each data pair because of different temporal gaps between the individual images. The change of motion over time is demonstrated on a single feature shown in Figure 5.

Wind data, provided by the Interim Re-analysis (Berrisford and others, 2009) of the European Centre for Medium-range Weather Forecasts, indicate heterogenic wind conditions with large variations in speed and direction for the period 16–23 June 2006. The wind directly affects the sea-ice drift characteristics. Since sea-ice motion is not only driven by the wind but depends also on ocean currents, tides and general sea-ice conditions (e.g. blocking effects by land and between different ice areas), it is difficult to link changes in sea-ice drift directly to changes in wind conditions. The wind data for the August observation period indicate the typical behaviour for the monitored region at this time of the year, with a dominating strong northward wind component.

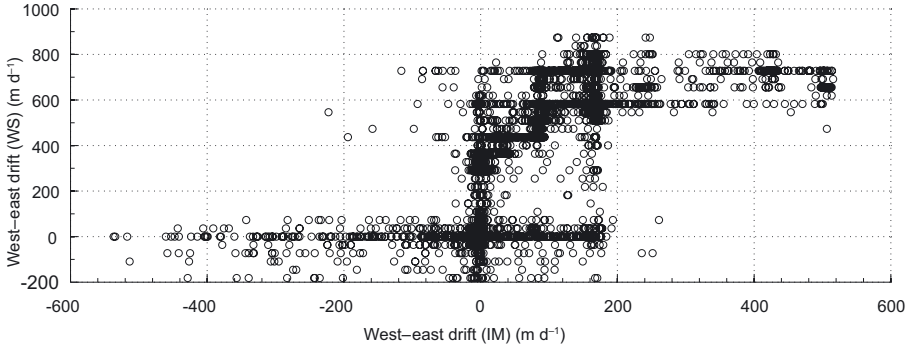

Fig. 4. Scatter plot of IM-based drift versus WS-based speed in WE direction. It shows that in IM images drift field variations are recognized over shorter distances, i.e. in greater detail, than in WS images.

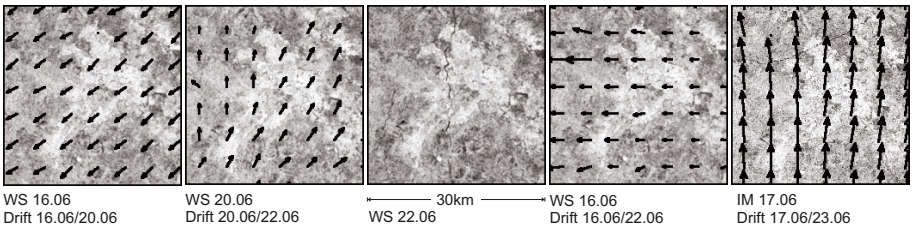

Fig. 5. Change of motion over time. Comparison of a characteristic pattern for all data pairs acquired in June 2006. The comparison indicates high variations of drift direction and magnitude. Dates are dd/mm.

CONCLUSION

The multiscale drift retrieval algorithm investigated in this study demonstrates a good performance for the analysed image pairs. A few drawbacks were found in cases for which central assumptions inherent in the algorithm were not valid. The quality of the estimated vector field strongly depends on pattern constancy in the analysed datasets, as the differences between the January dataset (summer) and the June and August datasets (winter) indicate.

In the analysed cases, the absolute error was independent of the magnitude of shift. The relative error therefore depends on the magnitude of shift. If a 10% criterion is used as an acceptable error for the shift, the minimum shift should be higher than 10–12 pixels (250–300 m) in winter (June and August) and about 18 pixels (450 m) in summer (January). Consequently, a longer time period between successive images is needed for slowly drifting ice than for large drift velocities. However, a longer time period increases the risk of violating the pattern constancy constraint.

The method has problems in homogeneous regions such as iceberg surfaces and areas without any features such as ridges and identifiable single floes. Fast-changing ice-cover characteristics such as leads revealed only low correlation coefficients between successive images. It was demonstrated that a relation between entropy and correlation performance exists and that a higher entropy is linked to a better correlation.

A first comparison of WS and IM data revealed that the drift fields estimated from the WS mode compare well with drift data estimated from IM data, although details are lost. In the presented example it was also demonstrated that sea-ice motion may change rather quickly. This is also very important for sea-ice physics since the averaging of heterogenous sea-ice motion fields may cause an underestimation of the ice velocity and the range of direction changes within the observation period, which affects our ability to interpret/reconstruct the observed sea-ice deformation patterns, in particular with regard to minor deformation events.

Our studies will continue with a comparison of motion fields derived from datasets with different spatial resolution, obtained with different imaging modes from different satellites. The goal is to increase the temporal and spatial resolution of the sea-ice motion field for detailed observation of sea-ice deformation.

ACKNOWLEDGEMENTS

The work of the first author is funded by the Alfred Wegener Institute in the framework of the German Earth Observing Network (Network EOS). We thank J. Hutchings, the scientific editor, and the reviewers for their useful and productive comments which greatly improved the paper.

REFERENCES

Akima, H. 1978. A method of bivariate interpolation and smooth surface fitting for irregularly distributed data points. *ACM Trans. Math. Softw.*, **4**(2), 148–159.

Banfield, J. 1991. Automated tracking of ice floes: a stochastic approach. *IEEE Trans. Geosci. Remote Sens.*, **29**(6), 905–911.

Berrisford, P. *and 6 others*. 2009. *The ERA-Interim archive*. Reading, European Centre for Medium-Range Weather Forecasts. (ERA Report Series 1.)

Canty, M.J. 2007. *Image analysis, classification and change detection in remote sensing: with algorithms for ENVI/IDL*. Boca Raton, FL, Taylor and Francis.

Chalermwat, P. 1999. High performance automatic image registration for remote sensing. (PhD thesis, George Mason University.)

Fily, M. and D.A. Rothrock. 1987. Sea ice tracking by nested correlations. *IEEE Trans. Geosci. Remote Sens.*, **25**(5), 570–580.

Gonzalez, R.C. and R.E. Woods. 2008. *Digital image processing. Third edition.* Upper Saddle River, NJ, Pearson Education.

Gutierrez, S. and D.G. Long. 2003. Optical flow and scale-space methods and applications in sea ice motion in Antarctica. *In* Stein, T., *ed. IGARSS 2003, International Geoscience and Remote Sensing Symposium, 21–25 July 1999, Toulouse, France. Proceedings, Vol. 4*. Piscataway, NJ, Institute of Electrical and Electronics Engineers, 2805–2807.

Hall, R.T. and D.A. Rothrock. 1981. Sea ice displacement from Seasat synthetic aperture radar. *J. Geophys. Res.*, **86**(C11), 11,078–11,082.

Holt, B., D.A. Rothrock and R. Kwok. 1992. Determination of sea ice motion from satellite images. *In* Carsey, F.D. *and 7 others, eds. Microwave remote sensing of sea ice*. Washington, DC, American Geophysical Union, 343–354.

Kwok, R., J.C. Curlander, R. McConnell and S.S. Pang. 1990. An ice-motion tracking system at the Alaska SAR facility. *IEEE J. Ocean. Eng.*, **15**(1), 44–54.

McConnell, R., R. Kwok, J.C. Curlander, W. Kober and S. Pang. 1991. Psi-S correlation and dynamic time warping: two methods for tracking ice floes in SAR images. *IEEE Trans. Geosci. Remote Sens.*, **29**(6), 1004–1012.

Shannon, C.E. 1948. A mathematical theory of communication. *Bell Syst. Tech. J.*, **27**(3), 379–423.

Thomas, M.V. 2008. Analysis of large magnitude discontinous non-ridge motion. (PhD thesis, University of Delaware.)

Thomas, M.V., C.A. Geiger and C. Kambhamettu. 2008. High resolution (400m) motion characterization of sea ice using ERS-1 SAR imagery. *Cold Reg. Sci. Technol.*, **52**(2), 207–223.

A.2 PAPER II: JOURNAL OF GEOPHYSICAL RESEARCH – OCEANS

"Sea ice motion at the Ronne Polynia, Antarctica: SAR observations vs. model results"

submitted for publication in Journal of Geophysical Research – Oceans

Sea ice motion at the Ronne Polynia, Antarctica: SAR observations vs. model results

T. Hollands,[1] V. Haid,[1] W. Dierking,[1] R. Timmermann[1] and L. Ebner[2]

Abstract. This study focuses on observations and simulations of the evolution of coastal polynias. We compare variations of polynia extent and ice drift patterns obtained from satellite radar images over the Ronne Polynia with results provided by the Finite Element Sea ice Ocean Model (FESOM), employing three atmospheric forcing data sets that differed in spatial and temporal resolution. Two polynia events are analysed, one from austral summer and one from late fall 2008. The open water zone in the polynia is of similar size in the satellite images and in the simulations results, but its temporal evolution differs slightly. We attribute this to the katabatic wind forcing used in the model. Modelled ice drift is slower than observed and reveals greater turning angles relative to the wind direction in many but not in all cases. For the summer event, model results obtained with high-resolution forcing are closer to the drift field derived from radar imagery than those from coarse-resolution forcing. For the late-fall event, none of the forcing data performs better relative to the others. Our results demonstrate that the coupled sea ice model can simulate polynia events realistically, provided that the modelling grid is dense (1-3 km) and the atmospheric forcing data are provided at high spatial resolution (<50 km).

1. Introduction

Polynias are often regarded as "sea ice factories". A deeper understanding of the physical processes related to polynia formation, changes of size, and closing is therefore of crucial importance [e. g. *Haarpainter et al.*, 2001; *Krumpen et al.*, 2011a]. Due to their special characteristics (continuously changing zones of open water and ice at different growth stages and highly variable ice drift patterns) polynias represent a challenge for remote sensing specialists as well as for modellers. The main objective of our study is to compare polynia observations using satellite images with results of a global coupled sea-ice ocean model.

Polynias are stable ice-free areas within the ice cover [*World Meteorological Organisation*, 1970]. They range in size between a few hundred metres to hundreds of kilometres. Their formation can be thermally driven due to temperature anomalies in the water column below or the air column above (sensible heat polynia). We deal here with latent heat polynias which are caused by mechanical effects when the ice is moved away from a fixed border (e. g. the coastline) by wind or currents [*Maqueda et al.*, 2004]. Since these processes are often related to topographical features of the region or special flow conditions depending on season or tides, polynias tend to occur recurrently at specific places, often at certain periods of the year. The formation of polynias has a significant impact on the regional climate. As gaps in the insulating sea ice cover, they allow for a strong heat exchange between ocean and atmosphere. This leads to an increased heat loss of the ocean and a warming of the air column above, which influences mesoscale atmospheric processes [*Lüpkes et al.*, 2008; *Fiedler et al.*, 2010]. Accordingly, polynias also affect biogeochemical air-sea fluxes as well as the tracer transport by the ocean [*Maqueda et al.*, 2004]. The export of ice away from the location of a latent heat polynia causes new ice formation, which is linked up with the rejection of brine. This mechanism causes an increased salinity in the upper water column, which affects the baroclinic circulation in the vicinity of the polynia. Combined with a weak stratification of the water column, this can trigger the formation of deep and bottom water.

In our analyses we consider the drift of thin ice in the polynia and of the pack ice adjacent to it since this information is essential in understanding the balance between polynia opening triggered by offshore katabatic winds and its closing by ice formation in the polynia area [e. g. *Van Woert*, 1999]. Since the early 1980s, satellite images have been used to estimate the motion of sea ice with passive microwave and infrared sensors [*Curlander et al.*, 1985; *Ninnis et al.*, 1986]. For detailed studies of local and regional sea ice dynamics, data from spaceborne synthetic aperture radar (SAR) systems are more suitable. On scales from a few tens of kilometres up to 500 km (the latter being the typical swath width of Wide Swath or ScanSAR mode), sea ice drift vectors can be provided independent of light and cloud conditions. Depending on the input data, the spatial resolutions of such vector maps are tens of kilometres to a few hundred meters [e. g. *Thomas et al.*, 2009; *Hollands and Dierking*, 2011]. With high-frequency radar such as TerraSAR-X even higher resolutions are possible.

We use imagery of satellite-borne SAR at spatial resolutions of 150 metres to study the variations of the polynia extent. Size variations of coastal polynias have been determined from data of satellite-borne microwave radiometers [e. g. *Kern*, 2009] and sensors measuring thermal infrared radiation [e. g. *Ciappa et al.*, 2012; *Wendler et al.*, 1997] and a combination of both [e. g. *Willmes et al.*, 2010]. The former operate at spatial resolutions of tens of kilometres, whereas the latter provide data at resolutions on the order of one kilometre. The polynia extent determined from passive microwave data covers both open water and thin ice areas, whereas it is easier to distinguish open water and ice in the optical and infrared images.

To explain temporal fluctuations in the extent of coastal polynias, several simple models have been developed and applied [e. g. *Pease*, 1987; *Van Woert*, 1999; *Krumpen et al.*,

[1]Alfred Wegener Institute for Polar and Marine Research, Bremerhaven, Germany.

[2]Department of Environmental Meteorology, Faculty of Geosciences, University of Trier, Trier, Germany.

0148-0227/13/$9.00

2011b]. These models are based on the balance between ice edge advection induced by katabatic winds and ice production within the polynia. Even if they are driven by local atmospheric flux data they neglect the interaction with other factors such as the spatial water-land distribution and the specific ice conditions (concentration, thickness, degree of deformation, extent) that may influence the evolution of the polynia. In our study, we use the Finite Element Sea Ice Ocean Model (FESOM), which is a coupled sea ice-ocean model described by *Timmermann et al.* [2009], in a configuration that provides results at spatial resolutions of up to 3 kilometres for our region of interest. At such resolutions the scales of satellite radar observations and model simulations become comparable, which allows a more detailed insight into small-scale processes related to polynia dynamics. Model simulations of temporal polynia evolution as a function of environmental conditions are sensitive to the atmospheric forcing data [e. g. *Mathiot et al.*, 2012]. In our study, we use three atmospheric forcing data sets that differ in their spatial and temporal resolution.

Our focus is on the Ronne Polynia, a coastal polynia in the Weddell Sea east of the Antarctic Peninsula and west of Berkner Island. It is mainly driven by strong wind outbursts from the Ronne Ice Shelf [*Gill*, 1973; *Renfrew et al.*, 2002]. The area of the polynia usually decreases towards spring and summer, as the offshore component of the wind weakens [*Maqueda et al.*, 2004]. We introduce the FESOM model and the available atmospheric forcing data in section 2. In the third section we describe the acquired SAR data and the methodology to determine polynia size and ice motion from satellite imagery. Subsequently we assess the quality of the ice tracking algorithm and outline the method of comparison between drift patterns obtained from the satellite images and the simulated data. In the fourth section we examine modelled and observed polynia sizes and compare the corresponding ice motion data. Here, several model runs with different atmospheric forcing data are used. To identify differences in the ice motion between the thin ice in the polynia and the adjoining pack ice we analyse both regions separately. The discussion (section 5) addresses various influences on ice motion, the ratio between ice drift and wind speed, and possible strategies to improve the comparison between drift patterns derived from satellite data and obtained from modelling results. Finally, the conclusions are presented.

2. The Finite Element Sea ice-Ocean Model (FESOM)

FESOM is a finite-element ocean circulation model including a dynamic-thermodynamic sea-ice component. It was developed at Alfred Wegener Institute and is described by *Timmermann et al.* [2009]. The sea ice model component uses the *Parkinson and Washington* [1979] thermodynamics. It includes a snow layer, the presence of which affects sea ice growth and melting considerably [*Owens and Lemke*, 1997]. The model is capable of forming snow ice due to flooding [*Leppäranta*, 1983; *Fischer*, 1995]. Linear temperature profiles are assumed in both layers applying the zero-layer approach of *Semtner Jr.* [1976], which neglects heat storage within the ice or snow. Prognostic variables are the mean ice thickness (ice volume per unit area) h_i, mean snow thickness (snow volume per unit area) h_s, ice concentration A, and ice drift velocity $\vec{u}_i$. Ice concentration is calculated following the suggestions by *Hibler III* [1979]. Snow and sea ice thickness are both assumed to be evenly distributed over the ice-covered part of each area unit. They can change by melting and freezing processes and are advected with the sea ice drift. The ice drift is influenced by atmospheric and oceanic surface stresses, sea surface slope and internal ice strength following the momentum balance equation

$$m\left(\frac{\partial \vec{u}_i}{\partial t} + f(\vec{k}\times\vec{u}_i)\right) = A(\vec{\tau}_{ai} - \vec{\tau}_{io}) + \vec{F} - mg\,\nabla\eta$$

with the mass of ice plus snow per unit area m, the Coriolis parameter f, the unit vector orthogonal to the surface $\vec{k} = (0, 0, 1)$, the wind stress $\vec{\tau}_{ai}$, the ice/ocean stress $\vec{\tau}_{io}$, the gravitational acceleration g and sea surface elevation η. The term $\vec{F} = \nabla \cdot \sigma$ accounts for the effect of internal stresses. The internal stress tensor σ is composed according to the elastic-viscous-plastic rheology as described by *Hunke and Dukowicz* [1997] and *Hunke and Lipscomb* [2001]. Atmospheric and oceanic stress are quadratic functions of the wind and water velocity relative to the ice. They are scaled with the ice concentration, following a suggestion by *Connolley et al.* [2004]

The second model component is a hydrostatic ocean circulation model that solves the primitive equations in a spherical geometry. For the parametrisation of subgrid-scale processes the model makes use of the rotated Redi and Gent-McWilliams diffusivities [*Redi*, 1982; *Gent and McWilliams*, 1990] and a vertical mixing scheme depending on the Richardson number [*Pacanowski and Philander*, 1981]. The dedicated equation of state as proposed by *Jackett and McDougall* [1995] facilitates the calculation of in-situ density as a function of potential temperature. Temperature, salinity, horizontal velocities and surface elevation are represented by continuous, linear basis functions.

Sea ice and ocean model component use the same surface grid. This enables easy communication between the two model components since no interpolation of results from either side is necessary. A flux-averaging method is applied to consider fluxes both in open water and in the ice-covered part of each area element [*Timmermann et al.*, 2009]. Fluxes of heat, salt, and momentum (the latter represented by the ice-ocean surface stress) are transferred between sea ice and ocean model components after each time step.

For this study the model was run on a global, unstructured grid with a horizontal resolution that ranges from 2.5° in the open oceans to 3 km at the western Weddell Sea coastline. In the vertical direction 37 z-levels were set up with resolution increasing toward the surface (6 levels in the uppermost 100 m). To enable a smooth and realistic representation of the bathymetry, the bottom nodes are allowed to deviate from the depth levels in a manner similar to the shaved-cells approach in finite-difference models [*Wang*, 2007]. A preliminary version of the topographic dataset RTopo-1 [*Timmermann et al.*, 2010] that in the Ronne region largely replicates ALBMAP [*Le Brocq et al.*, 2010] was used to create the model bathymetry. The time step was set to 3 minutes since the high spatial resolution of the model requires a corresponding high temporal resolution. Averaged output data was provided every 24 h (originally for another project). For our study this is sufficient because the ice drift magnitudes determined from SAR images are in most cases averages over 24 hours as well.

The model was initialized on January 1, 1980 with data from Polar Science Center Hydrographic Climatology (PHC) [*Steele et al.*, 2001] and run for a period of 30 years. Although the development of the PHC data set was developed for the Arctic Ocean, its performance is also good in the Southern Ocean.The atmospheric forcing was supplied by data from NCEP/NCAR Reanalysis by the National Centres of Environmental Prediction [*Kalnay et al.*, 1996]. This is a global dataset with a horizontal resolution of 1.875°. For our simulations, we used the daily datasets of 10-m wind velocity, 2-m air temperature, 2-m specific humidity, sea level air pressure, precipitation rate, relative cloud cover and latent heat flux. From these quantities,

evaporation, downward longwave radiation and downward short wave radiation are calculated.

A second model run employing data from the Global Model Europe (GME) [*Majewski et al.*, 2002] for the period April 2007 – December 2008 was performed. The required forcing fields are provided at time steps of 6-hours and at a spatial resolution of 60 km. In a third experiment we replaced the GME data in the southwestern Weddell Sea region by data from a regional setup of the COSMO model that is operated at the University of Trier. COSMO (= Model by Consortium for Small-Scale Modelling) [*Baldauf et al.*, 2011] provides forcing data with a temporal resolution of one hour, covering the area of the Antarctic Peninsula and the coast of the southwestern Weddell Sea with 5 km resolution. The data were fed into FESOM for an L-shaped area covering the coastline of the western Weddell Sea (from 65°W to 44.5°W and south of 62.55°S, and from 44.5°W to 15.05°W and south of 69.5°S) for the period March 2008 – August 2008. Hence, our test site (as e. g. shown in Fig. 6) is completely covered.

Both GME and COSMO are models developed by the German Meteorological Service (Deutscher Wetterdienst, DWD). The GME forcing data are the result of an analysis with consideration of atmospheric observations and sea ice data from SSM/I observations. COSMO is a regional forecast model with a thermodynamic ice model [*Schröder et al.*, 2011] receiving its lateral boundary conditions from GME. In general, the choice of the forcing data for the model simulations depends on the specific goals of investigation. NCEP is a long-term consistent data set with a low spatial resolution. If higher resolution is needed, GME forcing data are better in many aspects but provide a shorter temporal consistency. Forcing data at high spatial and temporal resolution are provided by COSMO, but only for a short period of time.

3. Data Processing

3.1. Polynia size

For the retrieval of polynia extent and ice drift patterns we used data from the Advanced Synthetic Aperture Radar (ASAR) on-board the European Environmental Satellite (Envisat). The data were acquired in 2008. The ASAR images were calibrated and geo-referenced with a pixel size of 150 m. The different characteristics of sea ice in the polynia and of the adjacent pack ice are in many cases clearly reflected in their appearance in the radar images. Since our SAR images did not always cover the entire extent of the Ronne Polynia, we determined its instantaneous area from the SAR observations and from the model simulations within the overlap region common to all SAR images. For the determination of polynia size, we marked the polynia manually by a region of interest (ROI) and calculated its area. In Fig. 1 a SAR image of the Ronne Polynia is shown. The bright area in the lower left of the image is the Ronne

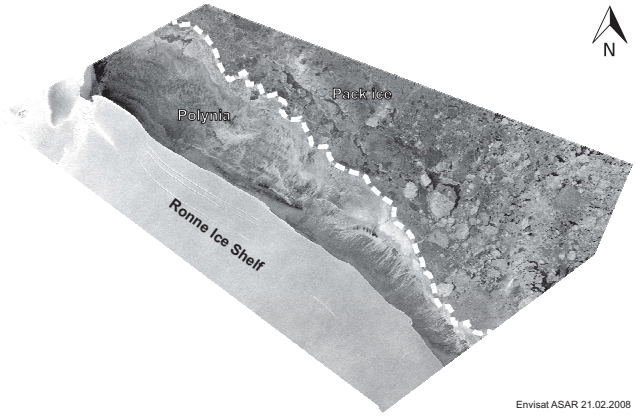

Figure 1. Ronne Polynia. The ASAR image was acquired on 21. February 2008. Three surface types (ice shelf, polynia, pack ice) have been marked. The right side shows the simulated polynia extent of the Ronne Polynia, based on ice concentrations of 30%,50% and 70% for the same day.

Table 1. Envisat Wide Swath scenes used for the region of the Ronne polynia[a]

ID	Image 1		Image 2		Wind	
	Date	Time	Date	Time	Speed	Direction
50	02/18	6:09:53	02/19	5:38:44	5.8 m/s	-11.3°
51	02/19	5:38:44	02/20	10:04:30	7.7 m/s	-33.4°
52	02/20	5:07:33	02/21	9:33:21	4.7 m/s	-46.2°
53	02/21	9:33:21	02/22	5:44:25	2.1 m/s	-50.6°
54	02/22	5:44:25	02/23	5:13:15	1.6 m/s	140.2°
55	02/23	5:13:15	02/23	10:10:10	3.2 m/s	98.7°
152	05/30	6:04:14	05/31	5:33:05	11.5 m/s	-34°
153	05/31	5:33:05	06/01	5:01:43	9.7 m/s	-32.7°
154	06/01	5:01:43	06/02	5:07:28	5.3 m/s	-26.5°
157	06/04	5:07:28	06/05	9:33:22	9.0 m/s	-26.1°
158	06/05	9:33:22	06/06	5:44:26	10.3 m/s	-31.6°
159	06/06	5:44:26	06/07	5:50:06	9.4 m/s	-30.8°
162	06/09	5:50:06	06/10	10:15:51	5.0 m/s	-21.7°
163	06/10	10:15:51	06/11	9:44:42	4.4 m/s	-9.2°

[a] Listed are acquisition date and time. The wind data was derived from the NCEP/NCAR Reanalysis data. The wind direction to which the wind is blowing is given counter-clockwise relative to North. The ID is related to the day of the year at which the second scene was acquired. To ease the comparison between SAR observations and modelling, the ID refers to 24 hours intervals starting at 5:30 am each day.

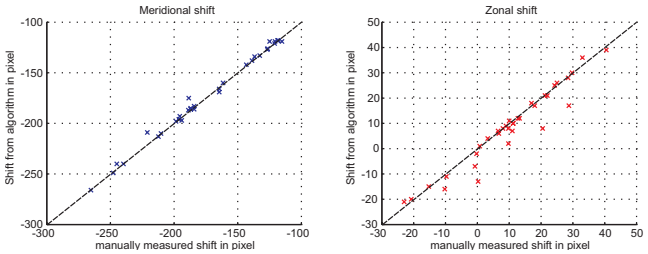

Figure 2. Scatter plot of data extracted by the algorithm versus reference data for drift pair 152 (30.05 - 31.05.2008).

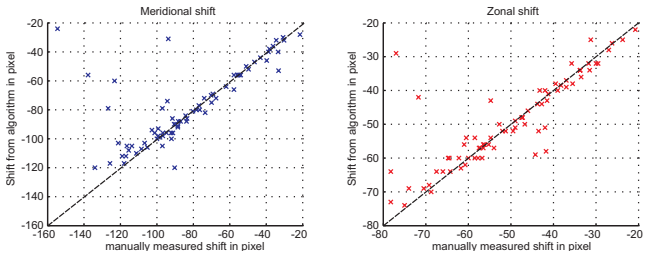

Figure 3. Scatter plot of data extracted by the algorithm vs. reference data for image pair 50 (18.02.2008 - 19.02.2008).

Ice Shelf, the upper part is pack ice in which single sea ice floes are recognizable. In the polynia, two zones can be separated: Adjacent to the ice shelf, the area is mainly ice free, whereas the area between open water and pack ice is covered by partly rafted or ridged thin ice. Towards the zone covered by thin ice, long feathery streaks are visible in the ice-free area, formed by wind-herding of the newly formed frazil ice.

In the model simulations, the polynia size is defined as the area with ice concentrations below 70%. This definition arises from the use of passive microwave data for polynia observations [e. g. *Massom et al.*, 1998]. We also estimated the polynia size using different concentrations (30% and 50%), and additionally tested the inclusion of modelled ice thickness i. e. all pixels with the given concentration limit or a thickness <0.2 m were classified as polynia. Since sea ice concentration and in particular ice thickness are difficult to determine in SAR images, we delimited the polynja from the adjacent pack ice and ice shelf by considering the image intensity and texture. We distinguished two different areas by their visual appearance: (1) the area of open water including the transition zone characterized by strips of frazil or grease ice as indicator of polynia size in agreement with studies using thermal infrared data [e. g. *Ciappa et al.*, 2012], and (2) the area between the ice shelf and the pack ice boundary. The zone of open water and newly formed ice is sometimes hardly to separate and hence prone to larger errors (between approximately 10-30 percent). The boundary between the recently formed "polynia ice" and the pack ice is often visible for several days, and the error in the area calculation is smaller than 10 percent.

3.2. Sea ice motion and its validation

The selected time periods for the ASAR image analysis were chosen based on simulations with FESOM to ensure high polynia activities, also considering the availability in the Envisat ASAR data storage archive. For 2008 five periods were identified during which SAR image pairs with smaller temporal gaps (between less than 5 hours and one day) were acquired. For our study we selected two periods, one in February (austral summer), one in May/June (late fall). The scenes for both periods are listed in Table 1. The covered area is about 27000 km^2 and includes the Ronne Ice Shelf margin, the polynia and the adjacent sea ice.

All drift vectors are calculated with a multi-scale tracking algorithm introduced by *Thomas et al.* [2008, 2011] and modified by *Hollands and Dierking* [2011]. The algorithm searches for corresponding radar intensity patterns in a pair of SAR images and calculates the spatial displacement between the respective locations of these patterns. For computational efficiency this procedure is initialized at a level of coarse spatial resolution (the original SAR images are low-pass filtered), which is successively increased to a final pixel size of 150 m at the level of highest resolution. At this level the displacement vectors are determined on a grid of 128×128 resolution cells for June (256×256 cells for February), each comprising 14×19 (7×11) pixels. The resulting vector field is re-sampled to an equally spaced grid with a cell size of 2500×2500 m. Since the shape of ice structures in the thin ice area of the polynia (such as cracks, rafting zone, different belts of ice) sometimes changes within very short time intervals, it can be difficult to retrieve displacements with the same robustness and spatial density as in the adjacent thicker sea ice. Missing displacement vectors are substituted by averages of their neighbours, which means that the vector field of the thicker ice influences the results inside the polynia to a certain degree.

The tracking algorithm provides the correlation coefficients as output for an assessment of the robustness of the retrieved ice motion field. Nevertheless, in rare cases the algorithm links two different ice structures instead of finding the same structure in a given pair of satellite images. Therefore, we estimate the quality of the retrieved displacements using a validation procedure similar to the one described in [*Hollands and Dierking*, 2011] which is based on manually collected displacement vectors as reference. We found only two cases in which the drift velocity of the pack ice zone obtained from the tracking procedure was too large (image pairs 53 and 162). These were excluded from further analyses. The reason for the erroneous retrieval results were a very low radar intensity contrast between ice structures and the undisturbed ice surface, as well as the fact that the pack ice zone in the overlap of the two satellite images was relatively small. To demonstrate the quality of motion retrievals that can be achieved under normal circumstances, we carried out an extended quality assessment for two image pairs. Figure 2 shows scatter-plots for the meridional and zonal displacement component for image pair 152 (30.05 - 31.05.2008) taken from the late-fall period. The displacement of some ice structures was as large as 250 pixels, i. e. corresponding to 37.5 km in 24 hours. The automatically and manually determined values compare well with a correlation coefficient of 0.97 and 0.99 of the east-west and north-south displacement components, respectively. The corresponding values for the errors of the resulting ice drift components are -0.0007 ± 0.0015 m/s at an average velocity of 0.08 m/s (east-west) and 0.0001 ± 0.0013 at 0.34 m/s (north-south).

A general problem of radar images acquired under summer conditions (our February data) is that ice structures are often buried under wet snow, which means that they can hardly or not at all be detected by C-band radar [*Hollands and Dierking*, 2011]. Figure 3 shows a scatter plot of the output of the algorithm versus reference data for image pair 50 (18.02.2008 - 19.02.2008), based on 76 collected reference vectors. Here, correlation coefficients of 0.95 and 0.82 were obtained for the east-west and north-south displacement components, respectively. Errors of the ice drift components are -0.0012 ± 0.003 m/s at an average velocity of 0.11 m/s (east-west) and 0.003 ± 0.005 at -0.024 m/s (north-south). Larger deviations are caused by two different factors: (1) the ice concentration is lower and the ice thickness smaller in summer. Positions of deformation patterns (e. g. cracks, zones of rafting) or recognizable ice floes may change fast, and matching patterns are difficult to detect. (2) The ice motion is highly variable within small distances. Due to the smoothing procedure inherent in the algorithm, most outliers in the displacement field are suppressed. In Figure 2, the largest deviations occur when automatically determined displacements are smaller than the corresponding reference values. This supports the hypothesis that the algorithm suppresses displacement vectors introduced by single faster moving ice floes in favour of a consistent drift vector field.

3.3. Comparison of results from images and model

Ice motion vectors from the FESOM model simulations were given as vector components at every model grid point. From the analysis of satellite image pairs, displacement vectors were obtained. The latter were normalized by the time interval between the first and the second image to represent the observed average velocity. The model output was fixed to provide drift velocities for every day as averages over the last 24 hours. The reference time of the model output was set to 5:30 given that most satellite images were acquired around 5:00-6:00 in the morning. Since the simulated velocity field was provided on the unstructured grid used in FESOM, it was re-sampled to the grid used for the observed data.

Simulated and observed velocity fields were checked for systematic differences in direction and magnitude. For comparison we used histograms and polar plots. The latter

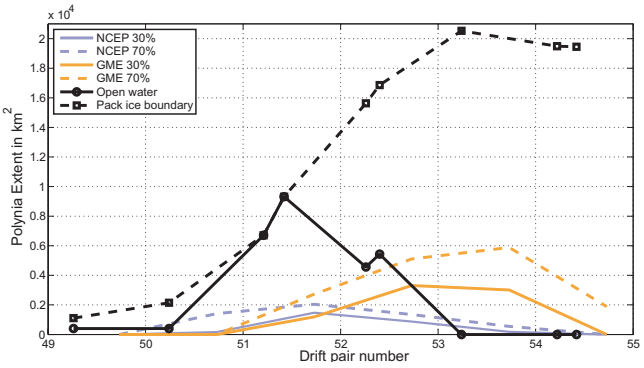

Figure 4. Observation and modelling of polynia-size for February.

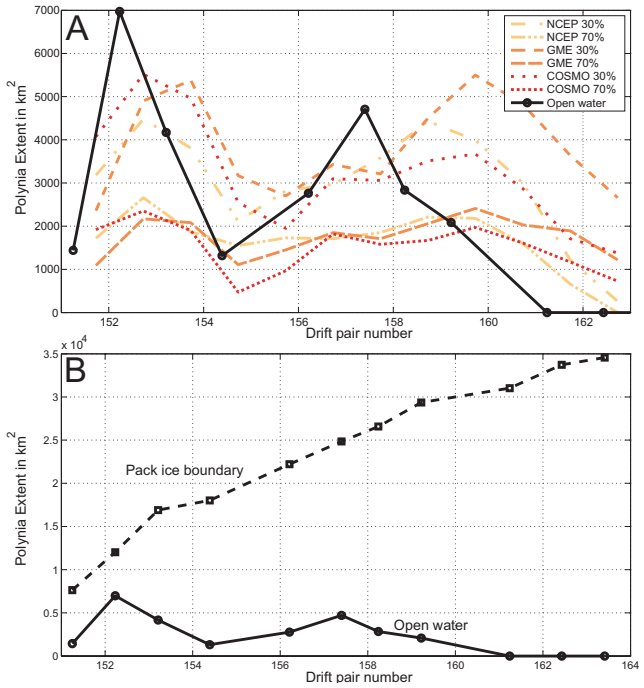

Figure 5. Observation and modelling of polynia-size for June. Panel A shows the model results and the observed open water area while panel B shows the growth of the thin ice area between the open water and the pack ice.

present the direction as angle and the magnitude as radius. The boxes shown in the plots contain the middle 68.3% of the data, i. e. within one the standard deviation of a normal distribution. The direction of a drift vector is given as angle ranging from 0° to 360°, counted positive in counterclockwise direction from north. The directional measures were calculated with a Toolbox for Circular Statistic described by *Berens* [2009].

3.4. Ice shelf edge

The position of the ice shelf margin as incorporated in the model is partly located further south compared to its position in the ASAR images. The offset varies between 0 and at maximum 20 km. The shelf ice margin of the model is based on ALBMAP version 1 which was published by *Le Brocq et al.* [2010]. For the Ronne Ice Shelf, they refer to *Lythe et al.* [2001]. The coastline of the Antarctic Peninsula in the model grid coincides exactly with the ASAR images. In all ASAR images, the margin of the Ronne Ice Shelf is located at the same position. We do not regard this offset as critical for our ice drift analysis. The reason is that the area closest to the ice shelf margin is open water in many cases, which is not considered in the comparison of drift vectors. When comparing the modelled and observed polynia size we assume that in case of strong katabatic winds the seaward wind field variations and the ice conditions relative to the ice shelf edge are the dominant factors influencing the growth of the polynia. This means that the offset of the ice shelf margin in the model has no effect on the evaluated polynia size.

4. Results

4.1. Polynia size

Figures 4 and 5 show the areas of the polynias observed in February and May/June in comparison to the simulated sizes. The results of model simulations are average values over 24 hours referring to a period from 5:30 am of one day to 5:30 am on the next day. In the figure, corresponding data marks are placed at 17:30 each day. The simulated areas were obtained by using ice concentrations of 30% and 70% and different forcings. The areas derived from the SAR images (open water and total area between pack ice and ice shelf (see section 3.1) refer to date and time of the image acquisition. The analysis of the SAR images reveals that in February the polynia grew rapidly on days 50 and 51. A belt of consolidated thin ice formed on day 52 at the seaward edge, and the size of the open water zone decreased. The partition of the polynia in two zones of water and ice, respectively, remained visible also on day 53. Starting with the end of day 53, almost the entire polynia area was covered by ice in the following days. While the margin of the pack ice, which moved further away from the ice shelf, could clearly be recognized in the beginning of this period, the transition from "polynia ice" to the pack ice was more difficult to detect later (on day 54), since structures more typical for pack ice (such as single ice floes) started to form in the "polynia ice". In comparison to the results from the SAR images, the initial increase in polynia size occurs later in the model simulations. Using the GME forcing, the delay is about one day, but the estimated area agrees much better

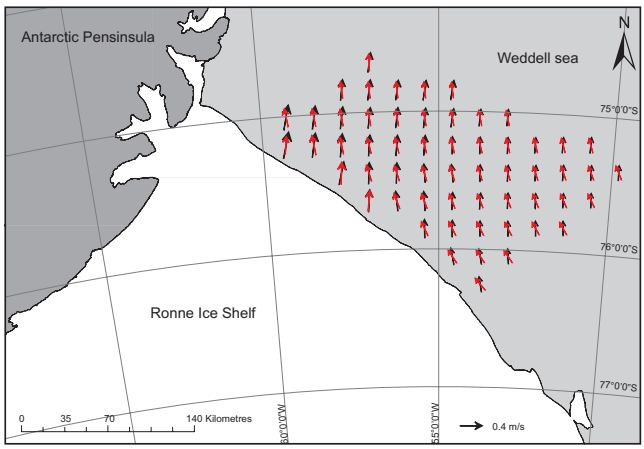

Figure 6. Drift vector field for observed drift (black) and modelled drift forced with NCEP (red) for day 152. The longest observed vector represents a drift magnitude of 0.58 m/s.

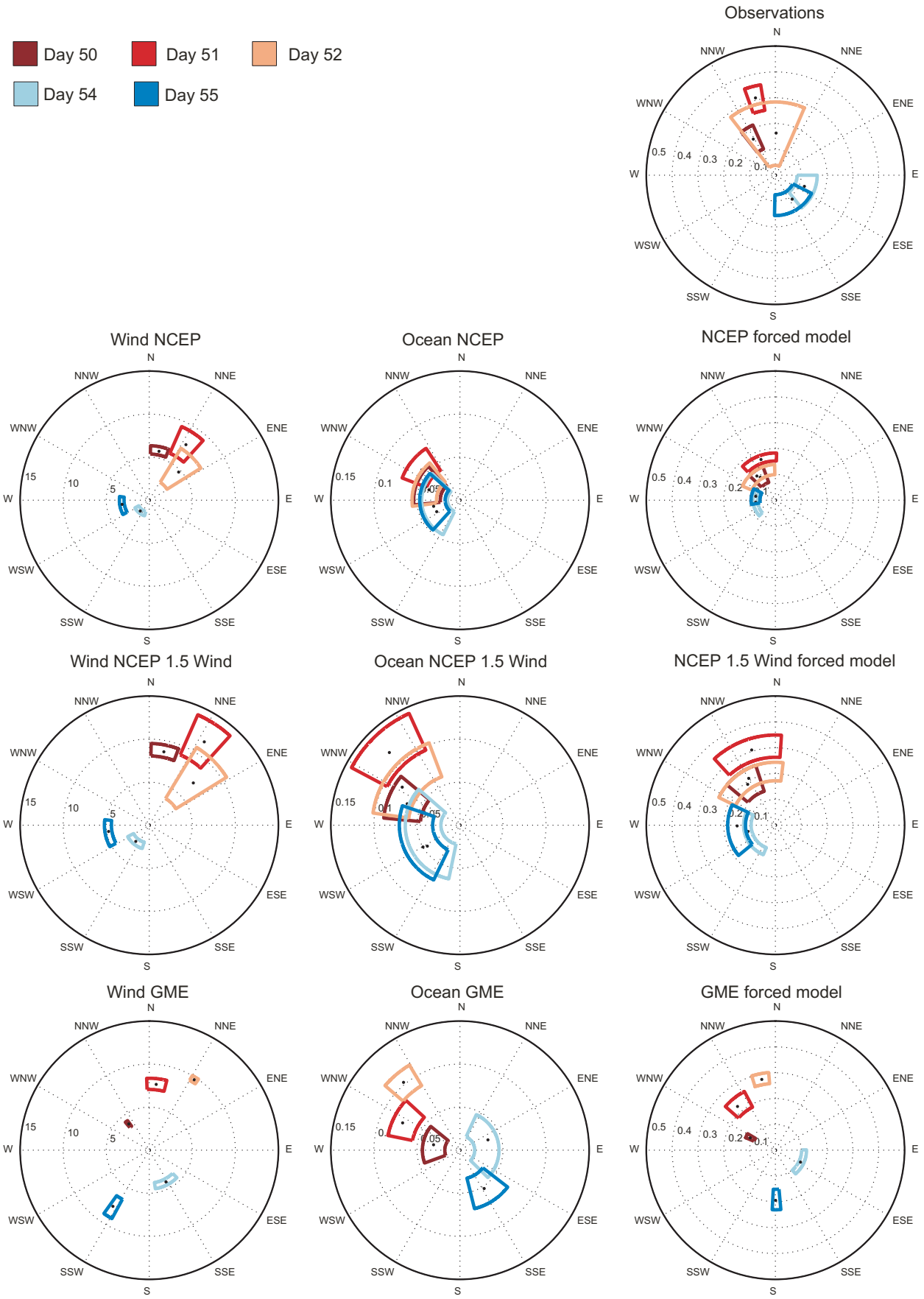

Figure 7. Polar plot showing the range of drift speed and direction for February. The boxes represent 68.3% of the data, the small circles mean values. The directional range of the drift is given by the angle and the magnitude is indicated by the radius.

with the observed open water area than for the NCEP forc- ing. In June, the total area of the polynia increased from

7600 km^2 on day 151 to 34500 km^2 on day 163. During this period, different belts of ice formed parallel to the ice shelf margin and drifted seawards. The open water area is much smaller in size and varies over time (for days 161-163, open water was difficult to detect). The polynia extent obtained from model simulations (using an ice concentration of 70%) is again comparable to the open water area calculated from the SAR images, although the two local maxima observed on days 152 and 157 appear 1-2 days later in the simulations. None of the three different forcings shows a significant better consistency with the observations. We attribute this to the representation of small-scale patterns of the katabatic winds. The inclusion of modelled ice thickness as an additional criterion for detecting the polynia affected only the results modelled at the lower ice concentrations. Our analysis indicates that using a threshold of 70% is a reasonable first choice for retrieving the size of the open water zone in the polynia from the model simulations with FESOM. Considering, however, that we could only study two different polynia events, the most appropriate way to define the extent of 'model' and 'radar' polynia requires further attention.

4.2. Comparison of simulated and observed drift

Figure 6 shows the drift fields for day 152 as obtained from the model simulation forced with NCEP and derived from ASAR images. In general, the drift vectors compare well. At some positions, however, significant deviations were found in the south-east section of the investigated area. Here we see a northward sea ice drift in the observation data but a north-west directed drift in the NCEP forced model data which moves the sea ice parallel to the shelf ice margin. The magnitudes of the drift are similar in both cases.

Figure 7 shows polar plots of observed and simulated ice drift fields together with the wind conditions and ocean surface velocity for the selected days of the summer period (February 2008). Modelling results are provided for the different forcing data. Note that the polar plots depict the direction *to* which the wind is blowing. Here we focus on the general characteristics of velocity fields derived from SAR observations and model simulations. A closer comparison of the effect of different forcing data sets on the simulated ice drift is presented in section 4.4 below.

The mean wind speed for the February polynia event ranged from about 2 to 8 m/s, and the wind was directed towards N - NE during the first four days of the observation period (50 - 53). During the last two days (54 - 55) wind conditions were significantly different: The katabatic winds from southerly directions weakened, the local wind was directed to the coast (WSW - W) with velocities of 1.6 - 3.2 m/s. In particular for these two days, the wind direction and the simulated patterns of ice drift differ substantially between NCEP and GME.

In the model simulations, the velocity vector of the upper ocean layer (the ocean stress term in the momentum balance) is smaller in magnitude than the ice velocity, but its direction is similar to the ice motion in most cases (see Fig. 7, in which the ocean surface velocity resulting from the three forcings is plotted). This indicates that the surface current is dominated by stress exerted from the ice movement. At lower wind speeds, the ocean surface velocity vector reveals slightly different directions relative to the ice drift in the case of GME forcing, indicating that pressure-gradient force becomes more important for the ocean currents here. The differences between the ocean terms obtained for different forcing data occur because the corresponding simulations result in spatial differences of ice conditions (locations of ice types and open water areas) and hence in different spatial distributions of salinity and density.

The simulated ice drift reveals some differences to the observed drift. The velocity of the former is smaller in many cases (a more detailed view is provided in section 4.3). At low wind speeds (days 54 and 55), the results obtained with NCEP forcing show a significant deviation of the drift direction. Since this deviation cannot be explained by the simulated ocean surface speed it indicates that the actual conditions (wind, ocean current, internal ice forces) differ from the situation obtained from the model simulations. The drift based on GME forcing mirrors the change in the wind conditions between day 53 and 54.

The results for the May/June (late fall) period are depicted in Figure 10, now including COSMO-forced simulations. During this period wind conditions are more homogeneous over time (see also Table 1). The average wind direction is from 25° to 35° (NNE) with speeds between 9 and 12 m/s for days 152 to 159 except day 154 with 5 m/s. The last two days (162 and 163) of the observation period reveal lower wind speeds of 4 - 5 m/s. The observations show that the ice drifted northwards with turning angles mainly between 20° and 30° counter-clockwise from the dominant wind direction.

We also carried out simulations for which the NCEP wind speed was multiplied by a factor of 1.5. The reason was to

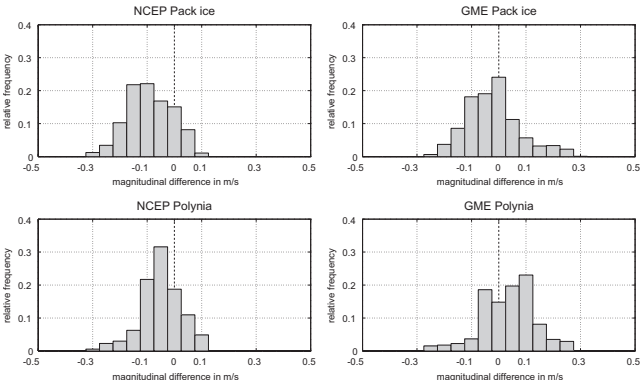

Figure 8. Histograms of differences (model minus observations) in ice drift magnitude between model simulations and ASAR-observations for February, shown separately for pack ice and polynia area.

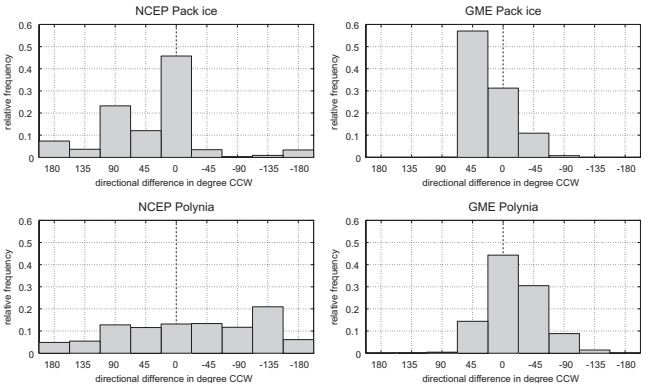

Figure 9. Histograms of differences (model minus observations) in ice drift direction between model simulations and ASAR-observations for February, shown separately for pack ice and polynia area. Positive angles indicate deviations of the modelled drift orientation relative to the observed drift vector in counter-clockwise direction.

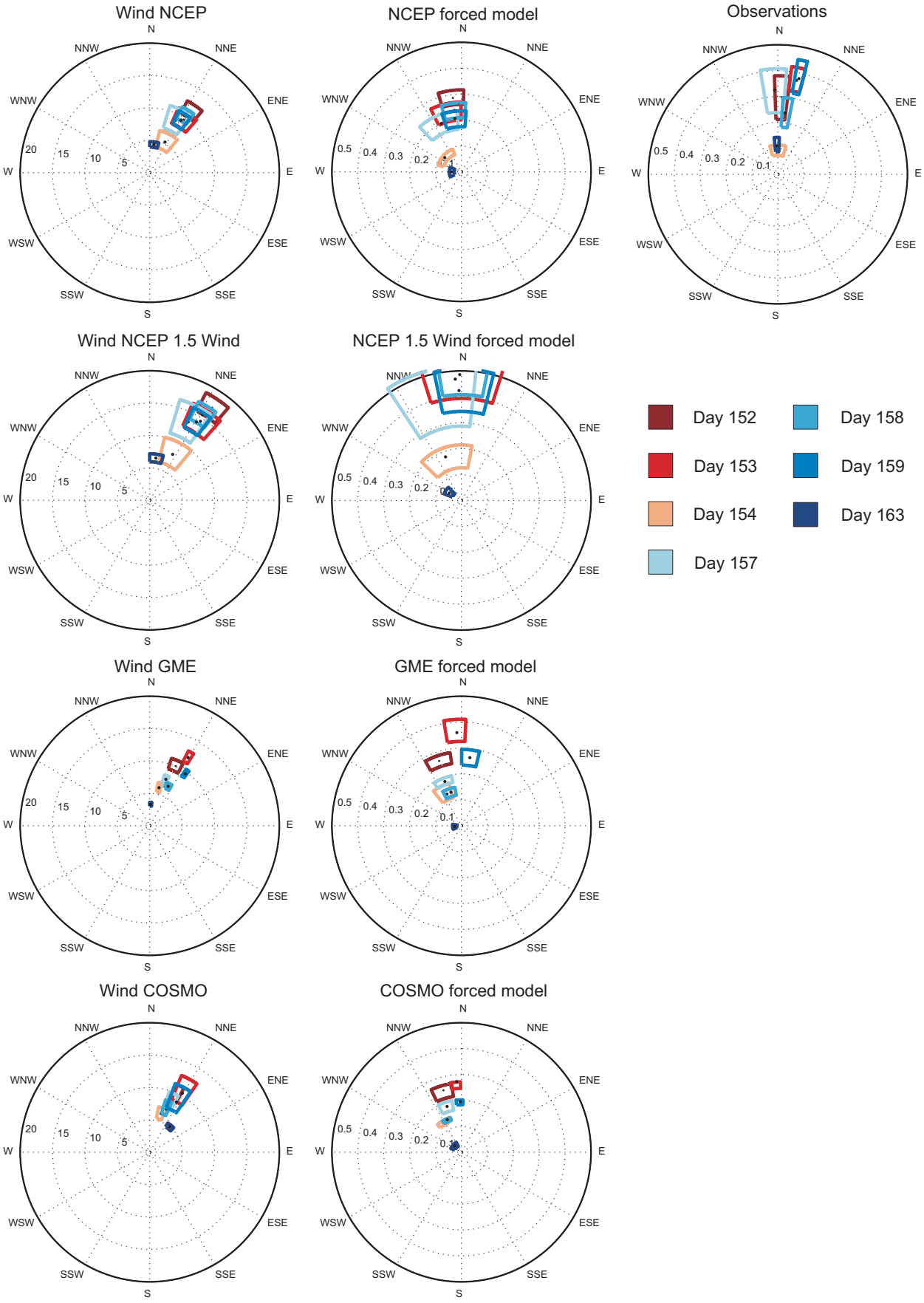

Figure 10. Polar plot for June. See explanation for Fig. 7

study the influence of higher wind speeds on the ice motion. The tests yielded simulated drift directions that are closer to the observed ones, but the ice drift speed was found to

be too large in many cases. (The corresponding results are not shown in the figures.)

4.3. Differences Between Polynia and Pack Ice

Thin sea ice in a polynia may drift with a different velocity than the seaward pack ice, e. g. , by *Haarpainter et al.* [2001]. Therefore, we analysed both areas separately. Note that for the drift analyses from radar images, the polynia area includes the thin ice areas between the coastal belt of open water and the seaward pack ice (Figure 1). In the following, we focus specifically on differences between observed and simulated ice drift patterns that are depicted in Figures 8, 9 (February) and 11, 12 (May/June) in a presentation, for which histograms from all days of the respective observation period were merged. Presence and frequency of distinct structures differ between pack and polynia ice. Structures such as single ice floes and deformation patterns are temporally more stable in the pack ice than in the polynia where sometimes significant deformation of thin ice areas occur within a few hours. In such cases, the accuracy of the calculated drift field in the polynia may be lower. In our tracking results, we did not find indications for critically reduced accuracies. For February, simulated and observed drift speeds do not show any systematic differences between the pack ice and the polynia area. For the drift direction in the polynia, deviations between model and observation are almost equally distributed over the range from -180° to 180° in case of the NCEP-forcing whereas they are focussed on a narrower interval if GME-forcing data are used. The June dataset presented in Figure 12 suggests that under stable wind conditions (dominating wind: N-NNE), the modelled drift directions of the pack ice show a smaller deviation between 0° and 30° counter-clockwise relative to the observations. For the ice in the polynia, the distribution of deviations is wider. The drift magnitudes compare better to observations over the pack ice than to those over the polynia area, where more cases of very low velocities occur. The histograms for pack ice indicate that modelled drift patterns based on GME and COSMO forcing are slightly closer to the observed patterns than the model results based on NCEP-forcing. For the ice in the polynia, the results of different forcing data do not reveal a similar tendency.

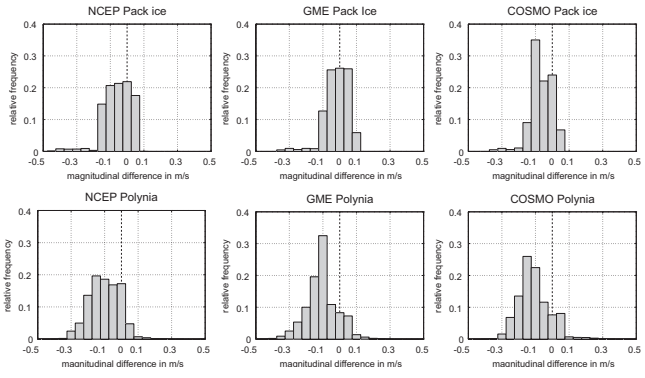

Figure 11. Histograms of differences (model minus observations) in ice drift magnitude between model simulations and ASAR-observations for June, shown separately for pack ice and polynia area.

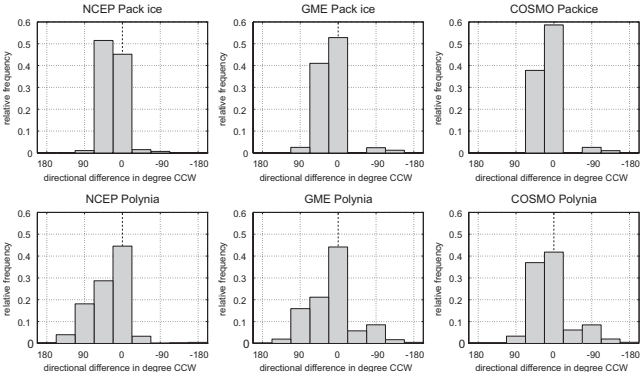

Figure 12. Histograms of differences (model minus observations) in ice drift direction between model simulations and ASAR-observations for June, shown separately for pack ice and polynia area. Positive angles indicate deviations of the modelled drift orientation relative to the observed drift vector in counter-clockwise direction.

4.4. Daily mean differences between modelled and observed ice drift

While the histograms shown in Figures 8 - 12 represent averages over the February and May/June observations, respectively, Figure 13 depicts daily mean magnitudes and direction angles of simulated and observed ice drift vectors for all analysed image pairs from February (summer situation) and May/June (late fall situation). Simulation results are from the model runs with NCEP, GME and COSMO forcings (the latter only for the late fall period). In the Antarctic, the turning angle, i. e. the deviation between drift and wind vector, is to the left of the wind direction, which is also reflected in the ice motion derived from the SAR data (Figures 7 and 10). If, for example, the ice drift is towards North (and drift and wind force are in balance) as in Figure 10, the wind direction is about 20° to 30° towards East which compares well with other observations reported in the literature giving differences between 10° and 25°.

In February, the mean daily drift direction simulated by the GME-forcing coincides very well with the observed data, whereas larger deviations occur with NCEP forcing, in particular during the last two days of the observation period for which the NCEP data exhibit low wind speeds and a large change in wind direction (see Fig. 7). The difference of magnitudes is also smaller for the GME- than for the NCEP forcing. While the latter results in smaller simulated drift velocities than those observed, positive and negative

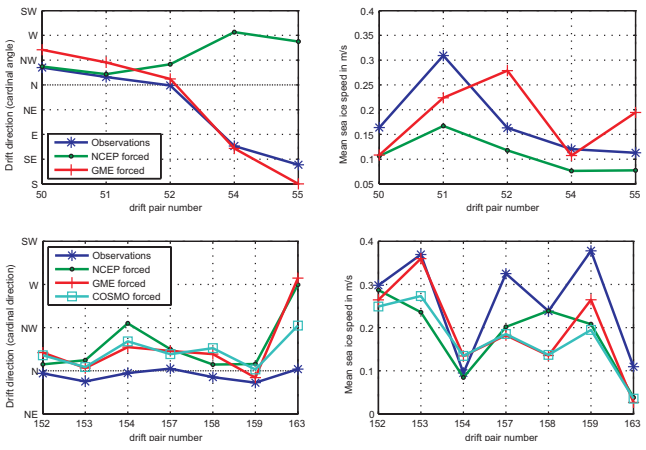

Figure 13. Mean magnitude and direction angle of ice drift for February (top) and May/June (bottom) obtained with different forcings.

deviations are found for the former. At maximum, the simulated ice drift velocities may differ from observations by a factor of 3. Using the NCEP forcing, the turning angle is too large in particular at the later days of the observation period when the wind was weakening.

In the late fall situation, the agreement between simulated and observed mean drift directions is sufficient for the different forcing data, although the simulated turning angles are larger than observed. Exceptionally large differences occur at low wind speeds (day 163). The simulated magnitudes of ice velocity are too small except at one day (154) with low wind velocity. On some days (153 and 154) GME and COSMO forcing provide results closer to the observed magnitudes, on other days (152, 157, 158) differences are smallest with the NCEP forcing. For COSMO and GME, the signs of day-to-day velocity changes (positive, negative) are the same as for the observed velocity curve, hence the tendency of daily velocity changes in and around the polynia is reproduced. This is not the case for the NCEP forcing which probably is the result of the coarser temporal and spatial resolution. The better agreement of the model forced with NCEP data for the late fall period compared to its performance in summer could be due to the more stable wind conditions in May/June (compare Figs. 7 and 10).

5. Discussion

The comparisons between model simulations of sea ice drift in the polynia area and drift patterns derived from SAR images presented in the preceding sections revealed differences in magnitudes and directions of ice drift vectors. Compared to the ice drift velocity derived from satellite data, the model output contains smaller drift velocities in many cases. A possible reason for the systematically low drift velocities is the underestimation of wind speed in the forcing data for this specific region and ice conditions. This assumption is supported by our analysis of the wind factor discussed below. Studies for other regions like the Amundsen Sea [*Assmann et al.*, 2005] and the Laptev Sea [*Ernsdorf et al.*, 2011] e. g. , also found that wind speed values in the NCEP data were too low. In our case, an artificial increase of the NCEP wind by 1.5 resulted in an overestimation of ice speeds in many cases but in a better approximation of the drift direction.

The agreement of modelled drift direction with observations is better over the consolidated pack ice than for the thin ice in the polynia. To some extent, this can be explained by the fact that the model does not include a sharp boundary between the thin ice area in the polynia and the adjacent pack ice. We have also to consider the inevitable limitations in horizontal discretisation of model equations. Within the polynia, high freezing rates occur connected with strong brine rejection. The surface salinity increases fast but not with an even distribution. Local differences lead to strong density gradients that induce large small-scale variations of ocean surface velocities. Via the ice-ocean drag parametrisation these velocities are superimposed on the comparatively smooth driving effect of the wind field. Thus, simulated ice drift within the polynia features a larger directional spread than simulated ice drift of the consolidated ice. It seems that in reality the density gradients level out on a very small scale keeping the induced ocean velocities low and much more local and eventually adding far less 'noise' to the wind-induced ice drift pattern.

While model simulations can be carried out with a high temporal resolution (on the order of minutes), the resolution of the drift vector fields derived from satellite data is usually much coarser (between 5 and 29 hours, in most cases 24 hours). We note that the time periods we selected for investigations were the most suitable regarding the duration of polynia activity and number of SAR image acquisitions available for the region of interest. A possible solution to reduce the temporal gaps between satellite images is to combine different sensors (radar, thermal infrared, and passive microwave data) but the optimal merging of the different data products needs to be further developed. Recent and future satellite constellations such as COSMO SkyMED and Sentinel-1 will give the opportunity to gather radar images sequences with higher temporal resolutions. We note that shorter temporal gaps between two SAR images may require also better spatial image resolutions for the ice displacement to be detectable.

The employment of a coupled sea ice ocean model to study polynia dynamics can be regarded as a useful complement to the more specialized flux balance models first formulated by *Pease* [1987] and subsequently studied further by several authors [e. g. *Haarpainter et al.*, 2001; *Skogseth et al.*, 2004; *Krumpen et al.*, 2011a]. A disadvantage of the flux balance models is that they neglect ice-ocean interactions, the ice rheology, and boundary conditions (imposed, e. g. by blocking effects of land or pack ice adjacent to the polynia). A detailed comparison of both approaches is beyond the scope of our study. However, in the following we will focus on the aspect of the implementation of sea ice drift in the flux balance models. Based on previous studies *Van Woert* [1999] assumed that in the Antarctic, the ice drift velocity amounts to 3 - 3.5% of the wind speed measured in 10 m height, independent of the internal ice stress. This value is valid for free ice drift and thus represents the possible maximum. *Van Woert* [1999] reduced this velocity by 5% of the ice thickness given in meters to roughly account for the ocean drag. *Haarpainter et al.* [2001] used a value of 3% of the wind speed (i. e. a "wind factor" of 0.03) for the drift of consolidated ice away from the open water edge, and a value of 1% for the pack ice adjacent to the polynia for simulations of polynia events in the Arctic.

For the days of polynia events investigated in our study we calculated the wind factor from the atmospheric forcing data. For the NCEP forcing, the results are shown in Figure 14. Both the output of FESOM simulations and SAR observations reveal significant variations. The wind factor derived from SAR observations is consistently larger than the one from simulations. For May/June, modelled values are below 3%, in February, higher values were found for days 54 and 55. These days are characterized by significant changes in wind speed and direction (Figure 7), which means that ice drift and wind momentum transfer are not in balance for some time. The simulated wind factors of the ice in the polynia area and the pack ice are similar. The relatively large values of the wind factor obtained using the drift observations is a clear indication that NCEP reanalysis wind speeds are too small. The observations indicate that velocities of consolidated thin ice in the polynia and pack ice may be different at some occasions. Figure 14 reveals that sometimes the pack ice moves faster than the polynia ice, and sometimes it is vice versa. We attribute this to different responses of the respective ice types to the wind and ocean forcing (e. g. more and higher ridges / deeper keels in the pack ice zone), and to the ice deformation in particular of the thin ice in the polynia.

According to the momentum balance equation, five different forces act on the ice cover: wind stress, ocean stress, internal ice stress, the Coriolis force and a force due to the surface tilt. The latter is unimportant over the spatial scales and time periods to be considered for studying a polynia event [e. g. *Wadhams*, 2000, chapter 4]. The Coriolis force only depends on the ice mass per unit area and on the drift velocity and is therefore well-constraint. More critical is the parametrisation of wind, ocean, and internal ice stress. In particular the interaction of the ice with ocean and tidal currents is complicated [e. g. *McPhee*, 2012]. The

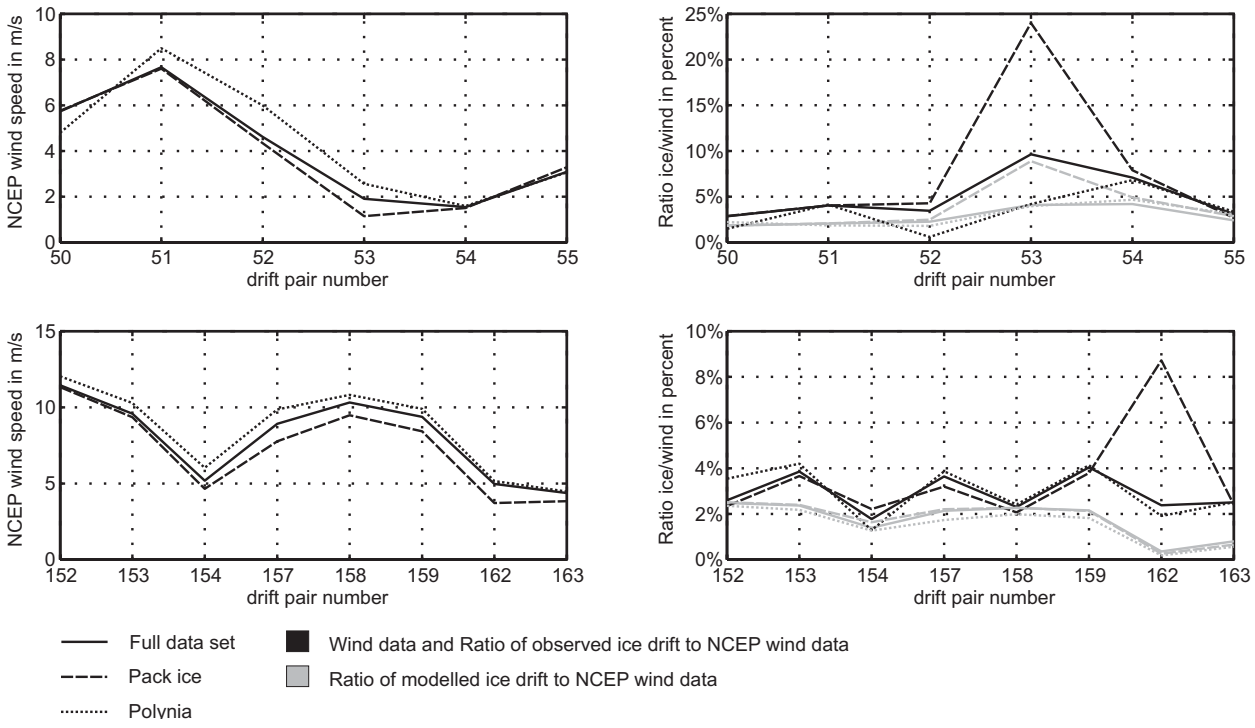

Figure 14. Wind speed and corresponding wind factors based on NCEP wind data.

upper ocean layer may slow down the wind-induced movement of an ice floe, but a strong current may accelerate the ice if the wind is weak. Hence, to develop atmosphere and ocean drag parametrisations, data from drifting buoys, ocean moorings equipped with sonar and current meters and surface and under-ice devices to measure atmospheric and hydraulic roughness are required. For more detailed analyses of the internal ice stress, the characteristics of ice deformation can be derived from the observed ice motion field [*Lindsay et al.*, 2003]. As we have shown in this study, SAR image sequences can provide drift patterns at a high spatial resolution. Radar measurements are sensitive to ice surface roughness [*Dierking et al.*, 1997] and provide information on ice deformation patterns (ridges, rafting zones) if the image resolution is sufficiently high (better than 10 m) [*Dierking and Dall*, 2007]. However, the development of measurement strategies using satellite instruments and of corresponding retrieval algorithms for parameters needed to estimate atmospheric and hydraulic drag is still in a premature stage and requires further investigations.

In the model the polynia area is defined using a sea ice concentration of 70% as threshold (see section 3.1). The reason is that ice concentration is one of the prognostic variables provided by the simulations. When looking at the evolution of the polynias in our SAR images, we found that the polynia consisted of a strip of open water and one or more belts of thin ice further seawards, formed perpendicular to the wind direction. These strips are separated by relatively sharp boundaries, see e. g. Figure 1. Hence, we have an abrupt transitions from an ice concentration of close to zero to almost (100%). A determination of the sea ice concentration from the ASAR images is not reliable because of a general difficulties to distinguish between small open water patches and the ice around. The identification of different ice types and water in the polynia is easier if multi-channel radar data supplemented with infrared imagery are available. The term "multi-channel" includes both different polarizations and different radar frequencies. Our results showed that, when evaluating the area of a polynia from ice concentrations between 30% and 70%, the simulated sizes are close to the open water area observed in the SAR images. This excludes the seaward thin ice belts which should be considered part of the polynia because of their larger heat exchange with the atmosphere and the brine rejection into the ocean layer below. Further studies are planned concerning the use of modelled ice thickness to delimit the total area of the polynia (open water and thin ice) from the seaward pack ice.

6. Conclusion

The evolution of polynias has been discussed in a number of publications based on local flux-balance models [e. g. *Haarpainter et al.*, 2001; *Drucker and Martin*, 2003; *Krumpen et al.*, 2011a, b]. In this study, we investigated simulations of polynia events on an unstructured grid by using the coupled sea-ice ocean model FESOM, which makes it possible to carry out simulations close to the coast in high resolution. The advantage of employing a coupled sea ice ocean model is that interactions between sea ice and ocean currents, the influence of the internal ice stress, and of boundary conditions (e. g. course of the coastline or of the ice shelf margin) can be adequately taken into account. We concentrated on variations of the areal extent and the ice drift in and adjacent to the Ronne Polynia, which is located in the Weddell Sea, Antarctica. Modelling results were compared to polynia area and ice drift patterns derived from image sequences acquired by satellite synthetic aperture radar in summer and late fall 2008. In the modelling simulations, we used atmospheric forcing data sets that differed in spatial and temporal resolution (NCEP, GME, and COSMO). From the comparison, we draw the following conclusions:

- When identifying the polynia in the model as the zone with ice concentrations <70%, we found that the sizes of the open water zone in the polynia coincided well between model and observations, although the simulated temporal variations exhibited a delay relative to the results derived from the SAR images (Figures 4 and 5). The use of an

atmospheric forcing with higher spatial resolution (GME) improved the accuracy of the simulations in the summer case. We assume that sudden outbursts of katabatic winds are not adequately represented in the forcing data. When defining the polynia area as the zone with ice concentrations <70%, belts of thin ice between the coastal open water zone and the seaward pack ice boundary are not included in the model polynia.

• With regard to magnitude and direction of the simulated ice drift vectors the results differed between summer and late fall (Fig. 9 and 11). In summer the agreement with the results from the SAR images was better using the high resolution forcing data; in the latter case, systematic differences between results of single forcing data were not found which we attribute to the more stable wind conditions in June. In many but not all cases, the drift velocities from the model runs are too small, and turning angles are slightly too large relative to the data obtained from the radar imagery. A possible reason for this is that the velocity of the wind forcing data may be too low as it was already shown for other regions in case of NCEP reanalysis data [*Assmann et al.*, 2005; *Ernsdorf et al.*, 2011].

• The wind factor (ratio between ice drift velocity and wind speed) is needed as input to the flux balance models for simulations of polynia area variations. Our results indicate that the wind factor is not constant but varies in particular if wind conditions change within short time intervals. If the wind is weakening, the influence of the ocean and/or internal ice stress may be dominant. In such cases, the use of a "wind factor" is of limited value. This problem does not occur in simulations using a coupled sea-ice ocean model.

In summary, our study shows that the FESOM model provides realistic simulations of the evolution of the Ronne Polynia. The quality of such simulations depends on the spatial and temporal resolution of the atmospheric forcing data. The study also demonstrates the usefulness of high-resolution satellite radar imagery for gathering validation data.

Acknowledgments. The work of the first author is funded by the Alfred Wegener Institute in the framework of the German Earth Observing Network (Network EOS). The modelling work in this study was funded by Deutsche Forschungsgemeinschaft SPP Antarktisforschung (grants TI 296/5, HE 2740/10). W. Dierking's contribution to this study is part of the EU 7th Framework project SIDARUS (grant agreement no. 262922). The SAR images were provided by ESA for the Cat-1 project C1P.5024.

References

Assmann, K. M., H. H. Hellmer, and S. S. Jacobs (2005), Amundsen sea ice production and transport, *Journal of Geophysical Research*, *110*(C12013), 17, doi:10.1029/2004JC002797.

Baldauf, M., J. Förstner, S. Klink, T. Reinhardt, C. Schraff, A. Seifert, and K. Stephan (2011), Kurze Beschreibung des Lokal-Modells Kürzestfrist COSMO-DE (LMK) und seiner Datenbanken auf dem Datenserver des DWD, *Tech. rep.*, Deutscher Wetterdienst, Offenbach, Germany, 75 pages.

Berens, P. (2009), Circstat: A matlab toolbox for circular statistics, *Journal of Statistical Software*, *31*(10), 1–21.

Ciappa, A., L. Pietranera, and G. Budillon (2012), Observations of the terra nova bay (antarctica) polynya by MODIS ice surface temperature imagery from 2005 to 2010, *Remote Sensing of Environment*, *119*, 158–172, doi:10.1016/j.rse.2011.12.017.

Connolley, W. M., J. M. Gregory, E. Hunke, and A. J. McLaren (2004), On the consistent scaling of terms in the sea-ice dynamics equation, *Journal of Physical Oceanography*, *34*, 1776–1780.

Curlander, J., B. Holt, and K. Hussey (1985), Determination of sea ice motion using digital SAR imagery, *IEEE Journal of Oceanic Engineering*, *10*(4), 358 – 367, doi:10.1109/JOE.1985.1145134.

Dee, D. P., et al. (2011), The ERA-interim reanalysis: configuration and performance of the data assimilation system, *Quarterly Journal of the Royal Meteorological Society*, *137*(656), 553–597, doi:10.1002/qj.828.

Dierking, W., and J. Dall (2007), Sea-ice deformation state from synthetic aperture radar imagery - part i: Comparison of C- and L-band and different polarization, *IEEE Transactions on Geoscience and Remote Sensing*, *54*(11), 3610–3622, doi:10.1109/TGRS.2007.903711.

Dierking, W., A. Carlstrom, and L. M. H. Ulander (1997), The effect of inhomogeneous roughness on radar backscattering from slightly deformed sea ice, *IEEE Transactions on Geoscience and Remote Sensing*, *35*(1), 147–159, doi:10.1109/36.551943.

Drucker, R., and S. Martin (2003), Observations of ice thickness and frazil ice in the st. lawrence island polynya from satellite imagery, upward looking sonar, and salinity/temperature moorings, *Journal of Geophysical Research*, *108*(C5), 3149, doi:10.1029/2001JC001213.

Ernsdorf, T., D. Schröder, S. Adams, G. Heinemann, R. Timmermann, and S. Danilov (2011), Impact of atmospheric forcing data on simulations of the laptev sea polynya dynamics using the sea-ice ocean model FESOM, *Journal of Geophysical Research*, *116*(C12038), 18, doi:10.1029/2010JC006725.

Fiedler, E. K., T. A. Lachlan-Cope, I. A. Renfrew, and J. C. King (2010), Convective heat transfer over thin ice covered coastal polynyas, *Journal of Geophysical Research*, *115*(C10051), 19, doi:10.1029/2009JC005797.

Fischer, H. (1995), Vergleichende Untersuchungen eines optimierten dynamisch-thermodynamischen Meereismodells mit Beobachtungen im Weddellmeer, *Berichte zur Polarforschung 166*, alfred-Wegener-Institut, Bremerhaven.

Gent, P. R., and J. C. McWilliams (1990), Isopycnal mixing in ocean circulation models, *Journal of Physical Oceanography*, *20*, 150–155, doi:10.1175/1520-0485(1990)020⟨0150:IMIOCM⟩2.0.CO;2.

Gill, A. (1973), Circulation and bottom water production in the weddell sea, *Deep Sea Research and Oceanographic Abstracts*, *20*(2), 111–140, doi:10.1016/0011-7471(73)90048-X.

Haarpainter, J., J.-C. Gascard, and P. M. Haugan (2001), Ice production and brine formation in storfjorden, svalbard, *Journal of Geophysical Research*, *106*(C7), 14,001–14,013, doi:10.1029/1999JC000133.

Hibler III, W. D. (1979), A dynamic-thermodynamic sea ice model, *Journal of Physical Oceanography*, *9*(4), 815–846.

Hollands, T., and W. Dierking (2011), Performance of a multiscale correlation algorithm for the estimation of sea ice drift from sar images: initial results, *Annals of Glaciology*, *52*(57), 311–317, doi:10.3189/172756411795931462.

Hunke, E. C., and J. K. Dukowicz (1997), An elastic-viscous-plastic model for sea ice dynamics, *Journal of Physical Oceanography*, *27*, 1849–1868, doi:10.1175/1520-0485(1997)027⟨1849:AEVPMF⟩2.0.CO;2.

Hunke, E. C., and W. H. Lipscomb (2001), CICE: The Los Alamos Sea Ice Model, Documentation and Software User's Manual, *LACC-98-16*, *v.3.*, Los Alamos National Laboratory, Los Alamos, USA.

Jackett, D. R., and T. J. McDougall (1995), Stabilization of hydrographic data, *Journal of Atmospheric and Oceanic Technology*, *12*, 381–389, doi:10.1029/2000JC000720.

Kalnay, E., et al. (1996), The NCEP/NCAR 40-year reanalysis project, *Bulletin of the American Meteorological Society*, *77*, 437–471, doi:10.1175/1520-0477(1996)077⟨0437:TNYRP⟩2.0.CO;2.

Kern, S. (2009), Wintertime antarctic coastal polynya area: 1992 - 2008, *Geophysical Research Letters*, *36*(L14501), 5, doi:10.1029/2009GL038062.

Krumpen, T., S. Willmes, M. A. M. Maqueda, C. Haas, J. Hölemann, R. Gerdes, and D. Schröder (2011a), Evaluation of a polynya flux model by means of thermal infrared satellite estimates, *Annals of Glaciology*, *52*(57), 52–60, doi:10.3189/172756411795931615.

Krumpen, T., et al. (2011b), Sea ice production and water mass modification in the eastern laptev sea, *Journal of Geophysical Research*, *116*(C05014), 17, doi:10.1029/2010JC006545.

Le Brocq, A. M., A. J. Payne, and A. Vieli (2010), An improved antarctic dataset for high resolution numerical ice sheet models (ALBMAP v1), *Earth System Science Data*, *2*, 247–260, doi:10.5194/essd-2-247-2010.

Leppäranta, M. (1983), A growth model for black ice, snow ice, and snow thickness in subarctic basins, *Nordic Hydrology*, *14*(2), 59–70, doi:10.2166/nh.1983.006.

Lindsay, R. W., J. Zhang, and D. A. Rothrock (2003), Sea-ice deformation rates from satellite measurements and in a model, *Atmosphere–Ocean*, *41*(1), 35–47, doi:10.3137/ao.410103.

Lüpkes, C., V. M. Gryanik, B. Witha, M. Gryschka, S. Raasch, and T. Gollnik (2008), Modeling convection over arctic leads with LES and a non-eddy-resolving microscale model, *Journal of Geophysical Research*, *113*(C09028), 17, doi:10.1029/2007JC004099.

Lythe, M. B., D. Vaughan, and the BEDMAP Consortium (2001), BEDMAP: A new ice thickness and subglacial topographic model of antarctica, *Journal of Geophysical Research*, *106*(B6), 11,335–11,351, doi:10.1029/2000JB900449.

Majewski, D., D. Liermann, P. Prohl, B. Ritter, M. Buchhold, T. Hanisch, G. Paul, W. Wergen, and J. Baumgardner (2002), The operational global icosahedral-hexagonal gridpoint model GME: Description and high-resolution tests, *Monthly Weather Review*, *130*, 319–338, doi:10.1175/1520-0493(2002)130⟨0319:TOGIHG⟩2.0.CO;2.

Maqueda, M. A. M., A. J. Willmott, and N. R. T. Biggs (2004), Polynya dynamics: A review of observations and modelling, *Review of Geophysics*, *42*(RG1004), 37, doi:10.1029/2002RG000116.

Massom, R. A., P. T. Harris, K. J. Michael, and M. J. Potter (1998), The distribution and formative processes of latent-heat polynyas in east antarctica, *Annals of Glaciology*, *27*, 420–426.

Mathiot, P., N. C. Jourdain, B. Barnier, H. Galle, jean Marc Molines, J. L. Sommer, and T. Penduff (2012), Sensitivity of coastal polynyas and high-salinity shelf water production in the ross sea, antarctica, to the atmospheric forcing, *Ocean Dynamics*, *62*(5), 701–723, doi:10.1007/s10236-012-0531-y.

McPhee, M. G. (2012), Advances in understanding iceocean stress during and since aidjex, *Cold Regions Science and Technology*, *76-77*, 24–36, doi:10.1016/j.coldregions.2011.05.001, max Coon Special issue.

Ninnis, R. M., W. J. Emery, and M. J. Collins (1986), Automated extraction of pack ice motion from advanced very high resolution radiometer imagery, *Journal of Geophysical Research*, *91*(C96), 10,725–10,734, doi:10.1029/JC091iC09p10725.

Owens, W. B., and P. Lemke (1997), Sensitivity studies with a sea ice-mixed layer-pycnocline model in the Weddell Sea, *Journal of Geophysical Research*, *95*(C6), 9527–9538, doi:10.1029/JC095iC06p09527.

Pacanowski, R. C., and S. G. H. Philander (1981), Parameterization of vertical mixing in numerical models of the tropical oceans, *Journal of Physical Oceanography*, *11*, 1443–1451, doi:10.1175/1520-0485(1981)011⟨1443:POVMIN⟩2.0.CO;2.

Parkinson, C. L., and W. M. Washington (1979), A large-scale numerical model of sea ice, *Journal of Geophysical Research*, *84*(C1), 311–337, doi:10.1029/JC084iC01p00311.

Pease, C. H. (1987), The size of wind-driven coastal polynyas, *Journal of Geophysical Research*, *92*(C7), 7049–7059, doi:10.1029/JC092iC07p07049.

Redi, M. H. (1982), Oceanic isopycnal mixing by coordinate rotation, *Journal of Physical Oceanography*, *12*, 1154–1158, doi:10.1175/1520-0485(1982)012⟨1154:OIMBCR⟩2.0.CO;2.

Renfrew, I. A., J. C. King, and T. Markus (2002), Coastal polynyas in the southern Weddell Sea: Variability of the surface energy budget, *Journal of Geophysical Research*, *107*(C6), 3063, doi:10.1029/2000JC000720.

Schröder, D., G. Heinemann, and S. Wilmes (2011), The impact of a thermodynamic sea-ice module in the COSMO numerical weather prediction model on simulations for the Laptev Sea, Siberian Arctic, *Polar Research*, *30* , 6334, doi:103402/polar.v30i0.6334..

Semtner Jr., A. J. (1976), A model for the thermodynamic growth of sea ice in numerical investigations of climate, *Journal of Physical Oceanography*, *6*(3), 379–389, doi:10.1175/1520-0485(1976)006⟨0379:AMFTTG⟩2.0.CO;2.

Skogseth, R., P. M. Haugan, and J. Haarpaintner (2004), Ice and brine production in storfjorden from four winters of satellite and in situ observations and modeling, *Journal of Geophysical Research*, *109*(C10008), 15, doi:10.1029/2004JC002384.

Steele, M., R. Morley, and W. Ermold (2001), PHC: A global ocean hydrography with a high quality Arctic Ocean, *Journal of Climate*, *14*, 2079–2087, doi:10.1175/1520-0442(2001)014⟨2079:PAGOHW⟩2.0.CO;2.

Thomas, M. V., C. A. Geiger, and C. Kambhamettu (2008), High resolution (400 m) motion characterization of sea ice using ERS-1 SAR imagery, *Cold Regions Science and Technology*, *52*(2), 207–223, doi:10.1016/j.coldregions.2007.06.006.

Thomas, M. V., C. A. Geiger, and C. Kambhamettu (2009), Mapping of large magnitude discontinuous sea ice motion, *SIGSPATIAL Special*, *1*(1), 45–50, doi:10.1145/1517463.1517469.

Thomas, M. V., C. Kambhamettu, and C. A. Geiger (2011), Motion tracking of discontinuous sea ice, *IEEE Transactions on Geoscience and Remote Sensing*, *49*(12), 5064 – 5079, doi:10.1109/TGRS.2011.2158005.

Timmermann, R., A. Beckmann, and H. H. Hellmer (2002), Simulations of ice-ocean dynamics in the weddell sea - 1. model configuration and validation, *Journal of Geophysical Research*, *107*(C3), 3024, doi:10.1029/2000JC000741.

Timmermann, R., S. Danilov, J. Schröter, C. Böning, D. Sidorenko, and K. Rollenhagen (2009), Ocean circulation and sea ice distribution in a finite element global sea ice–ocean model, *Ocean Modelling*, *27*(3–4), 114–129, doi:10.1016/j.ocemod.2008.10.009.

Timmermann, R., et al. (2010), A consistent dataset of Antarctic ice sheet topography, cavity geometry, and global bathymetry, *Earth System Science Data*, *3*(2), 261–273, doi:10.5194/essd-2-261-2010.

Van Woert, M. L. (1999), Wintertime dynamics of the terra nova bay polynya, *Journal of Geophysical Research*, *104*(C4), 7753–7769, doi:10.1029/1999JC900003.

Wadhams, P. (2000), *Ice in the Ocean*, 351 pp., Gordon and Breach, Amsterdam, The Neatherlands.

Wang, Q. (2007), The Finite Element Ocean Model and its aspect of vertical discretization, *Dissertation*, university of Bremen, Bremen, Germany. http://nbn-resolving.de/urn:nbn:de:gbv:46-diss000108304.

Wendler, G., D. Gilmore, and J. Curtis (1997), On the formation of coastal polynyas in the area of commonwealth bay, eastern antarctica, *Atmospheric Research*, *45*(1), 55–75, doi:10.1016/S0169-8095(97)00024-0.

Willmes, S., T. Krumpen, S. Adams, L. Rabenstein, C. Haas, J. Hölemann, S. Hendricks, and G. Heinemann (2010), Cross-validation of polynya monitoring methods from multisensor satellite and airborne data: a case study for the laptev sea, *Canadian Journal of Remote Sensing*, *36*(S1), 196–210, doi:10.5589/m10-012.

World Meteorological Organisation (1970), WMO sea-ice nomenclature, terminology, codes and illustrated glossary, *Report 259*, World Meteorological Organisation (WMO/OMM/BMO), Geneva, Switzerland.

W. Dierking, EOS / Polar Meteorology, Climate Science Division, Alfred Wegener Institute for Polar and Marine Research, Bussestraße 24, 27570 Bremerhaven, Germany.(wolfgang.dierking@awi.de)

L. Ebner, Department of Environmental Meteorology, Faculty of Geosciences, University of Trier, Trier, Germany.(ebner@uni-trier.de)

V. Haid, Climate dynamics, Climate Science Division, Alfred Wegener Institute for Polar and Marine Research, Bussestraße 24, 27570 Bremerhaven, Germany.(verena.haid@awi.de)

T. Hollands, EOS / Polar Meteorology, Climate Science Division, Alfred Wegener Institute for Polar and Marine Research, Bussestraße 24, 27570 Bremerhaven, Germany.(thomas.hollands@awi.de)

R. Timmermann, Climate dynamics, Climate Science Division, Alfred Wegener Institute for Polar and Marine Research, Bussestraße 24, 27570 Bremerhaven, Germany.(ralph.timmermann@awi.de)

A.3 PAPER III: JOURNAL OF SELECTED TOPICS IN APPLIED EARTH OBSERVATIONS AND REMOTE SENSING

"Reliability measures for sea ice motion retrieval from synthetic aperture radar images"

manuscript prepared for submission to Journal of Selected Topics in Applied Earth Observations and Remote Sensing

Reliability measures for sea ice motion retrieval from synthetic aperture radar images

Thomas Hollands, Stefanie Linow, and Wolfgang Dierking

***Abstract*—We evaluate the reliability of sea ice motion estimates derived from SAR images. Ice drift is obtained using a pattern-based cascaded multi-resolution motion tracking algorithm. The correlation coefficient as a measure of tracking quality is evaluated by comparing the resulting drift fields to reference data. We found that the magnitude of the correlation coefficient is not a sufficient criterion for the reliability of the derived motion field. Therefore, we introduce a combination of textural measures that provide information about the suitability of the respective image region for pattern matching. Additionally, we use back-matching as a technique to validate the consistency of drift field estimates. By combining the correlation coefficient with the magnitudes of selected texture parameters and the back-matching result, we obtain a reliable quality measure for the calculated velocities.**

I. Introduction

WHEN dealing with sea ice drift fields which were automatically retrieved from radar satellite imagery, ground truth for an assessment of their accuracy is often not available. However, it is necessary to be aware of the potential uncertainty of retrieved drift (or displacement) fields to employ the data for other applications (e.g. assimilation in sea ice models, operational forecast of sea ice conditions). Therefore it is desirable to identify some reliability parameters for the quality of the results. In Figure 1 we plotted the deviation

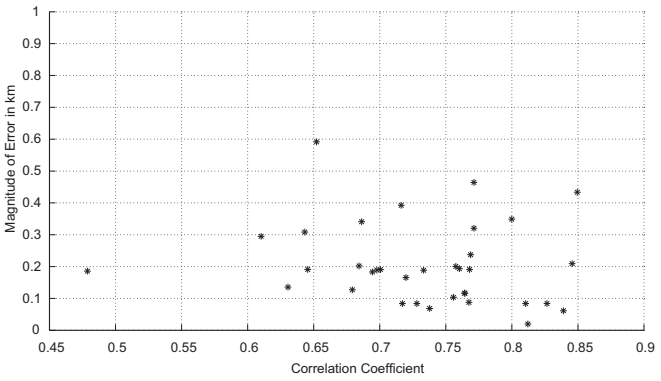

Fig. 1. Magnitude of error vs. cross-correlation coefficient for an image pair of the Ronne Polynia, Antarctica (22. / 23. 02. 2008)

between the drift estimate and our reference data as a function of the cross-correlation coefficient. One would expect a high cross-correlation coefficient to indicate that patterns are more similar, and that the found match is therefore more reliable than a match with a lower correlation coefficient. Figure 1, however, does not indicate any significant relation between the error and the correlation coefficient, and we conclude that the correlation coefficient cannot be regarded as a suitable measure for the reliability of the pattern matching algorithm. Vernon, 2001 [1] already states that correlation methods are not able to resolve regions of discontinuity. Not only the cross-correlation, but also the phase correlation is only a weak indicator for the quality of an estimated motion field [2]. Therefore, the reliability has to be based on other measures as well. The motivation of this work is to assess the usefulness of different parameters as quality measures for the retrived ice drift. We distinguish two different classes of measures: (1) parameters, which indicate whether a given area in the image is suitable for pattern-matching and which are applied on single images, and (2) procedures, which help to assess the success of matching and therefore need image pairs as input. In the following sections we describe selected textural parameters and the back-matching procedure, which are used to assess the potential of single images and image pairs, respetively, for successful pattern-matching. We assess the errors of a cascaded multi-resolution drift algorithm and present maps for the selected reliability measures.

II. Methods

As examples we present drift field calculation based on Envisat ASAR wide swath data acquired over the Ronne Polynia[1] in 2008, which are described in [3]. The image pairs were recorded on the following days: 18. / 19. 02. 2008, 19. / 20. 02. 2008, 22. / 23. 02. 2008, 30. / 31. 05. 2008, and 31. 05. / 01. 06. 2008. Figure 2 shows the location of the Ronne Polynia. For an independent validation of the drift algorithm, we manually determined displacements of ice structures for each satellite image pair. Ice drift velocities are then calculated from the ratio between displacement and time between the acquisitions of the two respective SAR images. The accuracy of the manually derived displacement data is 1-2 pixel, depending on the quality of the original images. For our drift estimates we applied a cascaded multi-scale resolution algorithm first described by Thomas, 2008 [4] and modified by Hollands, 2011 [5]. It is an area-based pattern-matching algorithm, which employs a combination of phase correlation and normalised cross correlation to determine the displacements of ice structures between two satellite images.

T. Hollands, S. Linow and W. Dierking are with the Department of Climate Sciences, Alfred Wegener Institute for Polar and Marine Research, Bremerhaven, D-27570, Germany e-mail: thomas.hollands@awi.de).

[1] A polynia is a region of open water in the pack ice where new ice forms. It is caused by katabatic winds or ocean currents which push the sea ice away from a coastline, or by upwelling of warm water.

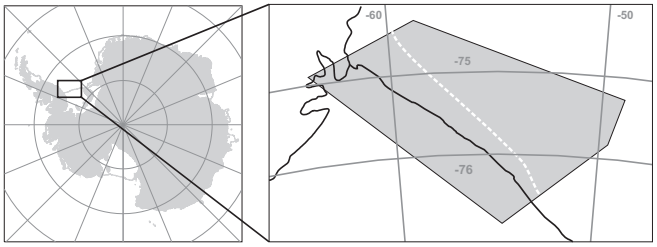

Fig. 2. Location of the test site. The zoomed region contains the overlapping area of the image pair recorded on the 18. / 19. 02. 2008. The dashed line denotes the approximate position of the polynia.

Similar to the approach described by Hollands, 2011 [5], we analysed the horizontal and vertical component of the error independently. We employed a Kruskal-Wallis test [6] to check if the errors in horizontal and vertical directions are statistically independent. In order to increase the robustness and reduce the computational efforts, the drift algorithm we apply is based on a resolution pyramid, which first calculates the ice displacement from a coarse-resolution version of the image before this information is used to initialise the search for corresponding patterns at a higher resolution level. In this way, the displacement is refined at every level of the resolution pyramid until the original resolution of the input image is reached. The algorithm itself forms a cascade of multiple runs though the resolution pyramid. In the cascade, the displacement field is calculated repeatedly. With each cascade step, the number of pixels to be matched for a single displacement vector is reduced, leading to an increased spatial density of the displacement field. To compensate for the reduced robustness of the match due to the reduced number of pixels in the search window (also called "template"), the algorithm uses the coarser displacement field from the previous run as initial displacement information and refines it locally during each pass of the resolution pyramid. The similarity measure of the employed algorithm is a normalised cross correlation (NCC) with a prependedphase correlation for candidate selection [4], [7]. The phase correlation is more robust towards non-linear motion and computationally more efficient, while the NCC is more robust against noise [8], [9]. Manduchi and Mian, 1993 [10], who analysed the performance of phase correlation and NCC in the presence of noise, found that both methods are relatively sensitive to high frequency noise and that the phase correlation is generally more sensitive to noise than the cross correlation. For this reason, both techniques are combined in this approach following [7].

Errors in the displacement estimate based on this algorithm are related to the properties of the image data:

- Insufficient backscatter patterns in the radar images: It is not possible to find corresponding regions in two successive images (e.g. in the case of new ice areas that do not show any distinct structures such as ice floe margins, rafting zones or ridges) which means that pattern matching fails. Periodic patterns can lead to false matches (e.g. boundaries between belts of ice that develop in polynias)
- Strong changes in ice structures between the acquisitions of the two images: Reasons may be advancing deformation, rotation of ice floes, ice melt or other processes which influence the appearance of the ice in the image.
- Loss of corresponding patterns at the image borders: The width of the zone where patterns are lost depends on the drift velocity.
- Noise: The matching of pure noise leads to spurious displacement vectors.

Another class of errors is based on insufficiencies of the algorithm itself. As indicated above, the algorithm employs a multi-scale approach which calculates displacements at different image resolutions and uses the results from previous stages of the algorithm to start calculations at the following stage. In general, this procedure generates robust estimates of the drift field but may fail in specific situations:

- If the directions of displacements vectors are very heterogeneous in a given region, the initial displacement may cause the algorithm to search in the wrong direction.
- The initial windows for searching matching patterns are very large. Since the overlapping area of the satellite images often is not rectangular, matches may be affected by the edges of the image overlap.

We aim to identify the potential for a successful pattern matching by a combination of different textural measures for the search templates. Then, we generate a set of weights to evaluate the quality of the resulting sea ice displacements. To this end we calculate the sum of six different measures over each run through the image pyramid and over each cascade step. We call the resulting value "confidence factor", or CFA. A map can then be generated in which high values of the CFA show regions for which the retrieved displacements are less reliable than in regions of low values.

A. Texture Measures

In the following section we focus on the textural parameters that are applied on single images to characterize the radar backscatter pattern (i. e. image brightness or grey-tone variations). The approaches to describe the composition of the backscatter pattern can be subdivided into three classes: statistical, structural, and spectral approaches [11].

- The statistical approaches we selected are based on the evaluation of the image brightness histogram (e.g. variance, standard deviation and related measures).
- Structural approaches (often referred to as second order statistics): deal with the question how grey-tone (brightness) values are related to their surrounding area. This information can be collected, for example, in a grey level co-occurrence matrix.
- By using spectral approaches, image properties are analysed in the Fourier domain

For sea ice motion tracking with SAR images, Kwok et al., 1990 [12] employed a texture parameter described by Ulaby et al., 1986 [13] to assess whether the variance of the image brightness (radar intensity) in a given window is larger than the value expected due to speckle. Speckle is a granular multiplicative noise that degrades the quality of SAR images. It results from the interference of signals from several

randomly distributed scatteres in one radar resolution cell. The variance-to-mean ratio (VMR) is calculated using the standard deviation s and the mean value μ of the intensity (pixel) values within the given window. Combined with the the number of looks (ENL) one obtains the texture variance:

$$s^2_{\text{texture}} = \frac{\frac{s^2}{\mu^2} - \frac{1}{\text{ENL}}}{1 + \frac{1}{\text{ENL}}} \quad (1)$$

The equivalent number of looks is a measure of the speckle contribution to the intensity variations. If no textural component is present in an image intensity pattern (i. e. : $s^2_{\text{texture}} = 0$), it is equal to the inverse of the VMR. After applying a multi-looking f lter and subsequently an advanced Lee f lter to our SAR images, we estimated the ENL on the ice shelf where intensity patterns did not reval indications of textural components. We obtained an ENL of 50. The texture variance was calculated individually for every window in the resolution pyramids of each cascade step. When the texture variance is greater than 0,this may indicate the existence of a sea ice structure suitable for pattern-matching. We increment the CFA if the texture variance is lower than 0.45. The selection of the threshold is explained below.

The second parameter we take into account is the Mean Intensity Gradient (MIG) [14] obtained in a given window. For the calculation of the mean intensity gradient we use the Sobel f lter. If there are strong brightness differences, the mean intensity gradient is large, while it is close to zero for homogeneous regions. We increment the CFA if the MIG is lower than 1.5. The third parameter is the mean gradient slope (MGS). It is the second derivative of the intensity image, and hence, the slope of the gradient. The MGS has been adapted from Pearlstine, 2005 [15]. It is calculated by employing the Sobel f lter on the intensity gradient map. The gradient slope shows spatial changes of the gradient which can be an additional hint for structures. In contrary to the MIG which shows also high values in the case of a steep intensity value ramp inside a given window, the MSG takes into account the changes of the gradient, which is more closely related to higher-frequency intensity variation in the image. These may be caused by sea ice structures. We increment the CFA if the MGS is lower than 7.

B. Cross-Correlation

Even if one single image contains a suff cient number of structural elements, it has to be taken into account that the characteristics of corresponding intensity patterns can vary between two consecutive images, which reduces the chance of successful pattern-matching. This is ref ected in the magnitude of the correlation coeff cient which we therefore keep as a reliability measure but here in combination with other measures contributing to the CFA. Additionally, we take into account a conf dence interval for the correlation coeff cient dependent on the window size. For a small number of samples N in the window, the correlation coeff cient r becomes unreliable. We assume a standardised normal distribution $f(z)$ for the error of the correlation coeff cient and estimate the conf dence interval Δr at a signif cance level of $\alpha = 99\%$:

$$\Delta r = \frac{z(\alpha) \cdot (1 - r^2)}{\sqrt{N - 1}} \quad (2)$$

If Δr is larger than 0.1 (10% of the range of values for r), we regard r unreliable and increment the CFA. The need of this parameter for a realistic assessment of the correlation value in the case of sea ice motion tracking was already discussed by Fily, 1987 [16]. In the calculation of the cross-correlation coeff cient, high values have a stronger inf uence than low values. A single high intensity peak as it might be caused by a mirror ref ection of the radar signal from the ice surface may dominate the resulting cross-correlation. Mirror (also called specular) ref ections occur, e. g., if broken pieces of ice are oriented such that one side faces the radar. Hence, the occurrence of specular ref ections is very sensitive to the imaging geometry, i. e. incidence and look angle of the radar, and orientation and shape of the ref ecting ice structure. Even slight differences of the imaging geometry change the locations of mirror ref ections from the ice. As a consequence the correlation might link two randomly occurring specular events instead of estimating the correct underlying displacement which is obtained from the undisturbed sea ice backscatter pattern. Similar points have been previously addressed in the context of Particle Image Velocimetry (PIV) [14] and stereo matching [17], [18]. Although the effect of peaks in radar intensity is reduced using the phase correlation for pre-selection of possible candidates for the pattern matching, they can still have a signif cant effect. Therefore we implemented a f xed threshold of -3dB which adds a score to the CFA in case the maximum value within the template exceeds this threshold.

C. Combination of different reliability measures

By combining the different criteria into one value, we take into account the three different factors that lead to a pattern mismatch.

1) The combination of three different texture criteria, one from the f eld of SAR analysis and two others from pattern tracking are used to detect the presence of distinguishable patterns in the individual images. While the texture variability only suggests whether there are any signal variations that cannot be explained by speckle, the other two measures focus mainly on the characteristics of the variations and evaluate whether the pattern is potentially unique and therefore suitable for matching.
2) The calculations of "fake" displacements between mirror ref ections positioned randomly from image to image are reduced by excluding outliers of the radar intensity.
3) The success of pattern matching is assessed by the cross-correlation coeff cient and its uncertainty which depends on the number of pixels in the search window.

The single contributions to the CFA are summarized in Table I. First experiments with different texture parameters aimed to exclude individual displacement vectors based on thresholds during algorithm runtime in order to increase the accuracy of the result. This approach failed because it destabilizes the algorithm if too many vectors (5-10% of the total number) are

TABLE I
OVERVIEW OF THE PARAMETERS CONTRIBUTING TO THE CFA

Parameter	Threshold
Texture variance	> 0.45
Mean intensity gradient	< 1.5
Mean gradient slope	< 7
Intensity threshold	$>$ -3dB
Correlation coefficient r	< 0.2
Confidence interval for r	< 0.1

excluded. To avoid this effect, we analysed the distribution of values for each individual parameter at all steps of the algorithm. Then, we empirically determined the individual thresholds for the assessment of reliability. Displacement vectors appearing unreliable in a single step of the algorithm are not removed. Consequently, the reliability of a displacement vector in the final result is influenced by the reliability of all previous estimates. For this reason we accumulate the CFA over all steps of the algorithm.

D. Back-matching

The concept of back-matching originates from the field of photogrammetry and is e.g. described by Schreer, 2005 [19]. It is a simple consistency check. For the back-matching, we calculate the respective field of displacements twice, the first one by matching image 1 with image 2 and the second one by reversing the image order. For the comparison, the result obtained from image pair 2-1 needs to be inverted and resampled to the grid used to calculate the displacement vectors for image pair 1-2. We emphasize the fact that the problems of pattern matching discussed above apply in the same way for image pairs 1-2 and 2-1. In the ideal case, the resulting displacements have identical magnitude and direction and the Euclidean distance between both fields (referred to as back-matching distance) is zero. Under realistic conditions, this distance is larger than zero. It assumes low values for regions where the matching works and larger values for regions where it fails. In contrary to the CFA, this procedure assesses the overall consistency of the algorithm result independent of the texture characteristics of the images. For an easier evaluation of the result, we calculated a normalised back matching difference which takes into account the estimated velocities. The normalised back matching difference is calculated from the velocity components u_f, v_f of the forward calculation and u_b, v_b of the backward run:

$$\|\vec{v}\| = \frac{(u_b - u_f)^2 + (v_b - v_f)^2}{\sqrt{u_b^2 + v_b^2} \cdot \sqrt{u_f^2 + v_f^2}} \quad (3)$$

By this means the influence of the velocity on the back-matching difference is removed.

III. RESULTS

In the following section, results are presented in terms of ice drift, i. e. the displacement vectors obtained from the application of the tracking algorithm were divided by the time difference between the acquisitions of the two respective SAR images. We compare the estimated drift with manually measured drift vectors to assess the performance of our drift algorithm. We found systematic errors between -100 and 240 m/d, and standard deviation between 13 and 430 m/d. Given the fact that we measured displacements of 9-30 km per day, these findings correspond to a relative error of up to 11% for the systematic deviations and up to 21% for the standard deviation. These are maximum values for the image pair 18.02-19.02.2008. For all other cases, the systematic error is below 2% and the random error below 8% (Table II). If we take into account that the spatial resolution of the images is 150×150 m, the systematic errors correspond to displacements smaller than 2 pixels. For the random components, we found corresponding displacements of $\pm$ 0-3 pixels. However, we have to take the uncertainty in the manual determination of the reference displacement field into consideration. We estimate that the random error of the manually derived drift field is on the order of $\pm$ 1-2 pixels ($\pm$ 150-300 m/d), depending on how well structures in the images can be recognized. This means that the presented statistics only takes into account regions where we were able to find traceable patterns and omits areas which were problematic for manual measurements.

TABLE II
DRIFT FIELD STATISTICS FOR DIFFERENT SATELLITE IMAGE PAIRS FROM COMPARISON OF AUTOMATICALLY RETRIEVED AND REFERENCE DATA. ALL UNITS ARE (M/D).

Date	18./19.02. 2008	19./20.02. 2008	22./23.02. 2008	30./31.05. 2008	31.05./ 01.06. 2008
Horizontal mean error	-102	-93	-28	-62	30
Horizontal standard deviation	256	206	121	127	13
Horizontal mean velocity	8925	6225	1575	6750	-7800
Vertical mean error	236	218	21	7	-98
Vertical standard deviation	430	305	105	114	227
Vertical mean velocity	-2025	23494	24675	28875	12750

An error including the regions of the entire image can be assessed by back-matching. We found that the errors for all images are significantly larger, due to the inclusion of regions that are less suited for pattern matching. The CFA which accumulates scores for the presented texture measures and the correlation coefficient over the entire cascade provides a realistic indication for the reliability of the drift field. Depicted in Figure 3 is a SAR image for visual reference. Figure 4 shows the CFA, which highlights the ice shelf and the margins of the image. In both regions, the performance of the algorithm is less reliable. Figure 5 shows an example of the relative back-matching difference. One can clearly identify stable regions in the drift field where results from image pairs 1-2 and 2-1 compare well, and regions where the search

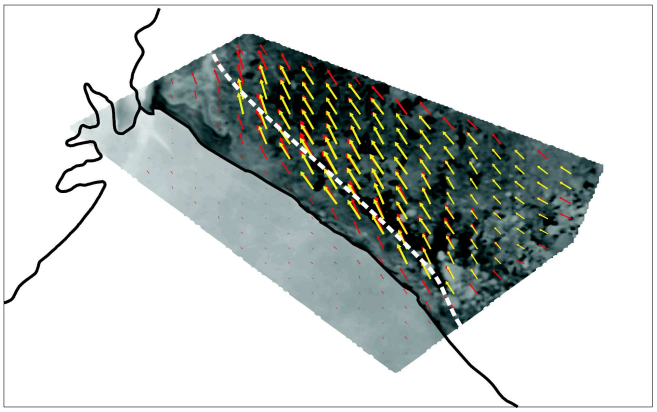

Fig. 3. Envisat WS SAR image taken on the 18.02.2008. The dashed line indicates the approximate position of the polynia. The red arrows show the output of the sea ice drift algorithm, the yellow arrows are reference drift vectors resampled to the position of the algorithm output

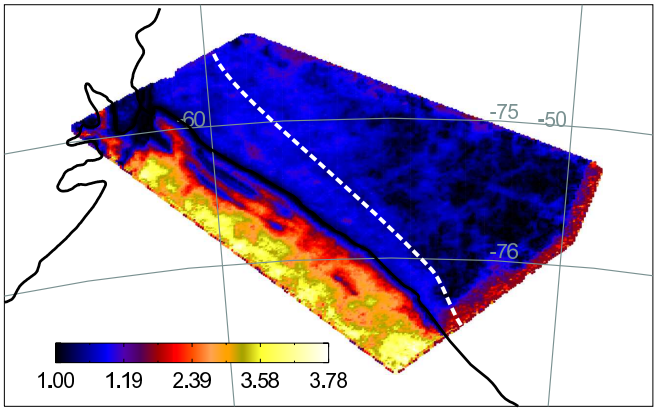

Fig. 4. CFA. The dashed line shows the approximate position of the polynia

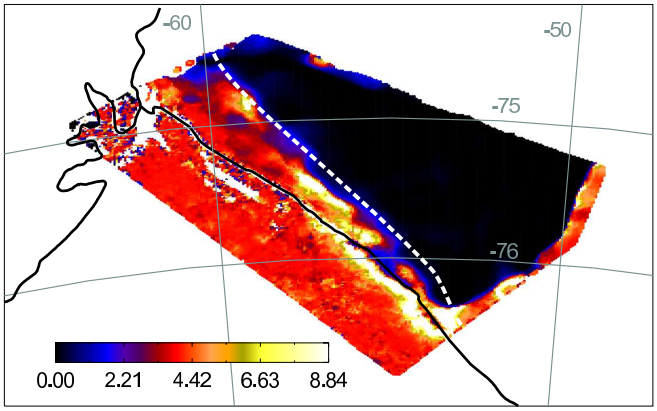

Fig. 5. Relative back matching difference. The dashed line shows the approximate position of the polynia

in pair 2-1 provided completely different results. We find a strong consistency between Figure 4 and Figure 5 except for the area of the polynia. The differences can be explained by the fact that the CFA only takes into account errors caused by insufficient texture or low and unreliable correlation coefficients, while the back-matching evaluates directly the consistency of the displacement field.

To identify the reasons for drift mismatches, we plotted the

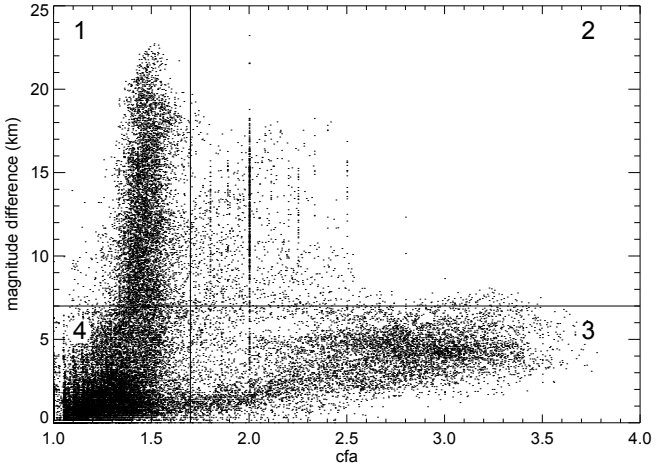

Fig. 6. Scatterplot of absolute differences over CFA for the image pair 18./19.02.2008

relation between CFA and back-matching difference in Figure 6. Since we can discern several distinctive clusters, we chose a simple cluster based classification approach to guide the interpretation of our data.

We identified four spatially separated classes in the scatterplot in Figure 6:

1) a low CFA score of < 1.7 but a large back-matching differences between 7-20 km, This class is linked with areas which have a sufficient texture for correlation but where the algorithm fails because of pattern instability or pattern loss at image borders. This class corresponds to the polynia with its fast-changing structures due to newly forming ice.
2) higher CFA values (> 1.7) and large back-matching differences. Here, insufficient texture is combined with a relatively high back-matching difference. This class is mainly found at the edges where the ice drifts into or out of the image.
3) a highly variable CFA, which is larger than 1.7 but has low back-matching differences below 7 km. This class can be found mainly on the shelf, where there is very little discernible texture but also no motion in the time frame we consider here.
4) good CFA values (lower than 1.7) and small back-matching differences (below 7 km). This is the region where sufficient texture is available for reliable pattern matching. Those regions are in the pack ice which exhibits several structural patterns, but also on land, the shelf ice edge and in the vicinity of visible cracks in the shelf which provide clear structures.

The classification result is visualised in Figure 7.

IV. Discussion

In our approach we choose to combine different parameters by which image characteristics (or in our case sea ice conditions) can be assessed with regard to their suitability for a successful retrieval of sea ice displacement. We can automatically separate the ice shelf or other nearly uniform regions, such as large icebergs, from sea ice. We found that

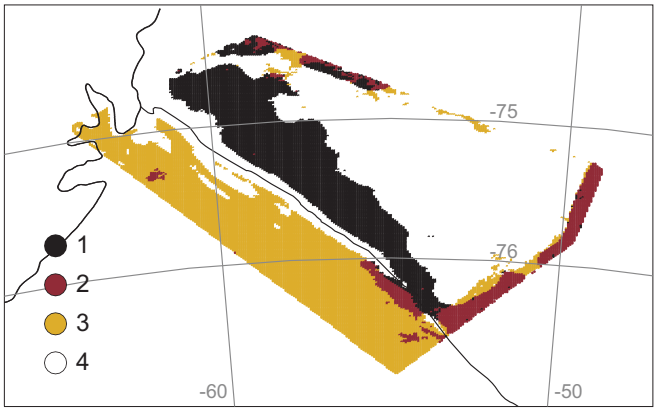

Fig. 7. Classif cation result for the image pair 18./19.02.2008

using single quality measures is not suff cient to assess the reliability of the pattern-matching. It has to be considered that the design of the employed drift algorithm reveals already a relatively high level of robustness. As long as enough reliable displacements ”survive” single levels in the resolution pyramid in each step of the cascade (due to high correlation values), more unreliable candidates can be successfully replaced by interpolation. The algorithm works on different resolution levels with different template sizes, calculating the displacement vector f eld at one resolution level and smoothing it as an initial guess for the displacement vector f eld on the following resolution level. The smoothing procedure suppresses single wrong matches. Additionally, the amount of details in image patterns and hence their potential for correlation might vary on the different resolution levels and for the different template sizes. This means that even for areas with poor texture at the highest resolution, the found displacements may be correct due to reliable correspondences on previous resolution levels.

Calculated drift velocities in homogeneous regions, such as ice shelves, are close to zero. As a consequence, the resulting back-matching differences are also low. Although this result is formally correct, it is desirable to automatically exclude such areas. Since the CFA score is high when there is insuff cient texure, it is possible to identify homogeneous regions based on the CFA only (see also Figure 4 and Figure 7, class 3). For this reason we consider a combination of the CFA and the back-matching difference necessary for a robust estimate of the quality of our drift f eld calculation. The CFA suggested in this work may be extended by introducing additional parameters. Karvonen, 2012 [2], for example suggested different measures to characterize the properties of the phase correlation function.

V. Conclusion

We have shown that the correlation coeff cient alone does not provide a suff ciently reliable measure for the quality of a sea ice drift f eld retrieved from a SAR image pair. Therefore, we introduced a combination of different parameters characterizing the potential of texture for a reliable correlation together with the correlation coeff cient and its conf dence interval. The different values were combined by a score called conf dence factor (CFA) which provides a quantitative number for an assessment of the expected accuracy of the derived drift f eld. The higher the CFA score is, the less reliable are the resulting drift vectors based on the available texture information and the cross-correlations in each step of the algorithm.

The reliability of calculated drift vectors does not only depend on the texture and the correlation but also on other effects like pattern stability. In order to account for these effects, a back-matching technique was employed. This technique is based on a double calculation of the drift vector f eld, f rst taking patterns from the f rst image in order to identify corresponding patterns in the second image and then changing the order of the images. If the results are consistent, the drift f eld is reliable. Unreliable regions are indicated by higher differences between forward and backward matching directions.

The use of the suggested measures is intended for providing information on the reliability of retrieved drift f elds in the absence of in-situ data from buoys or drift stations. This is essential not only for the comparison with model simulations but also for operational sea ice mapping and the potential assimilation of the data into sea ice models. The introduced reliability measures may be supplemented by additional criteria, in order to increase their robustness.

Acknowledgment

The work of the f rst author is funded by the Alfred Wegener Institute in the framework of the German Earth Observing Network (Network EOS). S. Linow’s and W. Dierking’s contribution to this study are part of the EU 7th Framework project SIDARUS (grant agreement no. 262922). The SAR images were provided by ESA for the Cat-1 project C1P.5024.

References

[1] D. Vernon, *Fourier Vision: Segmentation and Velocity Measurement Using the Fourier Transform*. Norwell, MA, USA: Kluwer Academic, 2001.

[2] J. Karvonen, “Operational sar-based sea ice drift monitoring over the baltic sea,” *Ocean Science*, vol. 8, no. 4, pp. 473–483, 2012.

[3] T. Hollands, V. Haid, W. Dierking, R. Timmermann, and L. Ebener, “Sea ice motion at the ronne polynia, antarctica: Sar observations vs. model results,” *Journal of Geophysical Research*, 2012, [submitted for publication].

[4] M. V. Thomas, “Analysis of large magnitude discontinuous non-rigid motion,” dissertation, University of Delaware, Delaware, USA, 2008. [Online]. Available: http://proquest.umi.com/pqdweb?did=1654490401&sid=5&Fmt=2&clientId=8331&RQT=309&VName=PQD

[5] T. Hollands and W. Dierking, “Performance of a multiscale correlation algorithm for the estimation of sea ice drift from sar images: initial results,” *Annals of Glaciology*, vol. 52, no. 57, pp. 311–317, 5 2011. [Online]. Available: http://www.igsoc.org/annals/v52/57/x57A037.pdf

[6] W. H. Kruskal and W. A. Wallis, “Use of ranks in one-criterion variance analysis,” *Journal of the American Statistical Association*, vol. 47, no. 260, pp. 583–621, 12 1952. [Online]. Available: http://links.jstor.org/sici?sici=0162-1459%28195212%2947%3A260%3C583%3AUORIOV%3E2.0.CO%3B2-A

[7] M. Thomas, C. Kambhamettu, and C. A. Geiger, “Motion tracking of discontinuous sea ice,” *IEEE Transactions on Geoscience and Remote Sensing*, vol. 49, pp. 5064–5079, 12 2011.

[8] J. P. Lewis, “Fast normalized cross-correlation,” in *Proceedings of Vision Interface 95*, Quebec City, Canada, 5 1995, pp. 120–123.

[9] A. Eckstein and P. P. Vlachos, “Digital particle image velocimetry (dpiv) robust phase correlation,” *Measurement Science and Technology*, vol. 20, no. 5, p. 14, 4 2009.

[10] R. Manduchi and G. A. Mian, “Accuracy analysis for correlation-based image registration algorithms,” in *IEEE International Symposium on Circuits and Systems (ISCAS)*. IEEE, 5 1993, pp. 834–837.

[11] R. C. Gonzalez and R. E. Woods, *Digital Image Processing*, 3rd ed., M. J. Horton, Ed. Upper Saddle River, New Jersey: Pearson Education, Inc., 2008.
[12] R. Kwok, J. C. Curlander, R. McConnell, and S. S. Pang, "An ice-motion tracking system at the alaska sar facility," *IEEE Journal of Oceanic Engineering*, vol. 15, no. 1, pp. 44–54, 1 1990.
[13] F. T. Ulaby, F. Kouyate, B. Brisco, and T. H. L. Williams, "Textural infornation in sar images," *IEEE Transactions on Geoscience and Remote Sensing*, vol. GE-24, no. 2, pp. 235 – –245, 3 1986.
[14] B. Pan, Z. Lu, and H. Xie, "Mean intensity gradient: An effective global parameter for quality assessment of the speckle patterns used in digital image correlation," *Optics and Lasers in Engineering*, vol. 48, no. 4, pp. 469–477, 4 2010.
[15] L. Pearlstine, K. M. Portier, and S. E. Smith, "Textural discrimination of an invasive plant, schinus terebinthifolius, from low altitude aerial digital imagery," *Photogrammetric Engineering & Remote Sensing*, vol. 71, no. 3, pp. 289–298, 3 2005.
[16] M. Fily and D. A. Rothrock, "Sea ice tracking by nested correlations," *IEEE Transactions on Geoscience and Remote Sensing*, vol. GE-25, no. 5, pp. 570–580, 9 1987.
[17] M. R. Jenkin, A. D. Jepson, and J. K. Tsotsos, "Techniques for disparity measurement," *CVGIP: Image Understanding*, vol. 53, no. 1, pp. 14–30, 1 1991.
[18] B. K. P. Horn, "Non-correlation methods for stereo matching," *Photogrammetric Engineering & Remote Sensing*, vol. 49, no. 4, pp. 535–536, 4 1983.
[19] O. Schreer, *Stereoanalyse und Bildsynthese*. Springer, 2005.

B PUBLICATION LIST

B.1 UNIVERSITY STUDIES

06/2006 [Talk] Hollands, T., Boström, G., Goncalves, J.G.M., Gutjahr, K., Niemeyer, I. & Sequeira, V. (2006): *3D Change Detection based on DSM extraction from satellite images*; 57. Berg- und Hüttenmännischen Tags an der TU Bergakademie Freiberg, 2006.

06/2007 [Poster] Boström, G., Goncalves, J.G.M., Gutjahr, K., Hollands, T., Niemeyer, I. & Sequeira, V. (2007): *3D Change Detection from Satellite Imagery*; 29. Symposium on Safeguards and Nuclear Material Management, Aix-en-Provence, France, 22.-24. May 2007.

06/2007 [Paper] Hollands, T., Boström, G., Goncalves, J.G.M., Gutjahr, K., Niemeyer, I. & Sequeira, V. (2007): *3D Change Detection from Satellite Imagery*; In: Proc. 29. Symposium on Safeguards and Nuclear Material Management, Aix-en-Provence, France, 22.-24. May 2007.

06/2010 [Paper] Eckert, S., Hollands, T. (2010): *Comparison of Automatic DSM Generation Modules by Processing IKONOS Stereo Data of an Urban Area*; IEEE Journal of Selected Topics in Applied Earth Observations and Remote Sensing, 3(2), 162 - 167, 2010.

B.2 DOCTORAL RESEARCH

06/2009 [Poster] Hollands, T. (2009): *Algorithms for the automatic tracking of sea ice*; AWI PhD days 2009, List(Sylt), June 2009.

10/2009 [Talk] Hollands, T. (2009): *Monitoring drift and deformation of sea ice based on SAR satellite data*; EOS fall school 2009, Herrsching am Ammersee, 26.-29. October 2009.

05/2010 [Poster] Hollands, T., Dierking, W. (2010): *High resolution monitoring of sea ice drift with SAR satellite data*; International Symposium on Sea Ice in the Physical and Biogeochemical System, International Glaciological Society, Tromsø, Norwegen, 31 May - 4 June 2010.

06/2010 [Poster] Hollands, T., Dierking, W. (2010): *Monitoring of sea ice drift and deformation with SAR satellite data of different resolution*; ESA Living Planet Symposium, 28 June - 2 July 2010, Bergen, Norwegen.

06/2010 [Paper] Hollands, T., Dierking, W. (2010):*Monitoring of sea ice drift and deformation with SAR satellite data*; Proceedings of ESA Living Planet Symposium, 28 June - 2 July 2010, Bergen, Norway / European Space Agency, H. Lacoste-Francis, (ed.), 1 CD-ROM. Noordwijk: ESA Communication Production Office (SP / European Space Agency; 686).

11/2010 [Talk] Hollands, T. (2010): *Sea ice motion tracking from SAR satellite imagery – Validation of an algorithm and comparison of different resolutions*; EOS fall school 2010, Lauenburg an der Elbe, 16.-19. November 2010.

05/2011 [Paper] Hollands, T., Dierking, W. (2011): *Performance of a multiscale correlation algorithm for the estimation of sea ice drift from SAR images: initial results*; Annals of Glaciology, 52 (57), 311-317, 2011.

05/2011 [Talk] Hollands, T., Dierking, W. (2011): *Sea ice in motion: New techniques for the observation of sea ice drift and deformation employing satellite radar images*; AWI PhD days 2011, Helgoland, Mai 2011.

09/2011 [Talk] Hollands, T., Haid, V., Dierking, W. (2011): *Sea ice kinematics around the Ronne Polynia derived from space*; YOUMARES 2.0, Bremerhaven, 7.-9. September 2011.

10/2011 [Talk] Hollands, T., Haid, V., Dierking, W. (2011): *Sea ice kinematics around the Ronne Polynia derived from satellite images and model simulations - first results of a comparison*; 12. Meeting of the "International Ice Charting Working Group", Cambridge, U.K., 17.-21. Oktober 2011.

07/2012 [Paper] Hollands, T., Haid, V., Dierking, W., Timmermann, R., Ebner, L (2012): *Sea ice motion at the Ronne Polynia, Antarctica: SAR observations vs. model results*; Submitted for publication in Journal of Geophysical Research – Oceans.

09/2012 [Paper] Hollands, T., Linow, S., Dierking, W. (2012): *Reliability measures for sea ice motion retrieval from synthetic aperture radar images*; Manuscript prepared for submission to Journal of Selected Topics in Applied Earth Observations and Remote Sensing.